



universität  
wien

# DISSERTATION

Titel der Dissertation

„Structural and functional studies for the disassembly of  
hemidesmosomes regulated by calcium-calmodulin“

Verfasser

Jaegeun Song

angestrebter akademischer Grad

Doctor of Philosophy (PhD)

Wien, 2014

Studienkennzahl lt. Studienblatt:

A 094 490

Dissertationsgebiet lt. Studienblatt:

Molekulare Biologie

Betreut von:

Univ.-Prof. Dipl.-Ing. Dr. Kristina Djinovic-Carugo



## Table of Contents

ACKNOWLEDGEMENTS .....	5
ABSTRACT .....	6
LIST OF ABBREVIATIONS .....	7
1. INTRODUCTION.....	8
1.1. Hemidesmosomes.....	8
1.2. Hemidesmosome assembly .....	9
1.2.1 Plectin .....	11
1.2.1.1. Domain structure of plectin and its molecular interactions .....	12
1.2.1.2. Isoform diversity of plectin .....	14
1.2.1.3. Human diseases related to plectin .....	15
1.2.1.4. Structure and function of the actin-binding domain .....	16
1.2.2 Integrin $\alpha 6\beta 4$ .....	18
1.2.2.1. Integrins .....	18
1.2.2.2. Integrin domain structures and the interactions.....	21
1.2.2.3. Integrin $\alpha 6\beta 4$ .....	23
1.2.2.4. Structure of the fibronectin type III domain.....	23
1.3. The plectin/integrin $\beta 4$ complex in hemidesmosomes and its regulation by phosphorylation .....	25
1.4. Calmodulin regulation of the plectin/integrin $\beta 4$ complex .....	27
1.4.1. Calmodulin.....	27
1.4.2. Various conformations of calmodulin .....	28
1.4.3. Target recognition of calmodulin .....	30

1.4.4. Calmodulin complexes .....	30
2. THE AIM OF THE STUDY .....	34
3. RESULTS.....	35
3.1. Structural studies on plectin 1a actin-binding domain .....	35
3.1.1. Construct design.....	35
3.1.2. Purification of plectin 1aABD constructs .....	35
3.1.3. Prediction of the disordered region of the N-terminal tail .....	36
3.1.4. Mapping of calmodulin interaction site on plectin 1a.....	37
3.1.5. Crystallization and structure determination of P1aABD $_{\Delta 22}$ .....	38
3.1.6. The crystal structure of P1aABD $_{\Delta 22}$ .....	39
3.1.7. The solution structure of P1aABD.....	41
3.2. Studies on the plectin 1a actin-binding domain/calmodulin complex.....	44
3.2.1. Construct design.....	44
3.2.2. Purification of calmodulin constructs.....	44
3.2.3. Thermal shift assay (Thermofluor) .....	46
3.2.4. Cross-linking and Mass Spectrometry analyses .....	46
3.2.5. N-lobe of CaM preferably binds to P1aABD.....	50
3.2.6. Crystallization and structure determination of the P1aABD $_{\Delta 22}$ /CaM $_{NL}$ complex .....	50
3.2.7. Crystal structure of the P1aABD $_{\Delta 22}$ /CaM $_{NL}$ complex.....	53
3.2.8. Molecular determinants for the preferable binding of CaM $_{NL}$ .....	58
3.2.9. SAXS structure of the P1aABD/CaM complex.....	61
3.2.9.1. <i>Ab initio</i> modeling.....	61

3.2.7.2. An extended conformation of CaM in complex with P1aABD .....	63
3.3. Studies on the plectin 1a actin-binding domain/integrin $\beta$ 4 complex .....	65
3.3.1. Construct design .....	65
3.3.2. Purification of $\beta$ 4Fn12 .....	65
3.3.3. Crystallization and structure determination of the P1aABD $_{\Delta 22}$ / $\beta$ 4Fn12 complex .....	66
3.3.4. Crystal structure of the P1aABD $_{\Delta 22}$ / $\beta$ 4Fn12 complex .....	67
3.2.5. SAXS structure of the P1aABD/ $\beta$ 4Fn12 complex .....	70
3.4. Disassembly of the P1aABD/ $\beta$ 4Fn12 complex by CaM binding .....	73
3.4.1. <i>In silico</i> analysis of the dissociation mechanism .....	73
3.4.2. Competitive binding assay by displacement ITC .....	74
4. DISCUSSION .....	77
4.1. The role of the isoform specific sequence of plectin 1a .....	77
4.2. The non-canonical binding of calmodulin in an extended conformation .....	78
4.3. Calmodulin is the first reported binding partner of isoform specific sequences of plectin .....	80
4.4. The role of calmodulin binding to plectin in the interaction with F-actin .....	81
4.5. Summary .....	82
5. MATERIALS AND METHODS .....	85
5.1. Molecular cloning .....	85
5.1.1. Plectin 1aABD .....	86
5.1.2. Calmodulin .....	86
5.1.3. Integrin $\beta$ 4 .....	86
5.1.4. Site-directed mutagenesis of plectin 1aABD .....	87
5.2. Protein expression and purification .....	87

5.3. Thermal shift assay (thermofluor).....	88
5.4. Determination of protein concentration.....	89
5.5. Protein crystallization .....	90
5.5.1. Crystallization and Structure Determination of the P1aABD <sub>Δ22</sub> .....	90
5.5.2. Crystallization and structure determination of the P1aABD <sub>Δ22</sub> /CaM <sub>NL</sub> complex .....	90
5.5.3. Crystallization and structure determination of the P1aABD <sub>Δ22</sub> /β4Fn12 complex .....	91
5.5.4. Crystal dehydration.....	91
5.6. Isothermal Titration Calorimetry (ITC) .....	93
5.7. Small angle X-ray scattering (SAXS).....	93
5.7.1. SAXS analysis of P1aABD.....	93
5.7.2. SAXS analysis of the P1aABD/CaM complex.....	94
5.7.3. SAXS analysis of the P1aABD/ β4Fn12 complex .....	95
5.8. Pull-down assay .....	95
5.9. Cross-linking and mass spectrometry analyses .....	96
6. REFERENCES.....	99
7. CURRICULUM VITAE.....	112

## ACKNOWLEDGEMENTS

I started my PhD study since I was selected for the DK program 'Structure and Interaction of Biological Macromolecules' in 2009. First of all, I am grateful to all DK faculty members for giving me an opportunity to study in Vienna, especially to those who organized and coordinated the PhD program, Prof. Tim Skern, Prof. Kristina Djinovic-Carugo, Ulrike Seifert, and Franziska Werba.

I would like to thank to my PhD committee member, Prof. Gerhard Wiche, Dr. Bojan Zagrovic, and Dr. Gang Dong. They provided me critical suggestions and advices, guiding me to work in a scientific way.

I would like to thank to my collaborators. For cross-linking and mass spectrometry analyses, Dr. Friedel Drepper and Prof. Bettina Warsheid in University of Freiburg help me a lot to carry out proper cross-linking experiments and to analyze data obtained. For SAXS studies, Dr. Petr Konarev and Dr. Dmitri I. Svergun in EMBL Hamburg gave me critical suggestions and advices to analyze SAXS data.

I would like to thank to my thesis reviewers, Prof. Friedrich Propst, Prof. Hans Brandstetter, and Prof. Klaus Scheffzek. I am really grateful for assigning your precious time to evaluate my thesis.

I would like to thank to my colleagues, especially to Julius Kostan, Dr. Irina Grishkovskaya, Dr. Euripedes Ribeiro, and Dr. Nikos Pinotsis. They guided most kinds of experiments to me, which I performed during my study.

Many thanks to my supervisor, Prof. Kristina Djinovic-Carugo. I have learned many things from you during my PhD. It would be a great asset for my scientific life in future.

Finally, thanks to my parents, my wife, Hyewon, and my daughter, Jina. All glories to Jesus, my Lord.

## ABSTRACT

The plectin-integrin  $\beta 4$  complex plays a pivotal role to maintain the mechanical stability of hemidesmosomes in keratinocytes. The binding of calcium-calmodulin (CaM) to plectin isoform 1a contributes to the disruption of the interaction between plectin and integrin  $\beta 4$  together with the phosphorylation on several sites of integrin  $\beta 4$ , which results in the disassembly of hemidesmosomes during keratinocyte differentiation and migration. During my PhD thesis, I characterized the interaction between CaM and the actin binding domain of plectin 1a (P1aABD) by ITC and cross-linking assays, and revealed the preferable binding of the N-lobe of CaM (CaM<sub>NL</sub>) to the N-terminal tail of plectin 1a. I determined the crystal structure of the P1aABD in complex with the N-lobe of CaM to 1.8Å resolution and the entire complex construction was completed by SAXS modeling. The structural analyses show that the disordered N-terminal tail of plectin 1a alters the conformation to  $\alpha$ -helix dependent upon the binding of CaM, which is varied into the hydrophobic cleft of (CaM<sub>NL</sub>).

To shed light on the detailed mechanism of the disassembly of the P1aABD/integrin  $\beta 4$  complex in hemidesmosomes modulated by the binding of calcium-calmodulin to plectin, I also solved the crystal structure of the P1aABD/integrin  $\beta 4$  complex. The dissociation mechanism of the P1aABD/integrin  $\beta 4$  driven by CaM was simulated by displacement ITC experiments and the superposition of two structures. The results suggest that CaM binding causes a steric clash against integrin  $\beta 4$  and promotes the disruption of the plectin-integrin  $\beta 4$  complex. My PhD studies provide the first structural insight into the hemidesmosome disassembly modulated by calcium-calmodulin.



## LIST OF ABBREVIATIONS

HD: hemidesmosome

BP180: bullous pemphigoid antigen 180

BP230: bullous pemphigoid antigen 230

CH: calponin homology

ABD: actin-binding domain

EBS-MD: Epidermolysis bullosa simplex with muscular dystrophy

CaM: calmodulin

CaM<sub>NL</sub>: N-terminal lobe of calmodulin

CaM<sub>CL</sub>: C-terminal lobe of calmodulin

FN-III: fibronectin type III domain

SAXS: small angle X-ray scattering

CD: circular dichroism spectroscopy

NMR: nuclear magnetic resonance

ITC: isothermal titration calorimetry

R<sub>g</sub>: radius of gyration

D<sub>max</sub>: maximum intramolecular distance

I(0): extrapolated scattering intensity at zero-angle

P1aABD: plectin 1a actin-binding domain

β4FN12: the first pair of fibronectin type III domains of integrin β4

CS: connecting segment of integrin β4

EDC: 1-ethyl-3-[3-dimethylaminopropyl]carbodiimide hydrochloride

sulfo-NHS: *N*-hydroxysulfosuccinimide

MS: mass spectrometry

K<sub>d</sub>: dissociation constant

RMSD: root-mean-square deviation

## 1. INTRODUCTION

### 1.1. Hemidesmosomes

Hemidesmosomes are the junctional complexes that connect epithelial cells (Farquhar & Palade, 1963). The name of hemidesmosome is originated from the structural similarity with desmosome: one half of a desmosome that mediates the lateral adhesion of epithelial cells (Jones et al, 1994). Electron microscope studies on the basal layer of human epithelial cells found that hemidesmosomes possess electron-dense plaques at one side of epithelial membranes, unlike desmosomes featuring electron-dense plaques at each side of membranes where intermediate filament networks are associated (**Figure 1.1A**) (Borradori & Sonnenberg, 1996; Green & Jones, 1996).

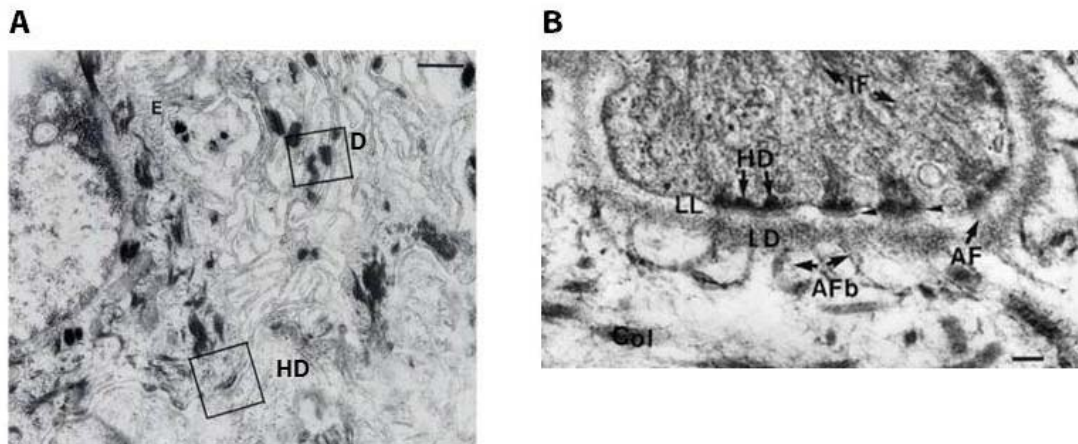


**Figure 1.1. (A)** Electron micrograph of the basal layer of human epidermis, showing the structural difference between desmosomes (D) and hemidesmosomes (HD), modified from the work of (Green & Jones, 1996). *Scale bar: 500 nm.* **(B)** Electron micrograph of the basal layer of a human keratinocyte. Abbreviations are the followings; IF: intermediate filaments, LL: lamina lucida, HD: hemidesmosome, LD: lamina densa, AF: anchoring filaments, AFb: anchoring fibrils, Col: collagen fibers. *Scale bar: 100 nm.* The figure was reproduced from (Borradori & Sonnenberg, 1999)

Hemidesmosomes play a role in establishing a firm attachment of epithelial cells to the underlying basement membrane by connecting extracellular matrix proteins to intermediate filaments in epithelial cells (Jones et al, 1994). Hemidesmosomes are closely located onto the sub-basal plate in the lamina lucida of the basement membrane, which is connected to the lamina densa via the anchoring filaments. Anchoring fibrils in the dermis are associated with lucida densa in the basement membrane (**Figure 1.1B**) (Borradori & Sonnenberg, 1999; Jones et al, 1998). Hemidesmosomes maintain the stable architecture for the integrity of epithelial cells; however, this function is dynamically regulated upon responding to the signals for cell differentiation, migration, or wound healing (Litjens et al, 2006).

## 1.2. Hemidesmosome assembly

Hemidesmosomes are the multi-protein complexes, which components are largely classified into three categories: the cytoplasmic proteins, the transmembrane proteins, and extracellular proteins (**Figure 1.2**) (Green & Jones, 1996). The cytoplasmic part of hemidesmosomes comprises BP230 and plectin, which connect the intermediate filament network to hemidesmosomes. BP230 (bullous pemphigoid antigen 230) was originally characterized as the 230 kDa antigen protein that is targeted by auto-antibodies in bullous pemphigoid (a skin blistering disease caused by an auto-immune disorder) (Stanley et al, 1988). BP230 is involved in the hemidesmosome architecture; the C-terminal domain interacts with keratin intermediate filaments and the N-terminal domain binds to the transmembrane components of hemidesmosomes (BP180 and integrin  $\alpha 6\beta 4$ ). Plectin is a cytoskeletal linker protein connecting different elements of cytoskeletons, expressed in a variety of mammalian cells.

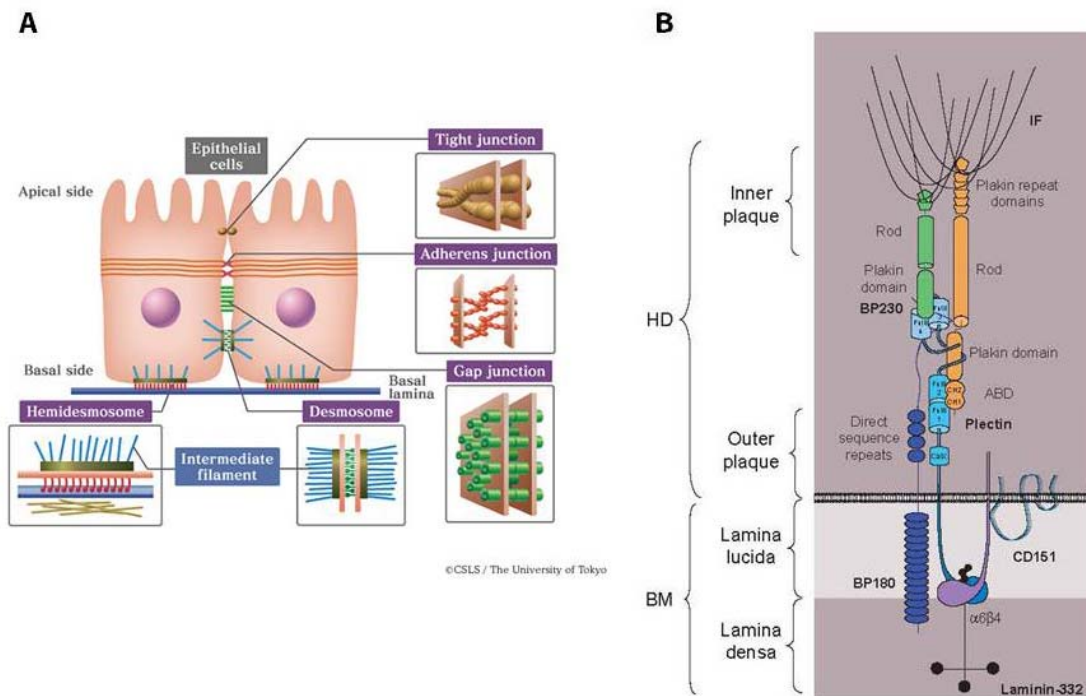


**Figure 1.2. (A)** Junctional complexes that connect epithelial cells. **(B)** Schematic illustration of the hemidesmosome, showing hemidesmosomal components in three categories: extracellular protein (laminin-322), transmembrane proteins (BP180 and integrin  $\alpha6\beta4$ ), and cytoplasmic proteins (plectin and BP230). The figure was modified from (Litjens et al, 2006).

The N-terminal globular part of plectin, including the actin binding domain and the plakin domain, interacts with the cytoplasmic domains of integrin  $\beta4$ , and the C-terminal part binds to intermediate filaments such as cytokeratins (Reznicek et al, 1998; Wiche et al, 1982). The transmembrane part of hemidesmosomes comprises BP180 and integrin  $\alpha6\beta4$ . BP180 is also identified as a target antigen of bullous pemphigoid, which has a large extracellular domain containing 15 collagenous subdomains (Giudice et al, 1992). The cytoplasmic part of BP180 is known to interact with integrin  $\alpha6\beta4$  (Borradori et al, 1997). The  $\alpha6\beta4$  integrin heterodimer is a principal constituent of the hemidesmosome assembly (Stepp et al, 1990). It serves as a transmembrane receptor for laminin-332, previously

termed laminin-5 consisted of three subunits ( $\alpha 3$ ,  $\beta 3$ , and  $\gamma 2$ ) (Aumailley et al, 2005), to mediate hemidesmosome formation and plays a role in the stable assembly of hemidesmosomes (Baudoin et al, 2005). The cytoplasmic part of  $\beta 4$  integrin associates with plectin and BP230. The extracellular proteins consist of laminin 322 and type IV collagen. Laminins are the heterotrimeric glycoproteins mainly found in basement membrane. Laminin-322 is a major ligand of the integrin  $\alpha 6\beta 4$  and the interaction is essential for the stable adhesion of hemidesmosomes. It also supports the keratinocyte motility. During the wound healing of the epidermis, the laminin-322 synthesis is up-regulated and the keratinocyte starts to migrate via the interaction with integrin  $\alpha 3\beta 1$  (Goldfinger et al, 1999).

#### 1.2.1. Plectin

Plectin is one of the cytoplasmic components of hemidesmosomes, interacting with integrin  $\beta 4$  to maintain the mechanical stability of hemidesmosomes. It was named according to preliminary studies on the cytoskeletal network formation, meaning a net or a mesh in Greek (Wiche & Baker, 1982). Plectin is a cytoskeletal linker protein that connects different cytoskeletal elements (actin filaments, intermediate filaments, and microtubules), and co-localized with cytoskeleton attachment sites including hemidesmosomes, desmosomes, Z-disks in sarcomere, and focal adhesions. Plectin has a large molecular weight that ranges from 499 kDa to 533 kDa according to the isoform variation and a multi-domain structure; the central rod domain (~200 nm long) is flanked by N and C-terminal domains, which is shown as a dumbbell-like shape under electron microscopy (**Figure 1.3**) (Foisner & Wiche, 1987). Plectin plays an essential role in maintaining the structural integrity of skin, skeletal muscle, and heart; plectin (-/-) mice die 2-3 days after birth showing extensive epithelial detachment caused by keratinocyte degeneration and the loss of myofibril integrity in skeletal and heart muscle (Andra et al, 1997).

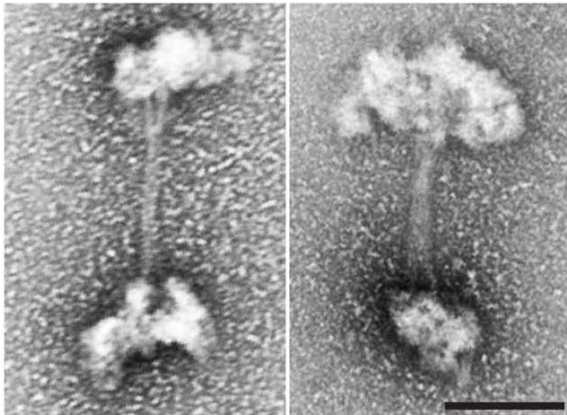


**Figure 1.3.** Negative staining electron micrographs of plectin oligomers, exhibiting dumbbell-like structure of purified plectin molecules. *Scale bar: 100 nm.* The figure was modified from (Walko et al, 2011)

#### 1.2.1.1. Domain structure of plectin and its molecular interactions

Most interactions of plectin are accomplished by N and C-terminal domains. The N-terminal domain is largely consisted of two domains: the actin-binding domain and the plakin domain. The actin-binding domain (ABD), encoded by exon 2-8, comprises a tandem pair of calponin homology domains (CH1 and CH2) and is located close to the N-terminus of plectin (**Figure 1.4**) (Fuchs et al, 1999). The sequence alignment results show that the sequence of plectin actin-binding domain has a high similarity with other cytoskeletal proteins like dystonin,  $\beta$ -spectrin, and dystrophin (Fuchs et al, 1999). In addition to the actin-binding function, the actin-binding domain interacts with other proteins such as vimentin (Sevcik et al, 2004) and integrin  $\beta 4$  (Reznicek et al, 1998). Some binding partners of the actin-binding domain regulate the actin-binding property. Phosphatidylinositol-4,5-bis-phosphate (PIP<sub>2</sub>) binds to plectin actin-binding domain, regulating its binding to F-actin (Andra et al, 1998). The integrin  $\beta 4$  binding to plectin actin-binding domain prevents the association of F-actin with plectin actin-binding domain (Geerts et al, 1999). The plakin domain, encoded by exon 9-30, is consisted of nine spectrin repeats (SR1-9) and the Src-homology 3 domain (SH3) is inserted into the middle of spectrin repeats (SR5) (**Figure 1.4**)

(Jefferson et al, 2007). The plakin domain is also involved in the interaction with integrin  $\beta 4$  (Koster et al, 2003).

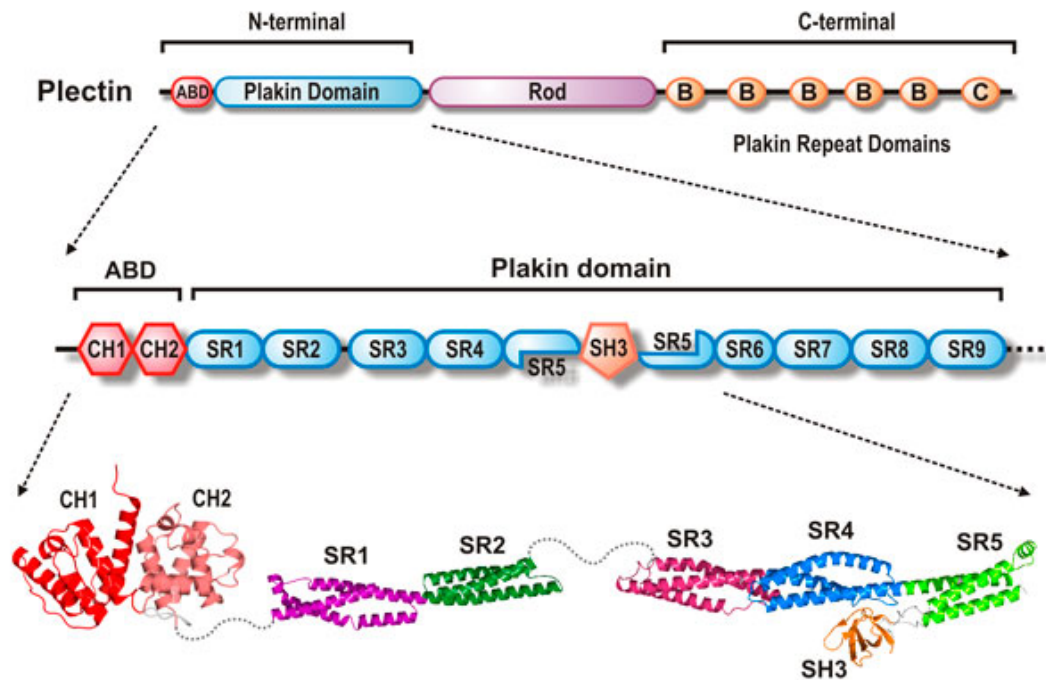


**Figure 1.4.** Schematic domain structure of plectin. Plectin can be divided into three parts: two globular N and C-terminal domains, flanked by the coiled-coil rod domain. The N-terminal domain contains the actin binding domain (ABD) and the plakin domain. The ABD is consisted of two calponin homology domains (CH1 and CH2), and the plakin domain comprises nine spectrin repeats and Src homology 3 domain. The C-terminal domain contains six plectin repeat domains (PRDs) composed of the plectin module flanked by two short linkers. The figure was modified from (Ortega et al, 2011) and (<http://xtal.cicancer.org/research.html>).

The C-terminal domain is mainly responsible for the interaction with intermediate filaments. The intermediate filament binding site of plectin is located between the C-terminal repeats 5 and 6, which was mapped to a stretch of approximately 50 amino acids

as a binding site for vimentin (Nikolic et al, 1996). In addition, the interaction with several kinds of intermediate filament proteins were identified including glial fibrillary acidic protein (GFAP) (Foisner et al, 1988), desmin (Reipert et al, 1999), and type I and II cytokeratins (Geerts et al, 1999). The central rod domain of plectin is an  $\alpha$ -helix, forming anti-parallel coiled-coil homodimers and higher order oligomers by the lateral adhesion of plectin dimers (Foisner & Wiche, 1987; Walko et al, 2011).

#### 1.2.1.2. Isoform diversity of plectin

The alternative splicing of 5'-end of the plectin gene produces a total of 16 exon variants (**Figure 1.5**), including eight kinds of first exons (1, 1a, 1b, 1c, 1d, 1e, 1f, and 1g), six non-coding first exons (0, 0a, -1, 1h, 1i, and 1j), and additional two exons (2 $\alpha$  and 3 $\alpha$ ) spliced within the actin-binding domain of plectin (Fuchs et al, 1999).

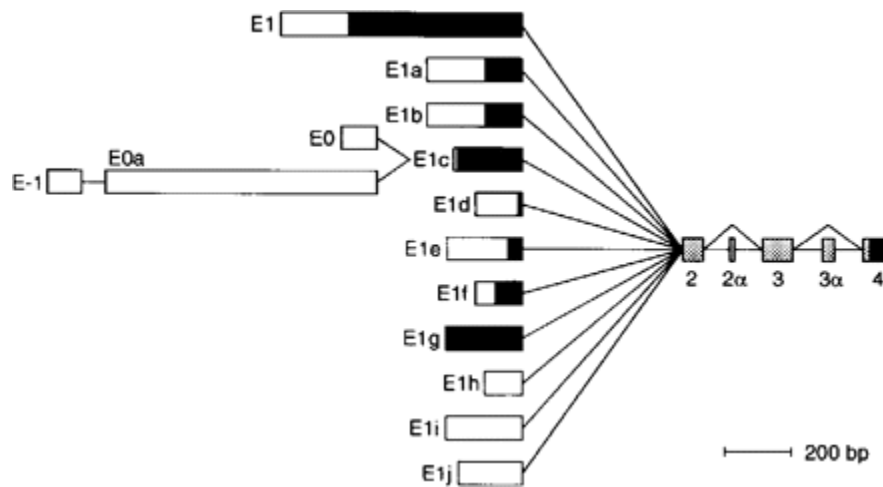


**Figure 1.5.** Schematic illustration of alternative splicing of 5'-end of the plectin gene, showing that 11 kinds of first exons are spliced into a common exon 2 and additional two exons (2 $\alpha$  and 3 $\alpha$ ) are spliced within plectin ABD. The figure was modified from (Fuchs et al, 1999).



Eleven of these are spliced into exon 2, generating isoform specific N-terminal sequences, which determine the tissue specific distribution of individual plectin isoforms, for example, plectin 1a is mostly expressed in epithelial tissues like small intestine and skin whereas plectin 1d is exclusively found in skeletal and cardiac muscles (Fuchs et al, 1999). Its subcellular localization is also dependent on N-terminal sequences. There are four identified isoforms (plectin 1, 1b, 1d, and 1f) in myofibrils; nevertheless they are respectively associated with outer nuclear membrane, mitochondria, Z-disk, and costameres (Konieczny et al, 2008; Rezniczek et al, 2007). In addition, the hemidesmosomal defect in plectin (-/-) keratinocytes is restored by the overexpression of plectin 1a, not by plectin 1c, which is co-localized with microtubules in keratinocytes (Andra et al, 2003).

#### 1.2.1.3. Human diseases related to plectin

Epidermolysis bullosa simplex combined with muscular dystrophy (EBS-MD) is the first identified disease, which is related with mutations of the human plectin gene (*PLEC*) (Chavanas et al, 1996). All EBS-MD patients suffer from the skin blistering from early childhood, whereas the progress of skeletal muscle weakness is relatively slow; most EBS-MD patient noticed the muscle weakness in twenties (Fine et al, 1991). Epidermolysis bullosa (EB) is an inherited disorder of the epithelial basement membrane, which can be largely divided into three categories based on the location where blisters occur (Eady & Dunnill, 1994). Epidermolysis bullosa simplex (EBS) is one of EB types that blisters develop at the level of the basal keratinocytes where hemidesmosomes are located (Fine et al, 1991). Various autosomal recessive mutations (at least 25 independent cases) were identified at most sites of the plectin gene, causing EBS-MD (Rezniczek et al, 2010). In contrast, EBS-Ogna is the EBS without muscle dystrophy, caused by an autosomal dominant mutation (heterozygous C-T transition at cDNA position 5998) on the plectin gene (Koss-Harnes et al, 2002; Koss-Harnes et al, 1997). In result, the Ogna mutation leads

to the Arg2000Trp substitution in central rod domain, which makes plectin vulnerable to the proteolytic degradations by calpains and other proteases in epidermis (Walko et al, 2011).

#### 1.2.1.4. Structure and function of plectin actin-binding domain

The actin-binding domain (ABD) of plectin contains two conserved calponin homology domains (CH1 and CH2) in tandem. All reported ABDs share the function, binding to F-actin with 5-50  $\mu\text{M}$  of the dissociation constant ( $K_d$ ). Each CH domain has a distinct role; CH1 is able to interact with F-actin by itself while CH2 is not (in cases of  $\alpha$ -actinin,  $\beta$ -spectrin, dystrophin, and utrophin).

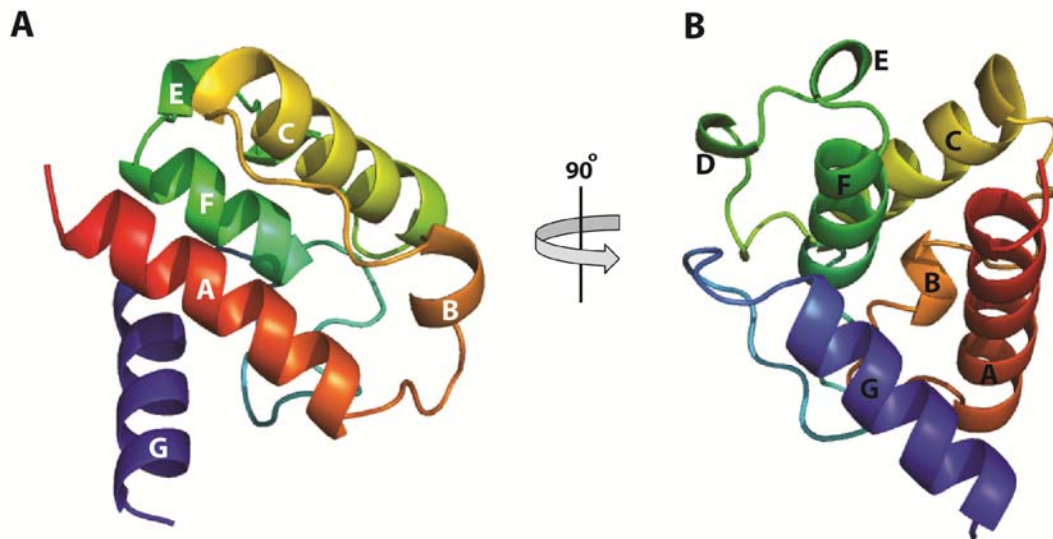


**Figure 1.6.** Structure of the calponin homology (CH) domain from human  $\beta$ -spectrin. The CH domain is composed of four major  $\alpha$ -helices (A, C, F, and G) and three minor helices (B, D, and E). The figure was generated using the coordinates in PDB(1AA2) (Djinovic Carugo et al, 1997). The helix annotations are different from the original work since the figure was produced using different program, PyMOL.

When CH1 binds alone, the affinity is 10-fold lower than entire ABD, demonstrating the cooperative role of CH2 in F-actin binding (Way et al, 1992). The calponin homology domain consists of four main helices (A, C, E, and G) and three short minor helices (B, D, and F) (**Figure 1.6**) (Djinovic Carugo et al, 1997). Biochemical and structural studies found that there are three actin-binding sites mostly consisted of hydrophobic residues (ABS1, 2, and 3) in actin-binding domains; ABS1 is located at the A-helix of CH1 and ABS2 comprises F and G helices in CH1, whereas CH2 contains ABS3 at the first helix (Bresnick et al, 1990; Levine et al, 1990) (**Figure 1.7**).

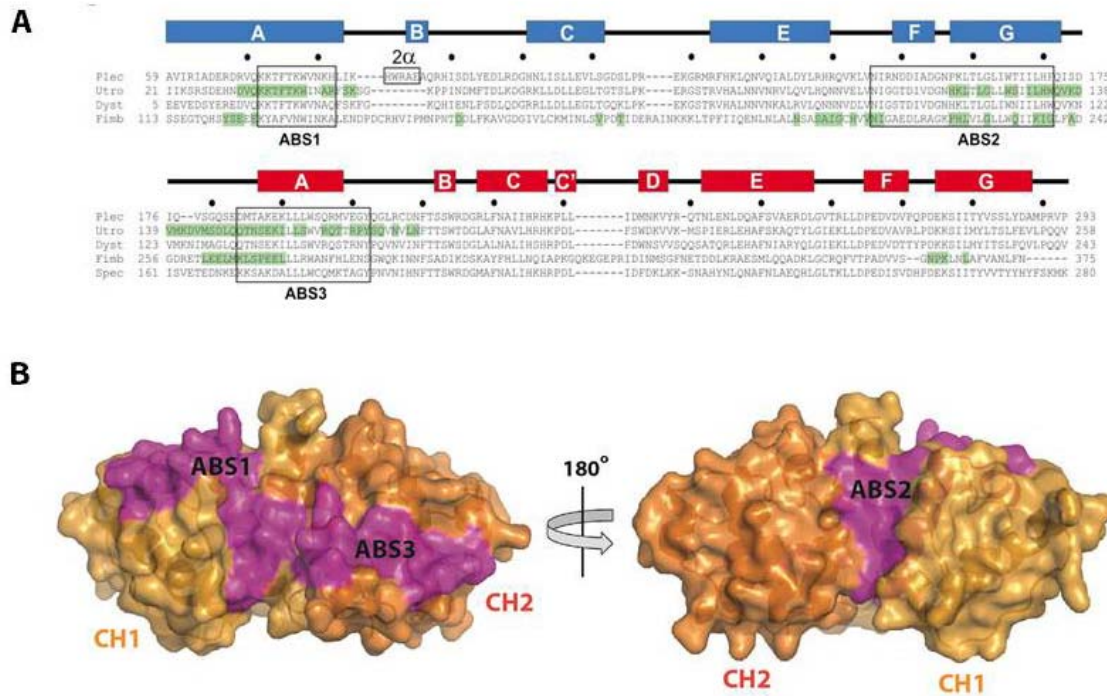


**Figure 1.7. (A)** The amino acid sequence of plectin ABD is aligned with utrophin, dystrophin, and fimbrin ABDs. Actin-binding sites are depicted as ABS1, 2, and 3. The figure was reproduced from (Garcia-Alvarez et al, 2003). **(B)** Three actin-binding sites are shown in magenta on the structure of plectin actin-binding domain (PDB:1MB8) (Garcia-Alvarez et al, 2003). CH1 domain contains ABS1 and ABS2, and CH2 domain comprises ABS3.

The structures of human and mouse plectin actin-binding domains were determined by X-ray crystallography (Garcia-Alvarez et al, 2003; Sevcik et al, 2004). Plectin actin-binding domain shows the similar actin binding affinity like other reported actin-binding domains ( $22.3 \mu\text{M}$  of  $K_d$ ) (Garcia-Alvarez et al, 2003). The structural studies on actin-binding domains have shown that actin-binding domains can adopt either open or closed conformations; the crystal structures of utrophin and dystrophin actin-binding domains were found in an open conformation, while actin-binding domains of plectin,  $\alpha$ -actinin, and fimbrin exhibit a closed conformation. Plectin,  $\alpha$ -actinin, and fimbrin actin-binding domains change the conformation upon the F-actin binding, leading to a relaxation of the CH1-CH2 interaction (Galkin et al, 2010; Moores et al, 2000). The structure of plectin CH1 shows a high similarity with utrophin and dystrophin (the root-mean-square deviation of 0.43 and 0.50 Å over equivalent 47 C $\alpha$  atoms in CH1, respectively) and CH2 is also in good agreement with other actin-binding domains like  $\beta$ -spectrin and utrophin (Garcia-Alvarez et al, 2003). One notable feature of plectin actin-binding domain is that it contains an additional helix encoded by exon 2 $\alpha$  after A-helix of CH1, which contributes to a higher affinity to F-actin than other actin-binding domain variants lacking exon 2 $\alpha$  (Fuchs et al, 1999). The plectin isoforms containing exon 2 $\alpha$  are dominant in heart and skeletal muscles, suggesting the role of the exon 2 $\alpha$  insertion to modulate the actin binding capacity in those tissues.

## 1.2.2. Integrin $\alpha 6\beta 4$

### 1.2.2.1. Integrins

Integrins are hetero-dimeric receptors for cell adhesion to extracellular matrix proteins, consisting of non-covalently associated  $\alpha$  and  $\beta$  subunits; 18  $\alpha$  chains and 8  $\beta$  chains have been identified so far, which form 24 functional pairs (**Figure 1.8**) (Clark & Brugge, 1995; Hynes, 2002; Schwartz et al, 1995).

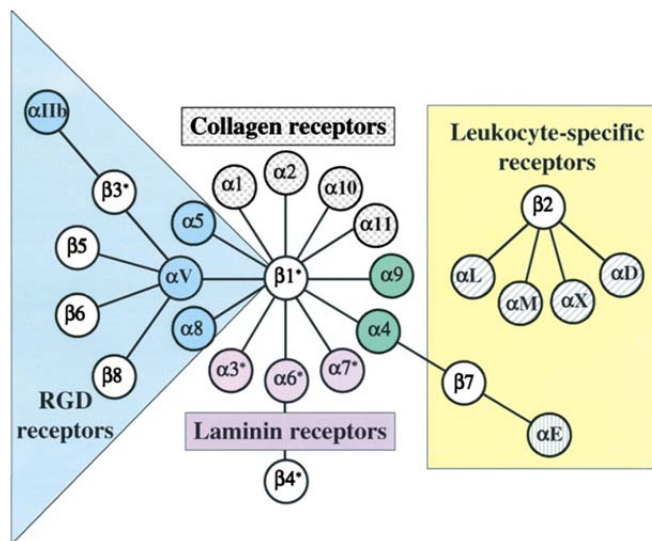


**Figure 1.8.** The integrin receptor diversity. The figure demonstrates possible combinations of 18  $\alpha$  and 8  $\beta$  subunits, generating 24 integrin heterodimers, which can be classified into 4 families: RGD, collagen, laminin, and leukocyte-specific receptors. The figure was modified from (Hynes, 2002)

Each integrin pair has a specific function and shows ligand specificity. Integrins are transmembrane glycoproteins that function as a mechanical linker between extracellular matrix and cytoskeletons. The cytoplasmic parts of integrins are linked to actin filaments except integrin  $\alpha 6\beta 4$  that connects to intermediate filaments (Tamura et al, 1990). In addition to the function for the linkage between extracellular matrix and cytoskeletal networks, integrins transduce a variety of signals, modulating many aspects of cell behavior including proliferation, survival, apoptosis, shape, polarity, motility, gene expression, and differentiation (**Figure 1.9**) (Hynes, 2002; Shattil et al, 2010). As depicted in **Figure 1.9**, there are two directions of integrin signaling. When extracellular ligands bind to integrins, it leads to the conformational change or clustering of integrins, consequently, transmitting signals from the extracellular matrix into the cell. This mechanism is called 'outside-in' integrin signaling (Schwartz et al, 1995; Shattil et al, 2010). For example, the activation of leukocytes is regulated by adhesion to the extracellular matrix. Secretion of cytokines such as IL-1 $\beta$  in monocytes is stimulated by integrin-mediated adhesion of integrins with antibodies (Pacifi et al, 1992). Differentiation and gene expression are regulated by the contact with extracellular proteins in many cell types (Schwartz et al, 1995).

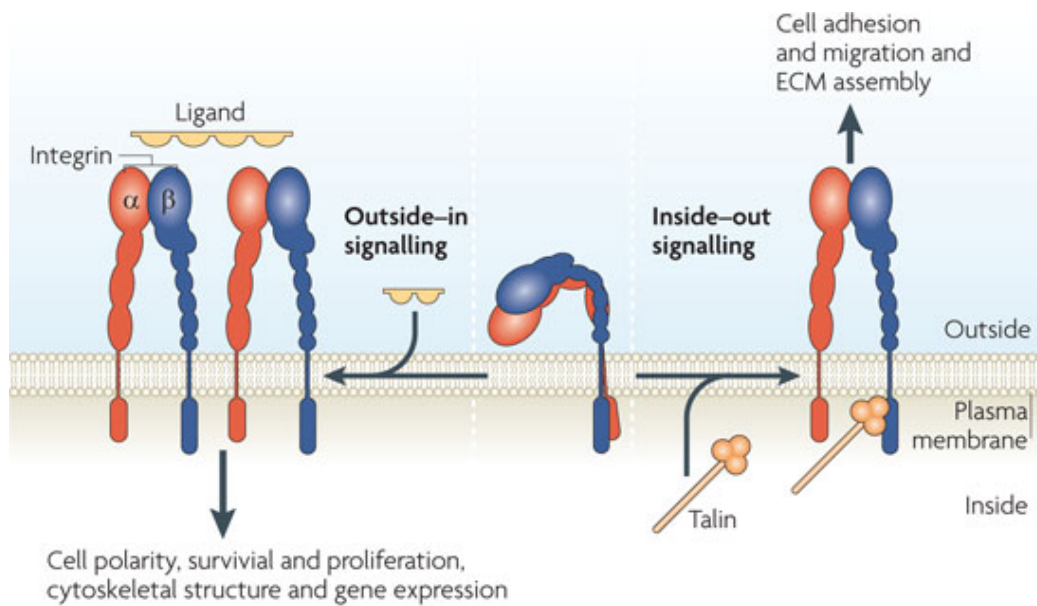


**Figure 1.9.** There are two directions of integrin signaling: ‘inside-out’ and ‘outside-in’. The figure exhibits that ligands can bind to either the cytosolic domain or the extracellular domain of integrins, causing bidirectional integrin signaling. The figure was modified from (Shattil et al, 2010)

The ‘inside-out’ integrin signaling is caused by the binding of cytosolic activators like talin and kindlin to cytosolic domains of integrins (Moser et al, 2009). For example, talin binds to the cytoplasmic domain of the  $\beta$ -integrin subunit, and activates  $\beta 1$  and  $\beta 3$  integrins (Tadokoro et al, 2003). Two point mutations (Y747A and L746A) in the  $\beta 3$  integrin tail prevent the interaction with talin. Mice harboring these mutations are defective in the  $\alpha \text{IIb} \beta 3$  integrin activation (abundantly present in platelets) and resistant from thrombosis, proving that the ‘inside-out’ signal by talin binding is required for the  $\alpha \text{IIb} \beta 3$  integrin activation (Petrich et al, 2007).

### 1.2.2.2. Integrin domain structures and the interactions

Each subunit of integrin can be divided into three parts: a large extracellular segment (~1000 residues for  $\alpha$  and ~750 residues for  $\beta$ ), a transmembrane segment, and a short cytoplasmic C-terminal tail (~50 residues) (**Figure 1.10A**).

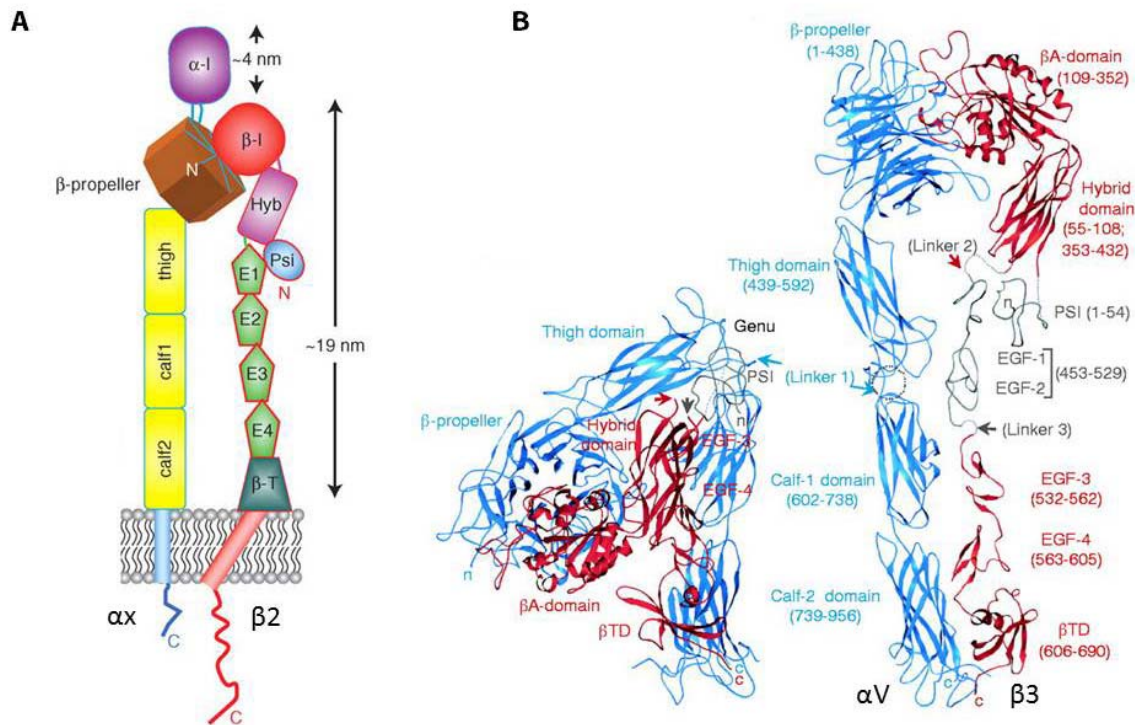


**Figure 1.10. (A)** Schematic presentation of the integrin  $\alpha\beta_2$  structure. The figure was modified from (Campbell & Humphries, 2011). **(B)** The crystal structure of the extracellular segment of integrin  $\alpha_V\beta_3$ . The extracellular part of  $\alpha_V$  subunit consists of a  $\beta$ -propeller (with seven blades), a thigh, and two calf domains (calf 1 and 2). The extracellular part of  $\beta_3$  subunit comprises a  $\beta$ A domain, a hybrid domain, a plexin-semaphorin-integrin (PSI) module, four epidermal growth factor (EGF) modules, and a  $\beta$ -tail domain ( $\beta$ TD). The figure was modified from (Xiong et al, 2001).



The crystal structure of the extracellular segment of integrin  $\alpha V\beta 3$  was solved in a ‘bent and closed’ conformation (**Figure 1.10B**) (Xiong et al, 2001). In that conformation, ligands like fibronectin can bind to integrin  $\alpha V\beta 3$ ; the RGD (Arg-Gly-Asp) motif of fibronectin binds into the crevice between the  $\beta$ -propeller and  $\beta A$  domains on the integrin head (Xiong et al, 2002). The ligand binding induces the ‘outside-in’ activation of integrin  $\alpha V\beta 3$ , releasing a ‘deadbolt’, the elongated CD loop of  $\beta TD$  that locks the  $\alpha 7$  helix of  $\beta A$ -domain in a bent conformation, and then it changes to an ‘extended and open’ conformation (Xiong et al, 2003). The structure of the complex of  $\alpha IIb\beta 3$  transmembrane helices in an inactive state was solved by NMR, showing that the complex is stabilized by glycine-packing within the outer membrane leaflet and by electrostatic and hydrophobic interactions in the inner membrane leaflet (**Figure 1.11A**) (Lau et al, 2009). Together with the structural study on the  $\beta 3$ -cytoplasmic tail/talin F3 complex (Wegener et al, 2007), these results suggest that talin F3 binding induces the dissociation of transmembrane helices of integrin  $\alpha IIb\beta 3$  and transduces the ‘inside-out’ signal (**Figure 1.11B**).

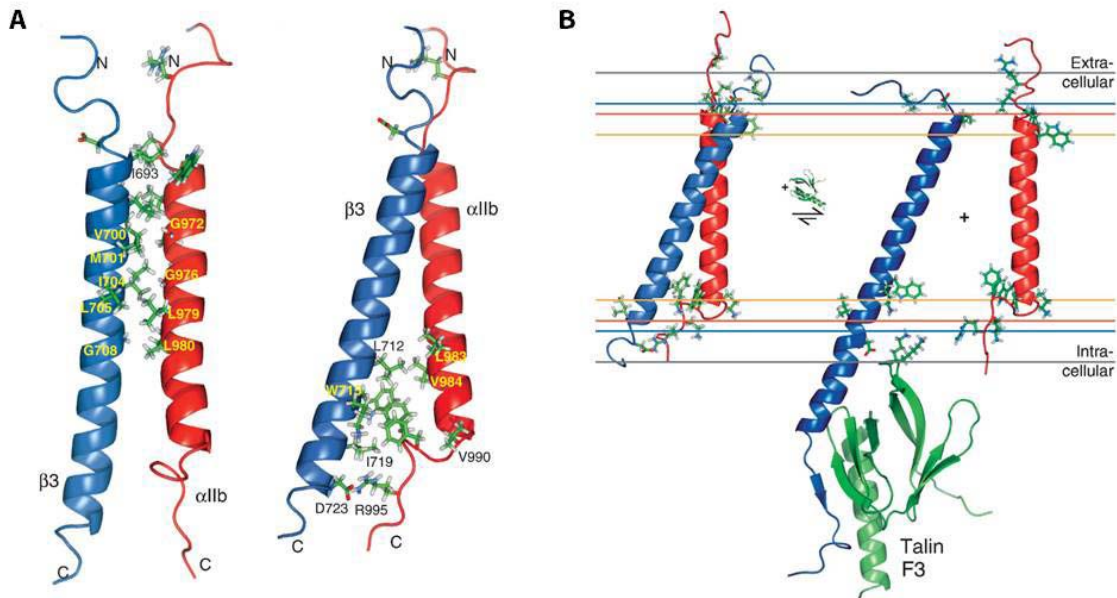


**Figure 1.11. (A)** Structure of the integrin  $\alpha IIb\beta 3$  transmembrane complex. **(B)** The proposed model of the ‘inside-out’ integrin signaling by talin F3 binding. The figures were modified from (Lau et al, 2009).



#### 1.2.2.3. Integrin $\alpha 6\beta 4$

The  $\alpha 6$  subunit can associate with either  $\beta 1$  or  $\beta 4$ ; however,  $\alpha 6$  preferentially binds to  $\beta 4$  in many epithelial cells (Hemler et al, 1989) and integrin  $\alpha 6\beta 4$  is specifically located at the hemidesmosomes (Sonnenberg et al, 1991; Stepp et al, 1990). The  $\beta 4$  subunit has an exceptionally long and unique cytoplasmic domain (more than 1000 residues), providing the function for the interaction with the intermediate filaments, which differ from other integrins usually associated with actin filaments (Suzuki & Naitoh, 1990; Tamura et al, 1990). The essential role of  $\alpha 6\beta 4$  in hemidesmosomes has been demonstrated by several functional studies (Georges-Labouesse et al, 1996; Vidal et al, 1995). The absence of  $\beta 4$  causes junctional epidermolysis bullosa, one type of epidermolysis bullosa that blisters occur within basement membranes due to the lack of functional hemidesmosomes (Eady & Dunnill, 1994; Vidal et al, 1995). In addition, the lack of  $\alpha 6$  also leads to the severe skin blistering and neonatal death in mice (Georges-Labouesse et al, 1996). Integrin  $\alpha 6\beta 4$  is the receptor for several laminins, major components of the basement membrane (Lee et al, 1992). Particularly, laminin-322 (previously termed laminin-5) plays a role in the formation and stabilization of hemidesmosomes (Baker et al, 1996). The interaction of integrin  $\alpha 6\beta 4$  with plectin is crucial for the stable assembly of hemidesmosomes. Two different mutations (Arg1225His and Arg1281Trp) in the second fibronectin type III domain, found in patients with non-lethal form of epidermolysis bullosa, interfere the interaction with plectin (Koster et al, 2001).

#### 1.2.2.4. Structure of the fibronectin type III domain

The cytoplasmic part of  $\beta 4$  subunit is consisted of two pairs of fibronectin type III (FN-III) domains separated by the connecting segment (Suzuki & Naitoh, 1990). Fibronectin type III domains (~90 residues) are found in many proteins including adhesion molecules, cytokine receptors, and extracellular matrix proteins. One of the well-known functions is

that the RGD (Arg-Gly-Asp) motif in several FN-III domains binds to RGD integrin receptors, which mediates numerous cell adhesion processes such as thrombosis and inflammation (Ruoslahti & Pierschbacher, 1987). The fibronectin type III domain has a conserved  $\beta$ -sandwich fold, consisted of two  $\beta$ -sheets enclosing a hydrophobic core; one with three strands (A, B, and E) and another with four strands (C, C', F, and G) (**Figure 1.12**) (Leahy et al, 1992).

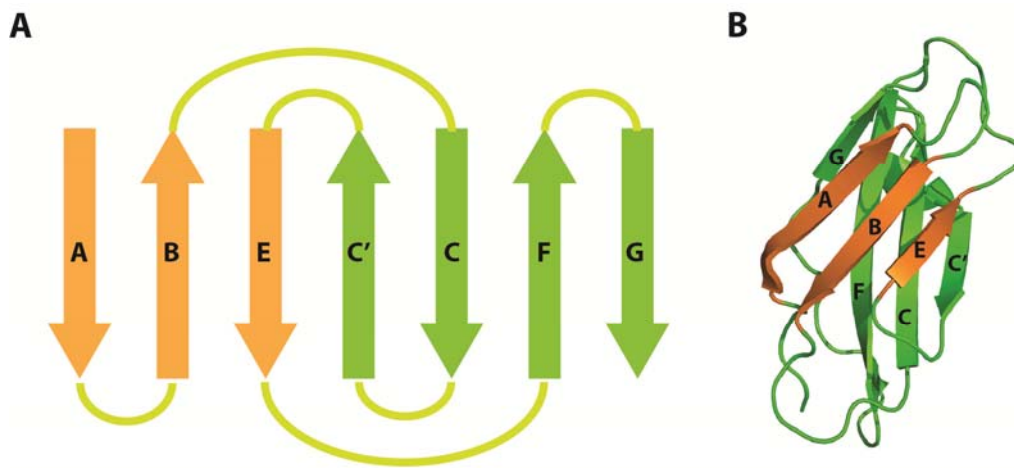


**Figure 1.12. (A)** Schematic diagrams of the fibronectin type III domain from human integrin  $\beta 4$ . **(B)** The structure shows a  $\beta$ -sandwich fold, composed of two  $\beta$ -sheets: one is consisted on A, B, and E  $\beta$ -strands, another comprises C, C', F, and G  $\beta$ -strands. The figure was generated from the structure of the second fibronectin type III domain of integrin  $\beta 4$  using PDB (1QG3) (de Pereda et al, 1999).

The crystal structure of a tandem pair of fibronectin type III domains from the  $\beta 4$  subunit shows that two FN-III domains of the  $\beta 4$  integrin are quite similar (root-mean-square deviation of 1.3 Å over 58 C $\alpha$  atoms) and lacking the RGD sequence in the F-G loop (de Pereda et al, 1999). The crystal structure of the integrin  $\beta 4$  fragment in complex with plectin 1c actin-binding domain was determined, demonstrating the structural basis of the interaction (de Pereda et al, 2009). The crystal structure exhibits that two residues

(Arg1225 and Arg1281), mutated in patients with epidermolysis bullosa, are critical for the interaction with plectin actin-binding domain, making salt bridges respectively with plectin Asp155 and Glu95. The interaction studies show that the connecting segment (CS) plays a role in the binding to plectin actin-binding domain; the mutant lacking the connecting segment shows a weaker affinity than other constructs having a partial connecting segment (de Pereda et al, 2009).

### 1.3. The plectin/integrin $\beta 4$ complex in hemidesmosomes and its regulation by phosphorylation

Although hemidesmosomes are adhesive protein complexes mediating the firm attachment of the basal layer of epithelial cells to underlying basement membrane, hemidesmosomes are regulated since their components are rearranged when cells detach from the basement membrane during processes such as cell migration or differentiation. (Litjens et al, 2006). There are two binding sites between plectin and integrin  $\beta 4$ . The first binding interface of the plectin/integrin  $\alpha 6\beta 4$  complex is established between plectin actin-binding domain and the first pair of fibronectin type III domain including the N-terminal part of the connecting segment (**Figure 1.13**) (Geerts et al, 1999; Rezniczek et al, 1998), which is sufficient for the localization of  $\alpha 6\beta 4$  in hemidesmosomes (Niessen et al, 1997). The phosphorylation of three serine residues (Ser1356, Ser1360, and Ser1364) located in the connecting segment, induced by protein kinase A and C (PKA or PKC) under epidermal growth factor (EGF) stimuli, causes the partial disassembly of hemidesmosomes in keratinocytes (Rabinovitz et al, 2004; Wilhelmsen et al, 2007). Additionally it was found that only two serine residues (Ser1356 and Ser1364) are phosphorylated by extracellular signal regulated kinases (ERK) 1/2 and p90 ribosomal s6 kinases (p90RSK) 1/2 under PMA and EGF stimuli, leading to the destabilization of the integrin  $\beta 4$  binding to plectin (Frijns et al, 2010).

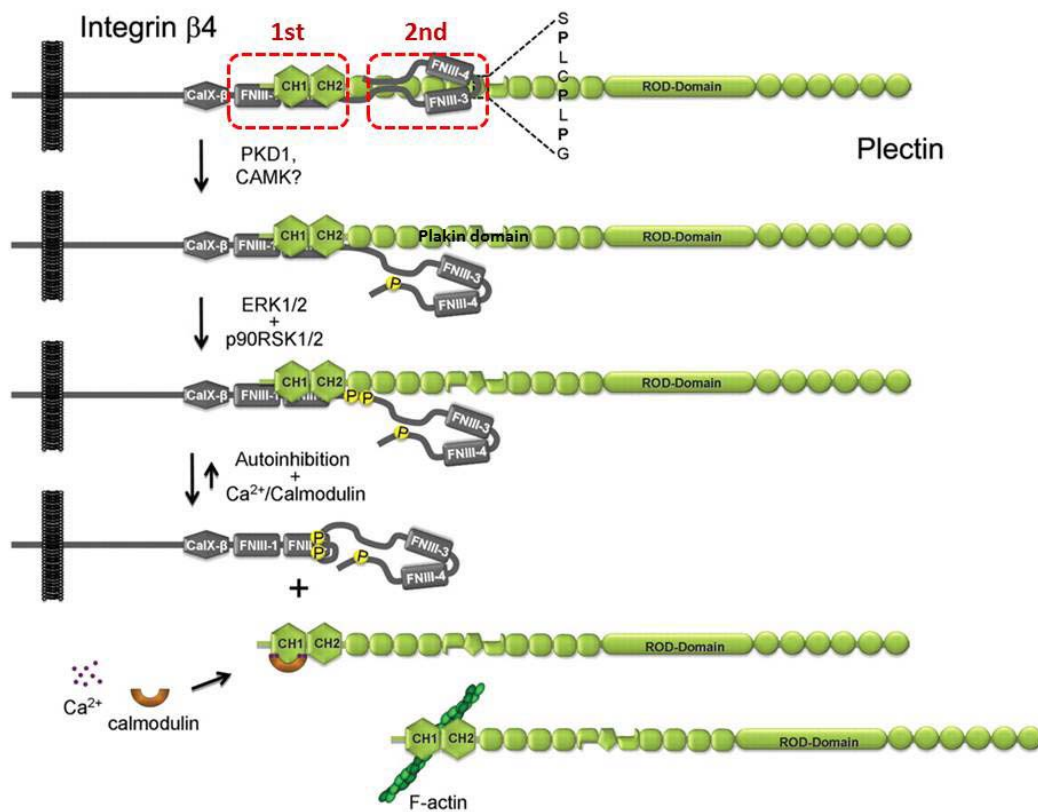


**Figure 1.13.** Putative model for the hemidesmosome disassembly driven by the phosphorylation on integrin  $\beta 4$  and the binding of calmodulin to plectin. The phosphorylation on Thr1736 disrupts the interaction with the plakin domain of plectin (2<sup>nd</sup> site), and the additional phosphorylation on Ser1356 and Ser1364 prevents the binding with plectin ABD (1<sup>st</sup> site). CaM binding to plectin ABD contributes the disassembly along with the phosphorylation on integrin  $\beta 4$ . The figure was modified from (Frijns et al, 2012).

The second interfacing site is between the plakin domain of plectin and loop regions of integrin  $\beta 4$  including the C-terminal part of the connecting segment and the C-terminal tail (**Figure 1.13**) (Geerts et al, 1999; Koster et al, 2004; Reznicek et al, 1998). Thr1736 residue in the C-terminal tail is phosphorylated by PKD1, which is a downstream event of PKC and EGF receptor activation. The phosphorylation on Thr1736 prevents the

interaction between the plakin domain of plectin and the C-terminal tail of integrin  $\beta 4$  (Frijns et al, 2012). The integrin  $\beta 4$  binding to plectin is strictly regulated by the phosphorylation on aforementioned serine residues in the connecting segment and Thr1736 in the C-terminal tail, which respectively diminish the interaction with plectin actin-binding domain and plectin plakin domain.

#### 1.4. Calmodulin regulation of the plectin/integrin $\beta 4$ complex

Calcium-calmodulin regulates the binding of plectin to integrin  $\beta 4$  in an isoform-specific manner (Kostan et al, 2009). Among three plectin isoforms (1a, 1c, and 1f) tested, calcium-calmodulin only binds to plectin isoform 1a that is specifically present in hemidesmosomes (Andra et al, 2003). Calmodulin binding to plectin 1a actin-binding domain (plectin 1aABD) reduces the binding affinities of plectin 1aABD with integrin  $\beta 4$  and F-actin, demonstrating that calmodulin also regulates the plectin/integrin  $\beta 4$  interaction together with the phosphorylation and contributes the hemidesmosome disassembly.

##### 1.4.1. Calmodulin

Calmodulin (CaM) is a cytosolic calcium chelating protein (148 amino acid residues) that modulates a plenty of calcium-dependent cellular processes upon binding to its partners. The calcium concentration in cytosol is maintained at 0.1  $\mu\text{M}$ . When the cytosolic calcium concentration is approximately 100-fold increased upon stimuli such as inositol-1,4,5-triphosphate (InsP3) or cyclic ADP-ribose (Berridge, 1993; Galione & White, 1994), calmodulin binds four calcium ions with high affinity ( $K_d$  of 1~10  $\mu\text{M}$ ) (Crivici & Ikura, 1995). Calmodulin is ubiquitously present in eukaryotic cells and more than hundred binding partners have been reported. Functions of calmodulin binding partners are modulated by

calmodulin binding, for examples, myosin light chain kinases, brain adenylate cyclase, ATPase, and  $\text{Ca}^{2+}$  pump of erythrocyte membrane (Crivici & Ikura, 1995). Calmodulin possesses two similar lobes: N-terminal and C-terminal lobes. The calcium binding affinity of each lobe is different; C-lobe ( $K_d$ :  $\sim 0.2 \mu\text{M}$ ) exhibits a 10-fold higher affinity than N-lobe ( $K_d$ :  $\sim 2 \mu\text{M}$ ), causing that calcium first binds to the C-lobe and subsequently to the N-lobe (Potter et al, 1983; Yazawa et al, 1987). Calcium binding to each lobe of calmodulin independently occurs; however, calcium binding to each lobe becomes co-related in the presence of the binding partner. Calcium binding to the C-lobe leads to the cooperative calcium binding to N-lobe; consequently, the calcium binding affinity of calmodulin is increased (Yazawa et al, 1987). Due to the cooperation between two lobes, calmodulin can activate many cellular signals at very low calcium concentration.

#### 1.4.2. Various conformations of calmodulin

Two lobes of calmodulin (N and C terminal lobes) are separated by a linker (76-84 residues), and each lobe comprises a pair of EF-hand (helix-loop-helix) motif (Babu et al, 1985). The conformational change of calmodulin upon calcium binding was measured by several methods such as small angle X-ray scattering (SAXS) and circular dichroism (CD) spectroscopy. The SAXS studies reveal that calcium-calmodulin shows  $21.3 \text{ \AA}$  of  $R_g$  (radius of gyration) and  $63 \text{ \AA}$  of  $D_{\text{max}}$  (maximum distance), calculated by pair distribution functions, whereas apo-calmodulin (calcium-free calmodulin) exhibits  $19.6 \text{ \AA}$  of  $R_g$  and  $59 \text{ \AA}$  of  $D_{\text{max}}$ , indicating that a conformational change caused by calcium binding leads to the increase of the overall shape of calcium-calmodulin compared to apo-calmodulin (Heidorn & Trewhealla, 1988). The circular dichroism analyses show that the  $\alpha$ -helical content is increased when calcium binds (Klevit et al, 1985). The high resolution structures of apo-calmodulin and calcium-calmodulin were respectively solved by NMR and X-ray crystallography, revealing the conformational change of calmodulin in detail triggered by calcium binding to each EF-hand motif (Babu et al, 1985; Kuboniwa et al, 1995).

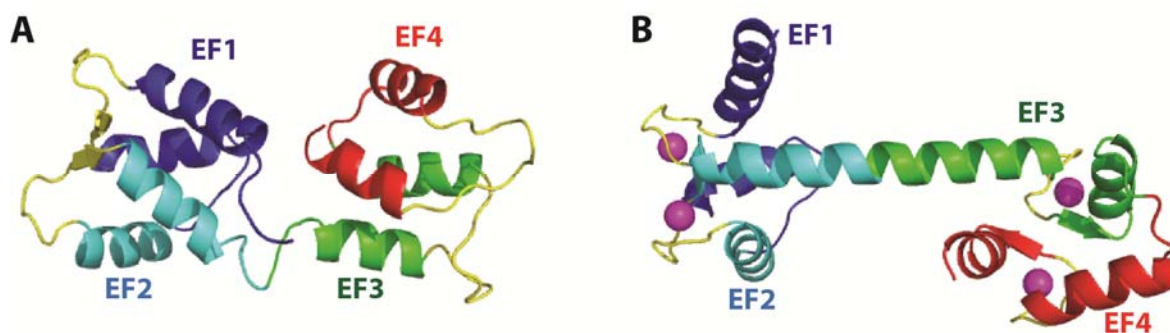


**Figure 1.14.** Conformational change of calmodulin upon  $\text{Ca}^{2+}$  binding. **(A)** Four helices are tightly packed in each lobe of apo-calmodulin. The figure was generated using the PDB (1CFC) worked by (Kuboniwa et al, 1995). **(B)** Calcium-calmodulin shows an extended conformation, exposing the hydrophobic core of each lobe. Calcium ions are shown as magenta spheres. The figure was generated using the PDB (3CLN) (Babu et al, 1988).

As shown in **Figure 1.14A**, apo-calmodulin contains two globular lobes separated by a flexible linker and each domain is consisted of tightly packed four anti-parallel  $\alpha$ -helices. The hydrophobic residues, which are responsible for the binding to partners, are varied, exhibiting a closed conformation; calmodulin possesses nine methionine residues (6.1%) comprising the hydrophobic core and generating strong van der Waals interactions with binding partners (Crivici & Ikura, 1995). On the contrary, calcium-calmodulin shows a dumbbell-like extended conformation, exposing the hydrophobic core (**Figure 1.14B**). Each EF-hand motif contains one calcium ion and the inter-lobe linker adopts a helical conformation. The interlobe linker varies in rigidity and length, enabling to accommodate the different conformation of calcium-calmodulin upon binding to various binding partners.

#### 1.4.3. Target recognition of calmodulin

The binding of calmodulin to target proteins induce an additional conformation change of calcium-calmodulin. The initial conformational change occurs upon calcium binding as mentioned above. The second conformational change is caused by anchoring to hydrophobic residues in an  $\alpha$ -helix of the binding partner, meaning that the conformation varies based on the arrangement of hydrophobic residues in binding partners (Hoeftlich & Ikura, 2002). Such an adaptive conformation of calmodulin is granted by largely two factors. First, calmodulin can adopt different conformations due to the flexibility of the interlobe linker (Heidorn & Trewhella, 1988). The second factor that affects the conformational flexibility is the adjustment of the flexible and hydrophobic methionine residues in each lobe for the binding. The calmodulin recognition motif can be classified based on the positions of two major hydrophobic residues that anchor to each lobe such as 1-10, 1-14, 1-16, and IQ (isoleucine and glutamine) motifs (Rhoads & Friedberg, 1997). These motif groups can be divided into subgroups, considering additional hydrophobic residues in the middle. For examples, the 1-14 motif class comprises the 1-5-8-14 motif, characterized for calcineurin and skeletal muscle myosin light chain kinase (skMLCK) and the 1-8-14 motif, found in smooth muscle myosin light chain kinase (smMLCK) and caldesmon (Rhoads & Friedberg, 1997).

#### 1.4.4. Calmodulin complexes

A number of structures of calmodulin in complex with binding partners were determined and calmodulin conformations can be largely classified into two types: collapsed and extended conformations (Vetter & Leclerc, 2003). **Figure 1.15** shows some examples of adaptive conformational changes of calcium-calmodulin.



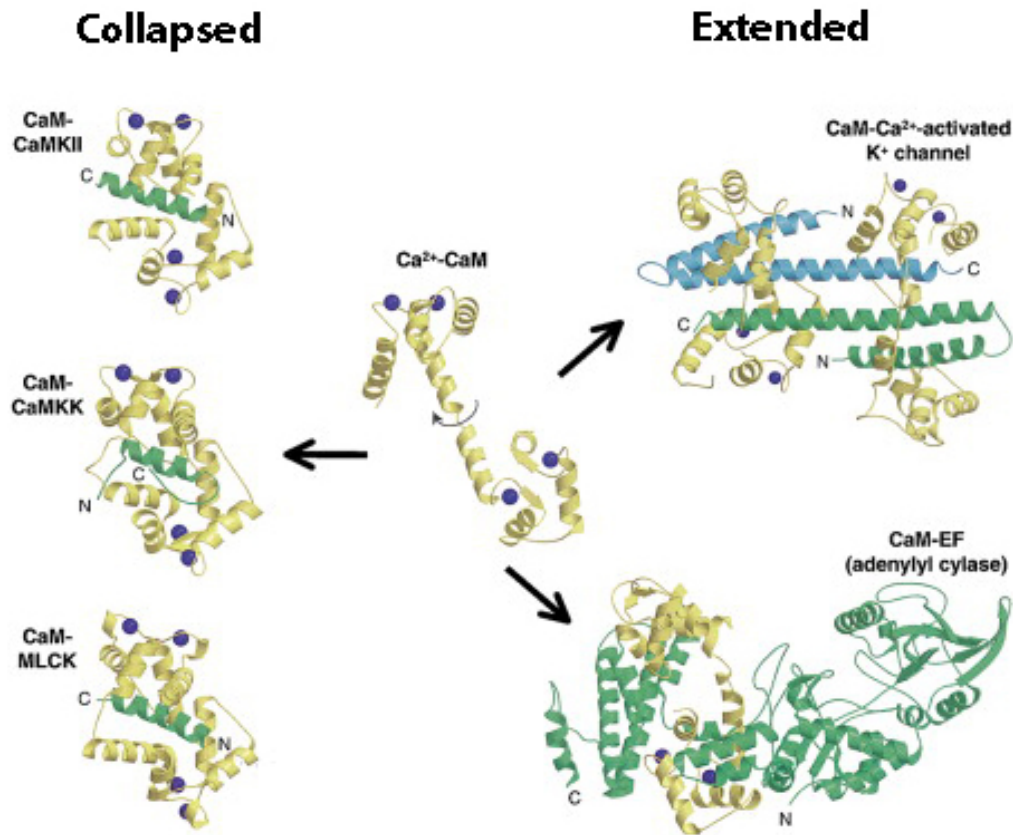


**Figure 1.15.** Calmodulin in different conformations. Calmodulin changes the conformation upon binding to partners; the left panel shows collapsed conformations with peptides from calmodulin-dependent protein kinase II (CaMKII), calmodulin-dependent protein kinase kinase (CaMKK), and smooth muscle myosin light chain kinase (smMLCK), and the right panel displays extended conformations of CaM with the CaM binding domain (CaMBD) of small conductance Ca<sup>2+</sup>-activated K<sup>+</sup> channel and oedema factor (EF, calmodulin-activated adenylyl cyclase). The figure was modified from (Hoeftlich & Ikura, 2002).

The collapsed conformation is found in many calmodulin/peptide complexes such as calmodulin/calmodulin dependent protein kinase II (CaMKII), calmodulin/calmodulin

dependent protein kinase kinase (CaMKK), and calmodulin/smooth muscle myosin light chain kinase (smMLCK).

In a closed conformation, the interlobe linker, shown as an  $\alpha$ -helix in the crystal structure of calcium-calmodulin, is divided into two short helices or becomes disordered, enabling two lobes to form a hydrophobic channel and to engulf the target peptides. In the case of the calmodulin/melittin (venom peptide) complex, apo-calmodulin and calcium-calmodulin show respectively 19.46 Å of  $R_g$  and 20.17 Å of  $R_g$  whereas the calmodulin/peptide complex exhibits 18.01 Å of  $R_g$ , indicating that the overall shape of the complex is more compact than apo-calmodulin and calcium-calmodulin (Kataoka et al, 1989). The calmodulin binding with a 1:1 stoichiometry in a collapsed conformation is called a 'canonical binding' of calmodulin (Hoeflich & Ikura, 2002).

An extended conformation of calmodulin means that calmodulin exhibits a similar extended conformation as the crystal structure of calcium-calmodulin; however, the interlobe linker is disrupted as found in a closed conformation. The binding of calmodulin in an extended conformation seems to have more possible ways for the interactions. As shown in **Figure 1.15**, the calmodulin forms active tetrameric complex with the calmodulin binding domain (CaMBD) of small conductance  $\text{Ca}^{2+}$ -activated  $\text{K}^+$  channel 2 in a stoichiometry of 2:2 (Schumacher et al, 2001); the CaMBD has two  $\alpha$ -helices and it forms an anti-parallel dimer with calmodulin. The crystal structure of the calmodulin/CaMBD complex shows that calmodulin remains in an extended conformation and binds to three  $\alpha$ -helices of CaMBD: one lobe to two  $\alpha$ -helices and another lobe to one  $\alpha$ -helix. The second example in **Figure 1.15** is the calmodulin/oedema factor (EF) complex. Oedema factor is a calmodulin-activated adenylyl cyclase, contributing to both cutaneous and systemic anthrax (Dixon et al, 1999). The catalytic part of EF comprises three globular domains:  $\text{C}_A$ ,  $\text{C}_B$ , and the helical domain. Calmodulin inserts between  $\text{C}_A$  and the helical domain in an extended conformation, causing a translation and a rotation of the helical domain away from the catalytic core and leading to the enzyme activation. Interestingly,

N-lobe of calmodulin does not contain  $\text{Ca}^{2+}$  and remains closed, and C-lobe interacts with H-helix of EF containing a 1-5-10 motif (Drum et al, 2002). Similarly, in the case of the calmodulin/C20W (the N-terminal calmodulin binding domain of plasma membrane  $\text{Ca}^{2+}$  pump) peptide complex, only C-lobe binds to C20W possessing a 1-5-8 motif and calmodulin exhibits an extended conformation owing to the lack of an anchor residue at 14 position in C20W peptide (Elshorst et al, 1999).

## 2. THE AIM OF THE STUDY

Calmodulin plays an important role in hemidesmosome regulation; calcium-calmodulin binds to plectin 1a located in hemidesmosomes, leading to the disruption of the plectin/integrin  $\beta 4$  complex and contributing the hemidesmosome disassembly. Recent studies revealed that calmodulin binds to plectin in an isoform-specific manner (Kostan et al, 2009); however, previous studies have not elucidated the binding region of calmodulin on plectin 1a and the role of the N-terminal isoform specific extension for the calmodulin binding. In addition, the molecular mechanism of calmodulin binding to plectin has not been examined. The interaction of plectin and integrin  $\beta 4$  is regulated by the phosphorylation on several sites of integrin  $\beta 4$ , as well as by calmodulin which only binds to plectin isoform 1a to modulate the interaction (Frijns et al, 2012). The overall aim of the study is to understand this isoform specific regulation on the plectin 1a/integrin  $\beta 4$  at molecular level.

The goal of my study is to elucidate the structural basis of the dissociation of the plectin 1a/integrin  $\beta 4$  complex driven by calcium-calmodulin binding. To achieve this aim, studies on the plectin 1a actin-binding domain/calmodulin complex and the plectin 1a actin-binding domain/integrin  $\beta 4$  complex have been carried out by structural approaches including X-ray crystallography and small angle X-ray scattering, combined with cross-linking/mass spectrometry analyses and isothermal titration calorimetry. The results obtained during my PhD study present the first structural insight into the calcium-calmodulin regulation of the hemidesmosome disassembly and propose a molecular model for the hemidesmosome disassembly modulated by calcium-calmodulin.

### 3. RESULTS

#### 3.1. Structural studies on plectin 1a actin-binding domain

##### 3.1.1. Construct design

The plectin construct named P1aABD is designed to contain the N-terminal tail and the actin-binding domain of plectin isoform 1a (amino acid residues 1-263, **Figure 3.1**) to study the interaction with calmodulin (Kostan et al, 2009).

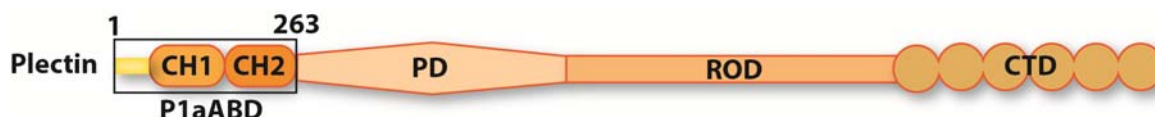


**Figure 3.1.** Schematic illustration of plectin. The P1aABD construct (1-263) contains the N-terminal tail and the actin-binding domain of plectin. The abbreviations correspond to the followings; ABD: actin-binding domain, PD: plakin domain, ROD: coiled-coil rod domain, CTD: C-terminal domain.

##### 3.1.2. Purification of plectin 1aABD constructs

Plectin constructs were expressed in *E.coli* Rosetta2 (DE3) pLysS cells. Protein samples were initially purified by affinity chromatography with a HisTrap HP column (GE Healthcare). After histag cleavage by 3C protease, samples were introduced again to a HisTrap HP column (GE Healthcare). Unbound fractions were collected and further purified using a Superdex 75 26/60 gel filtration column (GE Healthcare) (**Figure 3.2A**). The fractions of the peak corresponding to the molecular weights of 22~28 kDa were collected, indicating that plectin variants are monomer in solution, and further analyzed by SDS-PAGE to measure the purity of samples (**Figure 3.2B**).

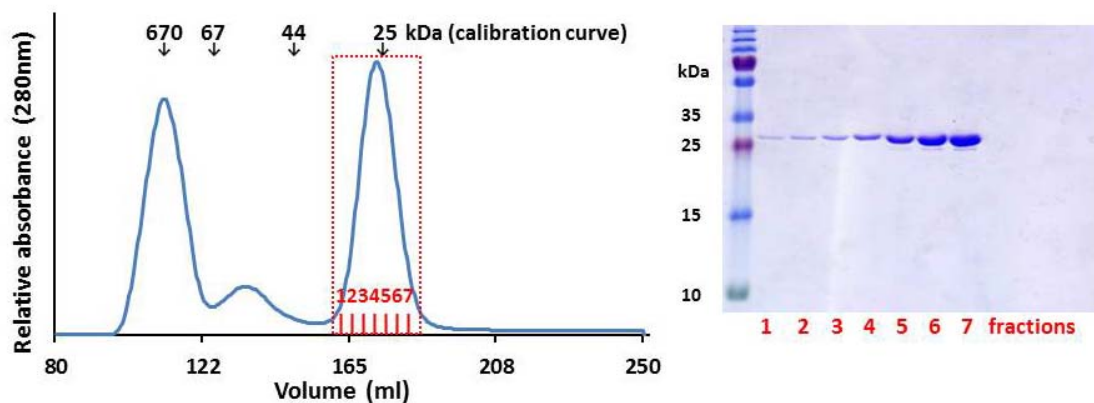


**Figure 3.2.** Purification of P1aABD **(A)** Elution profile of P1aABD using a Superdex 75 26/60 column. Aggregates were eluted at the void volume (109.7 ml) and P1aABD was eluted at the peak of 173 ml, corresponding to the molecular weight estimation of 28 kDa. **(B)** SDS-PAGE analysis of the fractions. The gel (15% of acrylamide) was stained with Coomassie brilliant blue.

### 3.1.3. Prediction of the disordered region of the N-terminal tail.

The isoform specific sequence of plectin 1a was aligned with other isoforms (1b, 1c, 1d, 1e, 1f, and 1g) to examine the sequence similarity among isoforms (**Figure 3.3**). The alignment shows no sequence conservation among seven plectin isoforms. These sequences were also analyzed by PrDOS (Ishida & Kinoshita, 2007) to predict the disordered region (**Figure 3.3**). It was predicted that plectin isoform 1a mostly contains the disordered part from the N-terminus (81.1 %) like isoform 1c (85.1 %). Other isoforms contain the following portions of residues predicted to be intrinsically disordered: 1b (43.2 %), 1d (100 %), 1e (66.7%), 1f (60.7 %), and 1g (27.3%).



**Figure 3.3.** Sequence alignment of plectin isoform sequences. The N-terminal specific sequences of seven isoforms were aligned, showing no sequence similarity among isoforms; conserved residues are shaded in green and identical residues are lightened in yellow. In addition, disordered residues predicted by PrDOS (Ishida & Kinoshita, 2007) are shown in red. The UniProt accession numbers of plectin isoform specific sequences are the following: 1a (Q9QXS1-3), 1b (Q9QXS1-5), 1c (Q9QXS1-6), 1d (Q9QXS1-10), 1e (Q9QXS1-12), 1f (Q9QXS1-13), and 1g (Q9QXS1-14).

### 3.1.4. Mapping of calmodulin interaction site on plectin 1a

Calmodulin interacts with plectin in an isoform-specific manner, namely only plectin 1aABD, but not 1cABD, or 1fABD showed binding to calmodulin-Sepharose beads (Kostan et al, 2009). In the same study the calmodulin interaction site was mapped to CH1 domain of plectin ABD. To further dissect and characterize the interaction site between P1a and calmodulin and to examine the role of the N-terminal sequence specific segment of P1a isoform in this interaction, I prepared several N-terminal truncation mutants of P1aABD and subjected them together with the full-length P1aABD to the pull-down assays with calmodulin-Sepharose beads in the presence of either  $\text{Ca}^{2+}$  or EDTA. While P1aABD, P1aABD $_{\Delta 11}$ , and P1aABD $_{\Delta 22}$  showed binding to full-length calmodulin in a calcium-dependent manner (**Figure 3.4**), this was not the case for P1aABD $_{\Delta 32}$  missing 32 residues

from the N-terminus, and for P1aABD $_{\Delta 37}$  missing the entire N-terminal extension. Thus the binding of calmodulin to P1a seems to be restricted to the region spanning 10 amino acids (residues 23-32) in the N-terminal tail, supporting the previous observation that the binding of calmodulin to plectin is isoform specific, as corroborated by sequence comparison that shows no sequence homology between plectin isoform specific sequences (**Figure 3.3**).

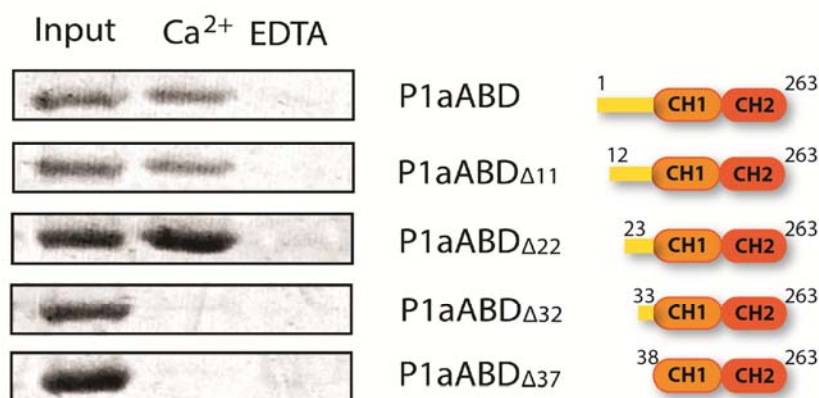


**Figure 3.4.** Pull-down assay. CaM-Sepharose beads were incubated with plectin variants in the presence of either Ca<sup>2+</sup> or EDTA, showing that ten amino acid residues (residues 23-32) are essential for the binding.

### 3.1.5. Crystallization and structure determination of P1aABD $_{\Delta 22}$

P1aABD $_{\Delta 22}$  (23-263) was crystallized by a vapor diffusion method (sitting-drop) at 22 °C. The protein sample was mixed with an equal volume of the crystallization solution containing 0.05 M potassium phosphate monobasic and 20% PEG 8000. Crystals were transferred to crystallization solution containing 20% glycerol and flash frozen in liquid nitrogen. Diffraction data were collected using the beamline ID14-4 at ESRF (Grenoble, France). The structure was solved by molecular replacement; plectin ABD (PDB: 1MB8) (Garcia-Alvarez et al, 2003) was used as a search model.



### 3.1.6. The crystal structure of P1aABD<sub>Δ22</sub>

I determined the crystal structure of P1aABD<sub>Δ22</sub> to 2.3 Å resolution in order to analyze the conformational change dependent upon the binding of calmodulin (**Figure 3.5**). P1aABD<sub>Δ22</sub> was crystallized in the space group of C222<sub>1</sub> and an asymmetric unit contains two P1aABD<sub>Δ22</sub> molecules. The structure was refined to R<sub>work</sub> and R<sub>free</sub> factors of 0.191 and 0.244, respectively. The data collection and refinement statistics are summarized in **Table 1**.

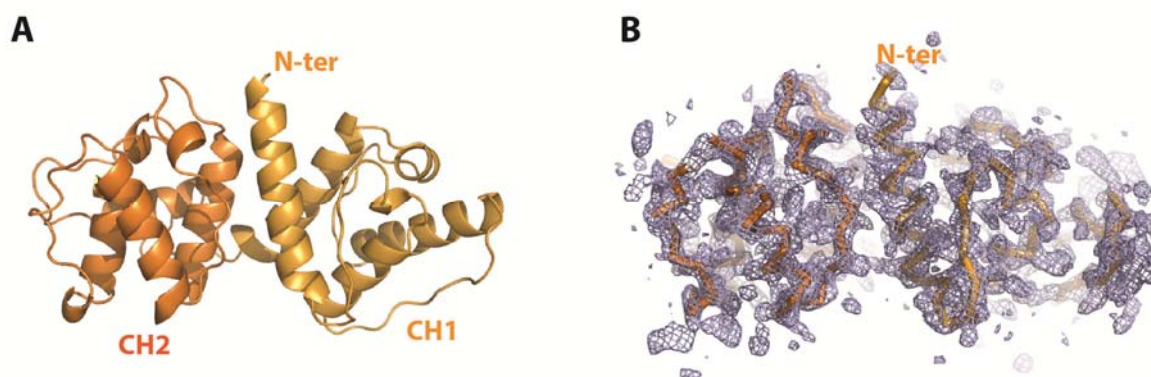


**Figure 3.5. (A)** The crystal structure of P1aABD<sub>Δ22</sub> is displayed in orange; calponin homology domains 1 and 2 (CH1 and CH2) are respectively consisted of four major helices and shown in bright and dark orange. **(B)** The electron density corresponding to 15 residues of N-terminal tail (amino acid residues 23-37) is absent in the structure. The electron density map (2Fo-Fc) is contoured at 1.5  $\sigma$ .

**Table 1.** Data collection and refinement statistics P1aABD<sub>Δ22</sub>

DATA COLLECTION		REFINEMENT	
Source	ID14-4 (ESRF)	R <sub>work</sub> <sup>d</sup>	0.194
Wavelength (Å)	0.939	R <sub>free</sub> <sup>e</sup>	0.244
Resolution (Å)	60.37-2.30 (2.38-2.30) <sup>a</sup>	R.m.s.d. bonds (Å)	0.010
Space group	C222 <sub>1</sub>	R.m.s.d. angles (°)	1.236
Unit cell (Å, °)	a = 41.60, b = 159.39, c = 183.83, α = β = γ = 90	Wilson B factor	34.65
Molecules / a.u.	2	MOLPROBITY <sup>f</sup> STATISTICS	
Unique reflections	28020 (2698)	All-atom clash score	6.04
Completeness (%)	99.7 (99.8)	Ramachandran plot	
R <sub>merge</sub> <sup>b</sup>	0.125 (0.424)	Outliers	0.00 %
R <sub>meas</sub>	0.143 (0.483)	Allowed	1.34 %
R <sub>pim</sub> <sup>c</sup>	0.067 (0.224)	Favored	98.66 %
Multiplicity	4.4 (4.2)	Rotamer outliers	0.72 %
Mean I/sig(I)	6.9 (2.2)	C-beta deviations	0
CC (1/2)	0.945 (0.856)		

<sup>a</sup>Values in parentheses are for the highest resolution shell.

$${}^b R_{merge} = \frac{\sum_{hkl} \sum_j |I_{hkl,j} - \langle I_{hkl} \rangle|}{\sum_{hkl} \sum_j I_{hkl,j}} \quad {}^c R_{pim} = \frac{\sum_{hkl} \sqrt{\frac{1}{n-1}} \sum_{j=1}^n |I_{hkl,j} - \langle I_{hkl} \rangle|}{\sum_{hkl} \sum_j I_{hkl,j}}$$

<sup>d</sup>R<sub>work</sub> = Σ|Fo-Fc| / ΣFo, <sup>e</sup>R<sub>free</sub> is the cross-validation. <sup>d</sup>R<sub>work</sub> computed for the test set of reflections (5 %) which are omitted in the refinement process.

<sup>f</sup> (Chen et al, 2010)

The actin-binding domain of plectin 1a is consisted of two calponin homology domains (CH1 and CH2) (**Figure 3.5A**). The most notable feature is that the electron density corresponding to 15 residues of the N-terminal tail is absent from the crystal structure (**Figure 3.5B**). The missing residues in the crystal structure are essential for the CaM binding (**Figure 3.4**); however the crystal structure shows that the N-terminal tail is disordered as predicted above (**Figure 3.3**). The difference between isoform 1a and 1c is that isoform 1c possesses an ordered helix in the isoform specific sequence (6 residues)(Garcia-Alvarez et al, 2003) extended from the A-helix of CH1 domain; whereas the isoform specific sequence of 1a is totally disordered.

### 3.1.7. The solution structure of P1aABD

P1aABD was prepared as described in a section **3.1.2**. The SAXS analysis of P1aABD alone was carried out to model the N-terminal segment, which is not visible in the crystal structure of P1aABD<sub>Δ22</sub>. Three concentrations of P1aABD samples (3.0, 4.5, and 6.0 mg/ml) were measured and merged for the further analyses since the concentration dependence was not detected by comparing  $I(0)$  and  $R_g$ . Three concentrations of P1aABD samples (3.0, 4.5, and 6.0 mg/ml) were measured and merged for the further analyses since the concentration dependence was not detected by comparing  $I(0)$  and  $R_g$ . Data collection and structural parameters derived from SAXS analyses on P1aABD are summarized in **Table 2**. The N-terminal extension was modeled as an ensemble of structurally variable moieties by the program EOM while the crystal structure of plectin ABD (**Figure 3.5**) was used as a rigid body for model generation, which fits to the experimental data with the  $\chi$  value of 1.09 (**Figure 3.6A**). EOM analysis shows a broad  $R_g$  distribution against the frequency of occurrence, indicating high flexibility of the N-terminal tail (**Figure 3.6B**). Eight models from the selected ensemble (in total 50 models) were superimposed to ABD, showing the random conformations of the N-terminal tail of plectin isoform 1a (**Figure**

**3.6C).** All together, these data confirm the disordered nature of the P1a isoform specific sequence.

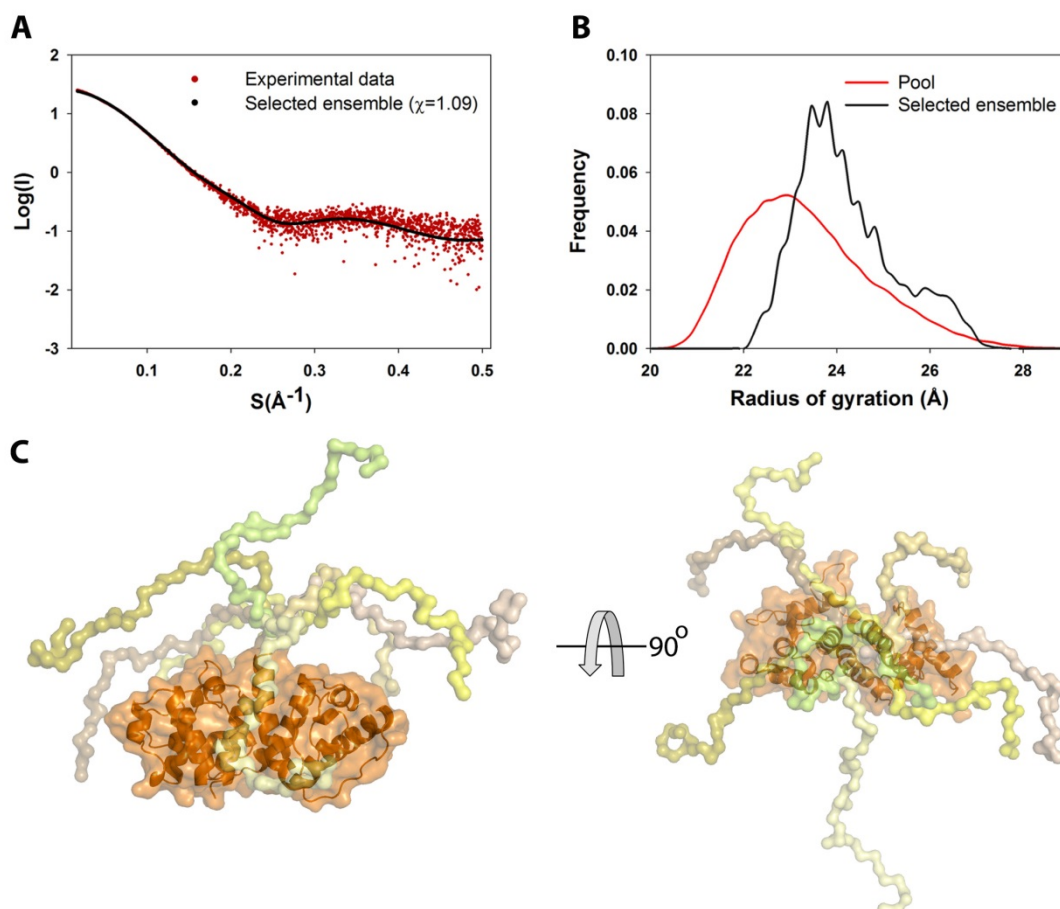


**Figure 3.6.** EOM analyses on the N-terminal tail of P1a. **(A)** The experimental scattering curve of P1aABD is shown in red; the simulated scattering curve of the selected ensemble by EOM is displayed in black **(B)** The frequency distributions of  $R_g$  generated from EOM are compared between the pool (red curve) and the selected ensemble (black curve). **(C)** Eight models from the selected ensemble are superimposed, showing the random conformations of the N-terminal tail in different orientations.

**Table 2.** Data collection and scattering-derived parameters of P1aABD

Data collection parameters		Structural parameters	
Instrument	SAXS beamline X33 (DESY)	$I(0)$ [from $P(r)$ ]	$26.05 \pm 0.01^*$
Sample to detector distance (m)	SAXS beamline X33 (DESY)	$R_g$ (nm) [from $P(r)$ ]	$2.51 \pm 0.01$
Wavelength (Å)	2.7 m	$I(0)$ (from Guinier)	$26.29 \pm 0.04$
$S$ range (Å <sup>-1</sup> )	1.5	$R_g$ (nm) (from Guinier)	$2.52 \pm 0.01$
Exposure time (sec)	0.08-0.6	Porod volume (nm <sup>3</sup> )	58.34
Temperature (K)	15	Dmax (nm)	8.7

\*Data are expressed as mean value  $\pm$  standard deviation.

## 3.2. Studies on the plectin 1a actin-binding domain/calmodulin complex

### 3.2.1. Construct design

The plectin construct (P1aABD) was used for the interaction study with calmodulin. Full-length calmodulin (CaM, 148 residues) and each lobe of CaM were prepared (**Figure 3.7**).



**Figure 3.7.** Schematic drawings of P1aABD and calmodulin constructs. The entire calmodulin (CaM, 1-148) construct as well as its N-terminal and C-terminal lobes (termed CaM<sub>NL</sub>(6-73) and CaM<sub>CL</sub>(82-148), respectively) were prepared.

### 3.2.2. Purification of calmodulin constructs

Expressed calmodulin constructs were finally purified using Superdex 75 gel filtration columns (GE Healthcare). Calmodulin (CaM) was eluted at the peak of 71 ml from a Superdex 75 16/60 column (GE Healthcare), corresponding to the molecular weight estimation of 40 kDa, indicating that CaM has an elongated shape in solution (**Figure 3.8A**). CaM<sub>NL</sub> was eluted at the peak of 198 ml from a Superdex 75 26/60 column (GE Healthcare), corresponding to the molecular weight estimation of 14 kDa, while CaM<sub>CL</sub> was eluted at the peak of 212 ml, corresponding to the molecular weight estimation of 10 kDa. Both lobes exhibit several bands in SDS-PAGE gels, indicating that each lobe possesses multiple conformations even in the denatured condition (**Figure 3.8B and 3.8C**).

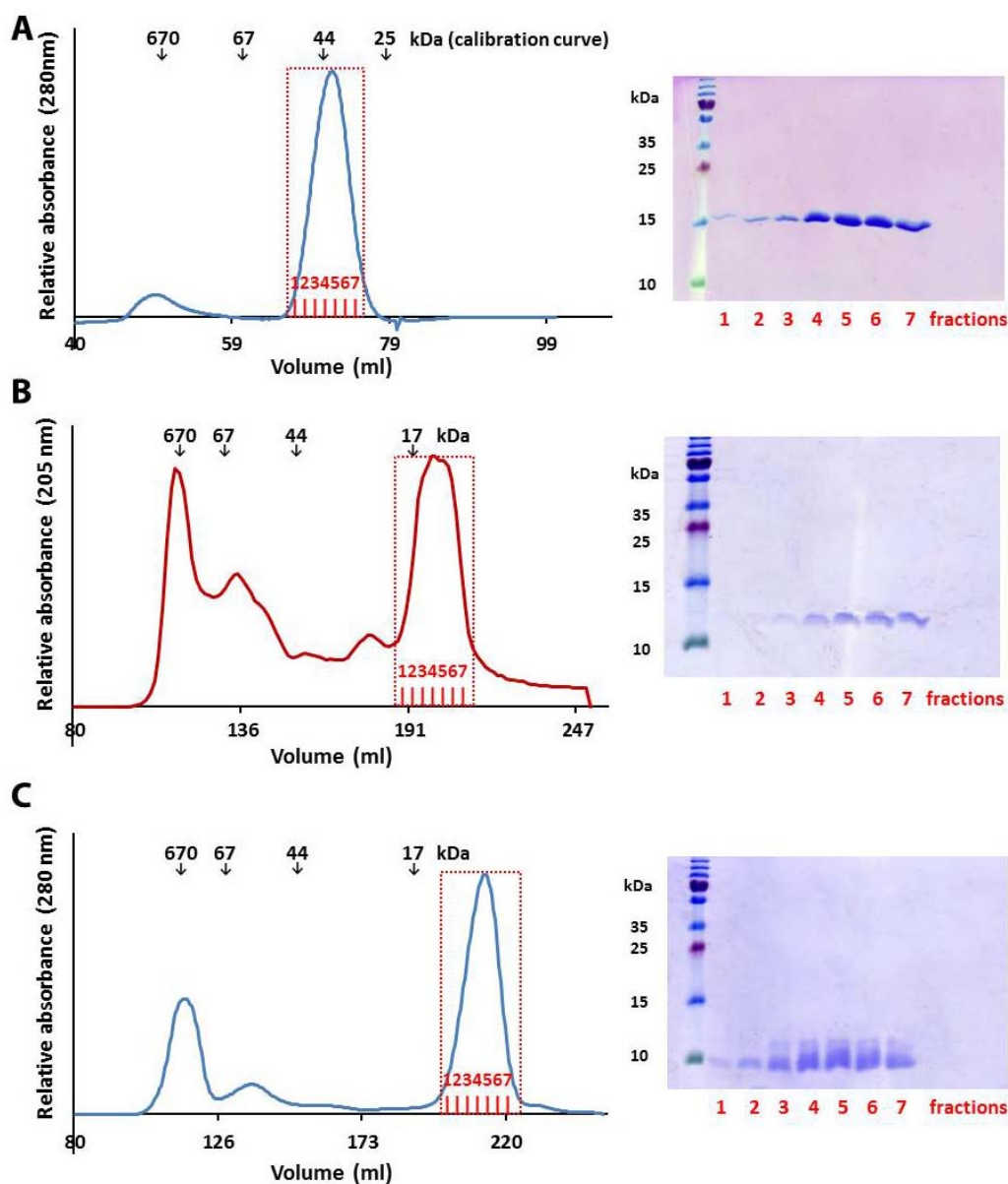


**Figure 3.8.** Purification of calmodulin constructs. **(A)** Elution profile of CaM using a Superdex 75 16/60 column. CaM was eluted at the peak of 71 ml, corresponding to the molecular weight estimation of 40 kDa. **(B)** Elution profile of CaM<sub>NL</sub> using a Superdex 75 26/60 column. CaM was eluted at the peak of 198 ml, corresponding to the molecular weight estimation of 14 kDa. Due to the absence of aromatic residues, UV 205 nm was used to detect CaM<sub>NL</sub>. **(C)** Elution profile of CaM<sub>CL</sub> using a Superdex 75 26/60 column. CaM was eluted at the peak of 212 ml, corresponding to the molecular weight estimation of 10 kDa.

### 3.2.3. Thermal shift assay (Thermofluor)

Thermofluor was carried out to understand the thermal stability of the complex and individual components and to find out the optimal crystallization solution for the P1aABD/CaM complex (Ericsson et al, 2006). The thermofluor profile of CaM is not interpretable; it has a highest fluorescence signal at the very beginning (at 20 °C) and the fluorescence level decreases afterwards (**Figure 3.9**). It is suggested that the hydrophobic dye (Sypro Orange, Molecular Probes) binds to the hydrophobic core of CaM in the presence of calcium and emits the signal from the initial temperature. P1aABD shows a typical thermofluor curve, showing the melting temperature of 60 °C. The P1aABD/CaM displays the melting temperature of 54 °C; whereas it exhibits an approximately half signal of the CaM at the beginning. The results suggest that one of calmodulin lobes might bind to P1aABD, showing the half fluorescence signal of CaM at the beginning.

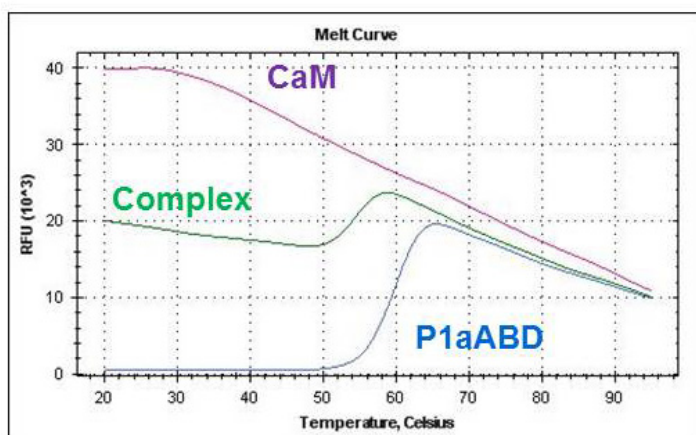


**Figure 3.9.** Thermal shift assay. The thermofluor profiles of P1aABD, CaM, and the P1aABD/CaM complex are individually shown in blue, purple, and green curves.

### 3.2.4. Cross-linking and Mass Spectrometry analyses

The cross-linking assay combined with mass spectrometry analyses was performed to understand the binding interface of the P1aABD/CaM complex in order to verify the



thermofluor results that suggest only one lobe of CaM is involved in the interaction (**Figure 3.9**). Cross-linking was tried using EDC/sulfo-NHS as a zero-length cross-linker in the presence of either calcium or EDTA with one or two-step methods. The results show that EDC/sulfo-NHS cross-links CaM and P1aABD in a calcium dependent manner and two-step cross-linking is more specific than one-step (**Figure 3.10A and B**). In addition to bands of monomeric P1aABD and CaM, protein bands corresponding to approximately 40 kDa specifically appear upon one- or two-step zero-length cross-linking, indicating the formation of a 1:1 complex. To identify intermolecular cross-links at a site-specific level, protein bands produced by two-step methods from a SDS-PAGE gel were in-gel digested using trypsin and further analysed by high resolution LC-MS/MS in the collaboration with Dr. Friedel Drepper and Prof. Bettina Warsheid in University of Freiburg, Germany.

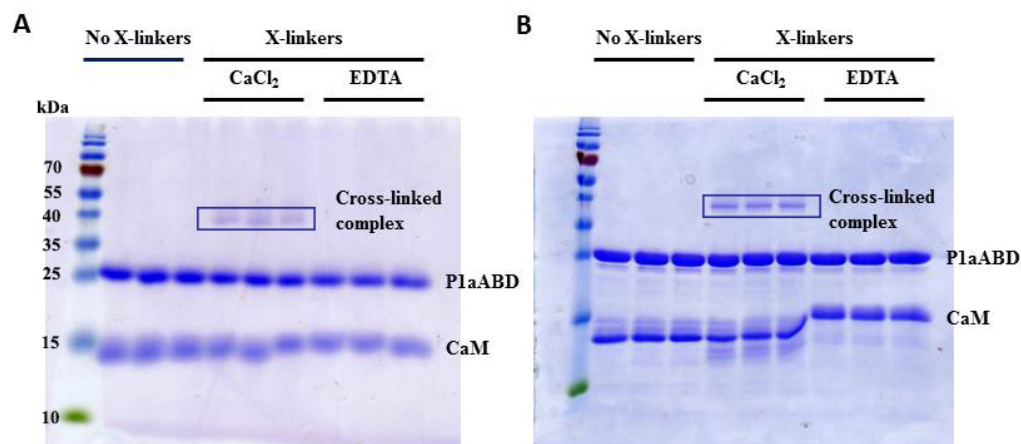


**Figure 3.10.** Cross-linking assays. The cross-linking assays using EDC/sulfo-NHS were carried out by one-step (**A**) and two step methods (**B**). Each experiment was performed with three batches in three different conditions: without cross-linkers (No X-linkers) and with cross-linkers (X-linkers) in the presence of either CaCl<sub>2</sub> or EDTA. The bands of the cross-linked complex are pointed out in the figure (Cross-linked complex).

**Table 3.** Mass spectrometry analysis of the cross-linked complex.

mass / Da	peptide of P1aABD		Peptide of CaM		P-value <sup>c</sup>	No. of spectra <sup>d</sup>	sum of Intensity
	sequence <sup>a</sup>	P-value <sup>b</sup>	sequence <sup>a</sup>	P-value <sup>b</sup>			
1955.9565	ASEGKKDE R	6.7E-03	EAFSLFDK	8.4E-14	4.7E-15	1	4.9E6
2372.1453	KDER	1.3E-03	EAFSLFDKDG ITTK	7.9E-11	8.4E-14	1	2.1E6
2643.2760	KDERDR	1.6E-03	EAFSLFDKDG ITTK	7.4E-08	5.2E-12	3	8.4E6
1555.7858	ASEGKK	1.9E-03	EAFSLFDK	1.9E-07	2.0E-11	1	3.0E6
2844.3763	ASEGKKDE R	2.8E-02	EAFSLFDKDG ITTK	4.0E-05	1.9E-07	1	6.1E7
1818.8752	EKGR	2.1E-02	LTDEEVDEMIR	3.2E-12	7.2E-14	1	2.3E6
1818.8766	EKGR	1.5E-02	LTDEEVDEMIR	1.0E-09	1.3E-11	1	1.8E6
2211.1308	HLIK <sup>a</sup> AQR	1.1E-04	LTDEEVDEM <sup>a</sup> IR	2.8E-05	2.9E-10	2	6.6E6
1320.6529	KDERDR	1.0E-03	EAFR	3.7E-02	2.5E-06	1	1.5E5
1049.5253	KDER	2.5E-02	EAFR	3.0E-03	2.4E-05	1	8.3E4
1521.7516	ASEGKKDE R	1.3E-04	EAFR	1.9E-02	5.8E-06	2	1.9E6
1513.7656	EKGR	2.1E-02	HVM <sup>a</sup> TNLGEK	3.5E-03	6.0E-05	2	1.1E6

<sup>a)</sup> E, K signify site of cross-linker, M<sup>\*</sup>, oxidized methionine

<sup>b)</sup> Subscores per peptide

<sup>c)</sup> P-value for cross-linked peptide

<sup>d)</sup> MS/MS spectra for ion species differing in charge or oxidation state; mass and P-values represent best match

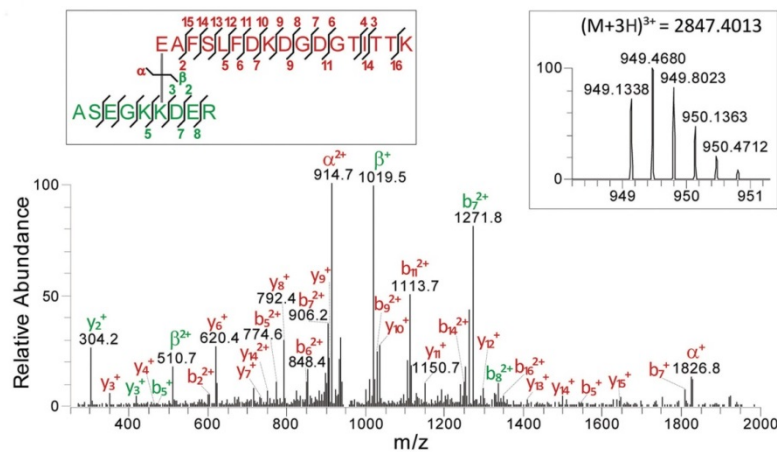


**Figure 3.11.** MS/MS-Spectrum identifying a pair of cross-linked peptides after in-gel proteolysis of the complex band marked in A obtained by two-step cross-linking of CaM and P1aABD. Fragment ions are annotated for the  $\alpha$ -peptide (red) and the  $\beta$ -peptide (green). Insets show mapping of the fragment ions onto the cross-linked peptide sequences (left) and the corresponding high-resolution MS1 spectrum displaying the isotopic distribution of the cross-linking product (right).

A representative MS/MS spectrum of a specific cross-linking product identifying a linkage between Glu14 of CaM and Lys37 of P1aABD is depicted in (**Figure 3.11**). In total, 12 cross-linked peptides were identified for the P1aABD/CaM complex obtained by EDC/sulfo-NHS treatment (**Table 3**). Most of the cross-linked sites were identified in more than one pair of peptides, increasing the confidence for these sites of interaction. The major cross-linking products identified involve the adjacent lysine residues 36 and 37 within the sequence specific N-terminal segment of P1aABD. Both residues located in the N-terminal tail were found to be cross-linked to Glu14 residing in the A-helix of CaM's EF-hand 1. Other identified cross-linking products involve several sites of the C-lobe of CaM, possibly indicating a less specific binding of the C-lobe to P1aABD. Thus, the crosslinking data suggest that both lobes of CaM have the capacity to interact with P1aABD; however,

cross-linked peptides connecting the N-lobe of CaM to the N-terminal tail of P1aABD were found to be more prominent and detected in higher abundance (**Table 3**).

### 3.2.5. N-lobe of CaM preferably binds to P1aABD

In order to further characterize the preferable binding of CaM<sub>NL</sub>, as suggested from the XL-MS analyses, I measured and compared the binding affinities of Ca<sup>2+</sup>/CaM, CaM<sub>NL</sub> and CaM<sub>CL</sub> lobes to P1aABD by ITC. The ITC results revealed that CaM<sub>NL</sub> binds to P1aABD with higher affinity ( $K_d$  of 10.5  $\mu$ M) than CaM<sub>CL</sub> ( $K_d$  of 27.7  $\mu$ M) (**Figure 3.12A and B**).

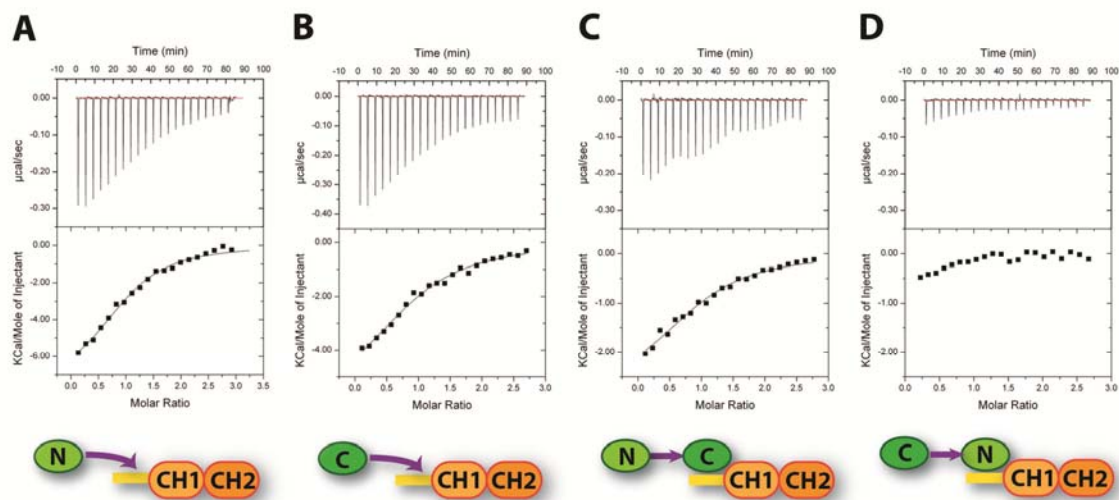


**Figure 3.12.** ITC analyses **(A)** 400  $\mu$ M CaM<sub>NL</sub> was titrated to 40  $\mu$ M P1aABD **(B)** 400  $\mu$ M CaM<sub>CL</sub> was titrated to 40  $\mu$ M P1aABD **(C)** 400  $\mu$ M CaM<sub>NL</sub> was titrated to 40  $\mu$ M P1aABD/60  $\mu$ M CaM<sub>CL</sub>. **(D)** 400  $\mu$ M CaM<sub>CL</sub> was titrated to 40  $\mu$ M P1aABD/60  $\mu$ M CaM<sub>NL</sub>. All ITC measurements were carried out at 25 °C of isotherm.

Both reactions are enthalpy-driven, however, the CaM<sub>NL</sub> binding is enthalpically more favored, leading to the higher affinity (**Table 4**). In addition, CaM<sub>NL</sub> was found to displace CaM<sub>CL</sub> when titrated to the P1aABD/CaM<sub>CL</sub> complex. In detail, the competitive binding reduces the apparent binding affinity (**Figure 3.12C**), resulting in decreased enthalpy contribution owing to the dissociation of CaM<sub>CL</sub> (**Table 4**). In contrast to CaM<sub>NL</sub>, CaM<sub>CL</sub> could not displace CaM<sub>NL</sub> from P1aABD/CaM<sub>NL</sub> complex (**Figure 3.12D**). These results indicate that the CaM<sub>NL</sub> binds to the same binding site of P1aABD with higher affinity than CaM<sub>CL</sub>. When CaM was titrated to P1aABD, the affinity ( $K_d$  of 4.2  $\mu$ M) was higher than CaM<sub>NL</sub> alone (**Figure 3.29B**), suggesting an auxiliary role of CaM<sub>CL</sub> for the binding event. In summary, XL-MS data combined with comprehensive binding study by ITC conclusively show that CaM binds to P1a preferentially via its N-terminal lobe.

**Table 4.** Summary of ITC results

Syringe	Cell	N	Kd ( $\mu$ M)	$\Delta H$ (kcal/mol)	$\Delta S$ (cal/mol/deg)
CaM <sub>NL</sub>	P1aABD	1.01	10.5 $\pm$ 1.1	-9.81 $\pm$ 0.64	-9.57
CaM <sub>CL</sub>	P1aABD	0.95	27.7 $\pm$ 3.9	-7.42 $\pm$ 0.89	-3.65
CaM <sub>NL</sub>	P1aABD/ CaM <sub>CL</sub>	0.97	18.7 $\pm$ 2.8	-2.61 $\pm$ 0.26	13.00
CaM <sub>CL</sub>	P1aABD/ CaM <sub>NL</sub>	ND	ND	ND	ND

\* Data are expressed as mean value  $\pm$  standard deviation. ND means ‘not determined’.

### 3.2.6. Crystallization and structure determination of the P1aABD <sub>$\Delta$ 22</sub>/CaM<sub>NL</sub> complex

To get insight into molecular mechanism of P1a interaction with calmodulin, I carried out structural studies on the P1aABD/CaM complex. Based on the results of the pull-down assay and predictions of intrinsically disordered regions, it was considered that the P1aABD <sub>$\Delta$ 22</sub> construct (residues 23-263) to be the most suitable for further crystallization

studies. Even though extensive crystallization trials with P1aABD $_{\Delta 22}$ /full-length calmodulin complex, I did not obtain any crystals. Since N-lobe of calmodulin preferentially binds to a short region of the N-terminal extension of P1a, N-lobe of CaM (CaM $_{NL}$ ) was used for crystallization studies instead of full-length calmodulin. P1aABD $_{\Delta 22}$  (23-262) was mixed with CaM $_{NL}$  in an equal molar ratio and the protein complex was purified from a gel filtration column in the presence of calcium (**Figure 3.13**). Crystals of the complex were grown by the hanging-drop vapor diffusion method at 4 °C. The concentrated protein solution (11 mg/ml) was mixed with an equal volume of the crystallization solution containing 0.1 M Bis-Tris pH 6.5, 0.2 M MgCl $_2$ , and 13% PEG 8000. Crystals were transferred to cryo-protectant containing 20% glycerol and flash frozen in liquid nitrogen. Diffraction data were collected at the beamline ID14-1 in ESRF (Grenoble, France). The structure was solved by molecular replacement using plectin ABD (PDB: 1MB8) as a search model.

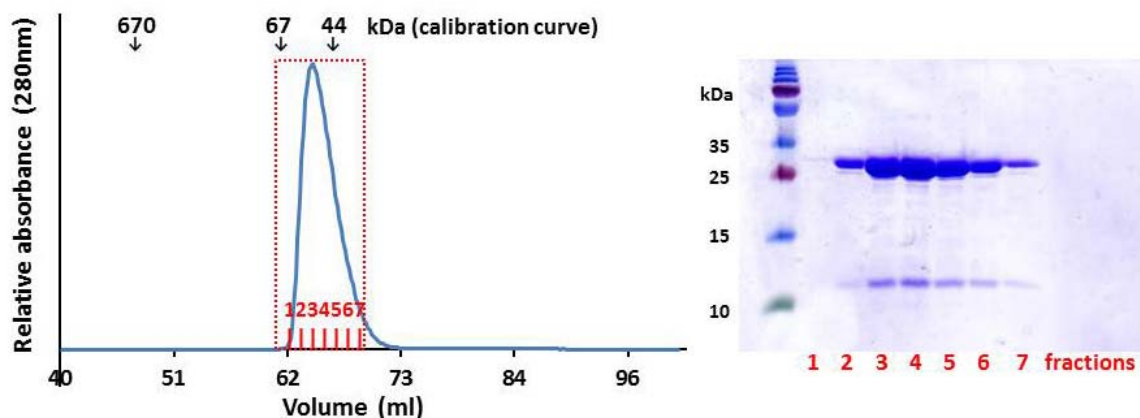


**Figure 3.13.** Purification of the P1aABD $_{\Delta 22}$ /CaM $_{NL}$  complex. **(A)** Elution profile of the P1aABD $_{\Delta 22}$ /CaM $_{NL}$  complex using a Superdex 75 16/60 column. The P1aABD $_{\Delta 22}$ /CaM $_{NL}$  complex was eluted at the peak of 65 ml, corresponding to the molecular weight estimation of 51 kDa. **(B)** SDS-PAGE analysis of the fractions. The gel (15% of acrylamide) was stained with Coomassie brilliant blue.

### 3.2.7. Crystal structure of the P1aABD<sub>Δ22</sub>/CaM<sub>NL</sub> complex

I determined the structure to 1.8 Å resolution with final R<sub>work</sub> and R<sub>free</sub> factors of 0.149 and 0.188, respectively. Data collection and refinement statistics are summarized in **Table 5**.

**Table 5.** Data collection and refinement statistics P1aABD<sub>Δ22</sub>/CaM<sub>NL</sub>

DATA COLLECTION		REFINEMENT	
Source	ID14-1 (ESRF)	R <sub>work</sub> <sup>d</sup>	0.149
Wavelength (Å)	0.933	R <sub>free</sub> <sup>e</sup>	0.188
Resolution (Å)	48.93-1.8 (1.9-1.8) <sup>a</sup>	R.m.s.d. bonds (Å)	0.007
Space group	P2 <sub>1</sub> 2 <sub>1</sub> 2 <sub>1</sub>	R.m.s.d. angles (°)	0.974
Unit cell (Å, °)	a= 59.08, b= 65.38, c= 87.3 α= β= γ= 90	Wilson B factor	17.05
Molecules / a.u.	2	MOLPROBITY <sup>f</sup> STATISTICS	
Unique reflections	31805 (4301)	All-atom clash score	2.15
Completeness (%)	99.2 (94.7)	Ramachandran plot	
R <sub>merge</sub> <sup>b</sup>	0.095 (0.488)	Outliers	0.00 %
R <sub>meas</sub>	0.101 (0.527)	Allowed	0.96 %
R <sub>pim</sub> <sup>c</sup>	0.033 (0.193)	Favored	99.04 %
Multiplicity	9.4 (7.2)	Rotamer outliers	0.70 %
Mean I/sig(I)	17.5 (3.7)	C-beta deviations	0
CC (1/2)	0.998 (0.877)		

<sup>a</sup>Values in parentheses are for the highest resolution shell.

$$^b R_{merge} = \frac{\sum_{hkl} \sum_j |I_{hkl,j} - \langle I_{hkl} \rangle|}{\sum_{hkl} \sum_j I_{hkl,j}} \quad ^c R_{pim} = \frac{\sum_{hkl} \sqrt{\frac{1}{n-1}} \sum_{j=1}^n |I_{hkl,j} - \langle I_{hkl} \rangle|}{\sum_{hkl} \sum_j I_{hkl,j}}$$

<sup>d</sup>R<sub>work</sub> =  $\Sigma |F_o - F_c| / \Sigma F_o$ , <sup>e</sup>R<sub>free</sub> is the cross-validation. <sup>d</sup>R<sub>work</sub> computed for the test set of reflections (5 %) which are omitted in the refinement process. <sup>f</sup> (Chen et al, 2010)

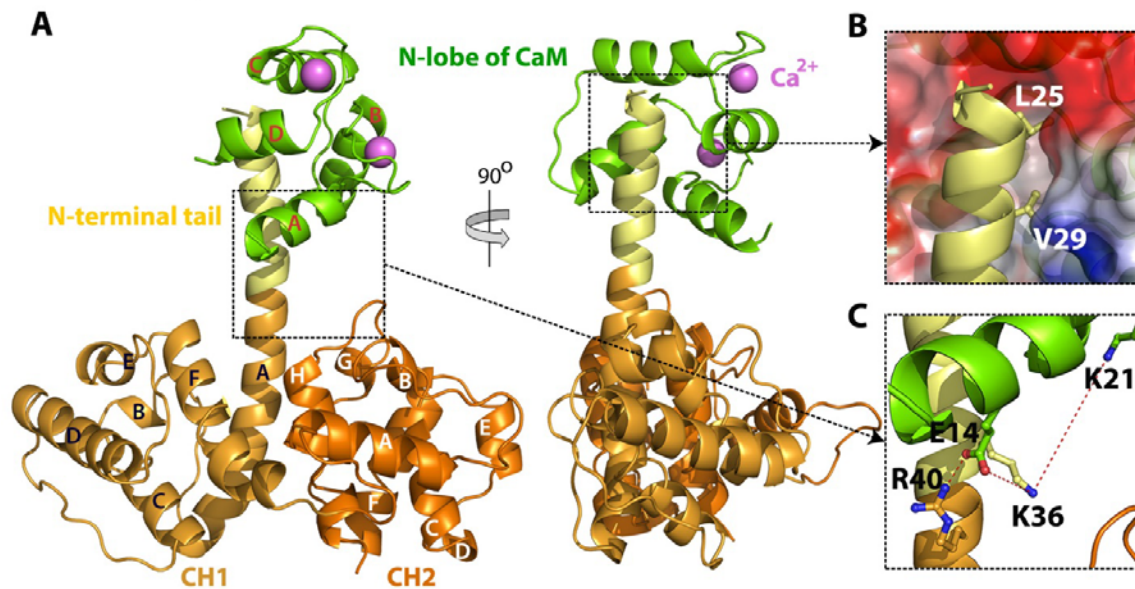


**Figure 3.14.** Crystal structure of the P1aABD $\Delta$ 22/CaM<sub>NL</sub> complex. **(A)** Crystal structure of the P1aABD $\Delta$ 22/CaM<sub>NL</sub> complex is displayed; CH1 and CH2 in ABD are separately displayed in bright-orange and orange, the N-terminal tail in yellow, and CaM<sub>NL</sub> in green. Ca<sup>2+</sup> is presented as a violet sphere **(B)** The binding interface of P1aABD $\Delta$ 22/CaM<sub>NL</sub> complex; CaM<sub>NL</sub> is shown in the electrostatic potential surface and two residues (L25 and V29) of plectin are varied into CaM<sub>NL</sub> **(C)** A salt bridge is established between CaM Glu14 and plectin Arg40 (2.7 Å apart). CaM Glu14 is involved in the cross-linking with plectin Lys36 (5.7 Å apart) and plectin Lys37 (7.0 Å) by EDC/sNHS.

As expected, CaM<sub>NL</sub> was found to bind to the N-terminal tail, which adopts an  $\alpha$ -helical structure, extending from the A-helix of CH1 domain, and protruding away from the body of the ABD (**Figure 3.14A**). Each EF hand of CaM<sub>NL</sub> coordinates one calcium ion, and binds to the N-terminal extension of P1a mainly *via* hydrophobic interactions (Crivici & Ikura, 1995) (**Figure 3.15**). CaM<sub>NL</sub> does not change the conformation upon binding to plectin, as



compared with the crystal structure of unbound  $\text{Ca}^{2+}$ /CaM (PDB: 3CLN) (root-mean-square deviation, RMSD: 0.40 Å over 62 equivalent C $\alpha$  atoms in N-lobe).

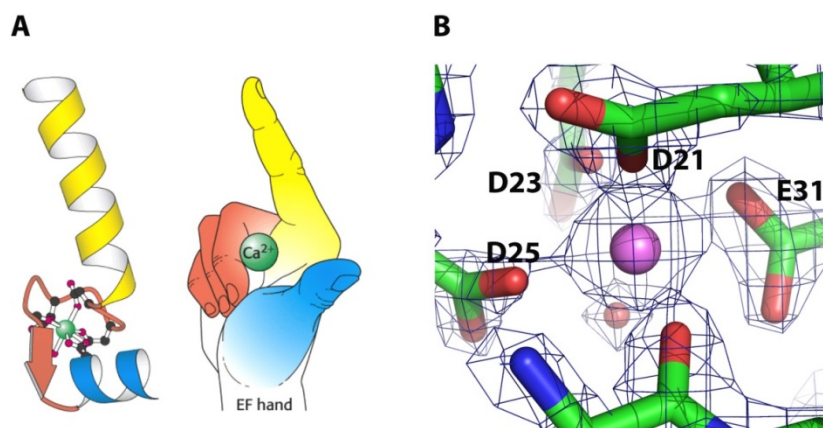


**Figure 3.15.** Calcium coordination of the EF hand motif. **(A)** Schematic drawing of EF hand **(B)** The first EF hand motif is shown in green stick. The pentagonal bi-pyramidal coordination of calcium is completed by 4 acidic residues (Asp21, Asp23, Asp25, and Glu31), one carbonyl group of the protein backbone, and one water molecule. The electron density map (2Fo-Fc) is contoured at 1.5  $\sigma$ .

Three hydrophobic residues of the N-terminal the  $\alpha$ -helical extension (Leu25, Val29, and Ala32) are buried into the hydrophobic cleft of  $\text{CaM}_{\text{NL}}$  (**Figure 3.14B**), which is consistent with known binding motif of  $\text{Ca}^{2+}$ /CaM termed 1-5-8 (Elshorst et al, 1999; Rhoads & Friedberg, 1997). The interacting residues were analyzed by Ligplot (Wallace et al, 1995). Leu25 forms stabilizing hydrophobic interactions with  $\text{CaM}_{\text{NL}}$  residues Leu32, Val55, Met51 and Met71, while Val29 interacts with residues Phe19, Phe68, and Met72 of  $\text{CaM}_{\text{NL}}$ . Ala32 is responsible for the interaction with Leu18 and Leu39 (**Figure 3.16**).

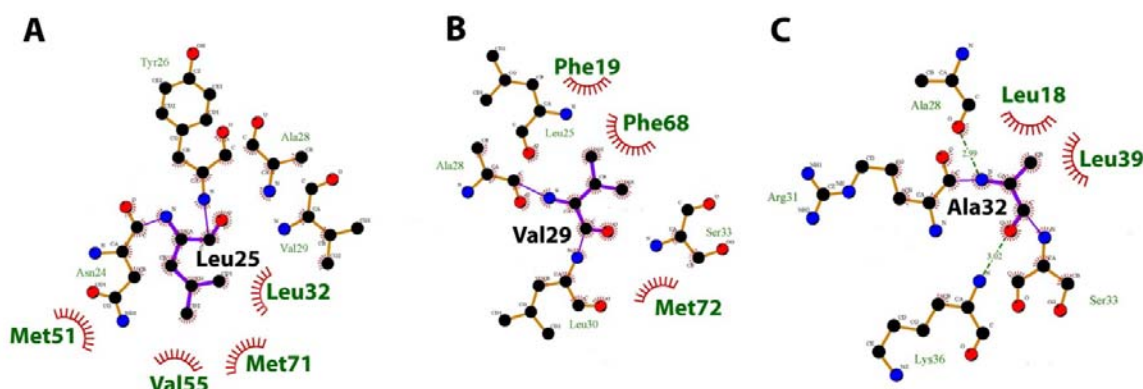


**Figure 3.16.** Ligplot analysis on hydrophobic residues (1-5-8 positions) in the N-terminal tail of plectin 1a. The interfacing hydrophobic residues in N-CaM are shown in green. **(A)** Leu25 forms stabilizing hydrophobic interactions with CaM residues Leu32, Val55, Met51 and Met71. **(B)** Val29 interacts with residues Phe19, Phe68, and Met72 of CaM<sub>NL</sub>. **(C)** Ala32 is involved in the interaction with Leu18 and Leu39 of CaM<sub>NL</sub>.

To validate the role of these residues in binding to  $\text{Ca}^{2+}$ /CaM, the double mutant of P1aABD (Leu25Asp and Val29Asp) was generated. By using of both, ITC and size exclusion chromatography, I showed that P1aABD double mutant does not interact with  $\text{Ca}^{2+}$ /CaM, confirming that Leu25 and Val29 residues play an essential role in the binding (**Figure 3.17**). In addition, a polar interaction between Gln41 (residing in the loop between B and C helix of N-lobe) and Arg31 of P1a (located in the N-terminal tail) and a salt bridge between Glu14 in A-helix of EF1 and Arg40 in A-helix of the CH1 domain of plectin are formed (**Figure 3.14C**). The salt bridge does not seem to be essential for the CaM binding as other isoforms of plectin also possess arginine residue at this position in CH1, but do not bind to  $\text{Ca}^{2+}$ /CaM, however, it is most likely involved in further stabilization of the overall interaction. In addition, the crystal structure of the P1aABD<sub>Δ22</sub>/CaM<sub>NL</sub> complex shows that the carboxylate group of Glu14 in CaM<sub>NL</sub> is 5.7 Å and 7.0 Å apart from the amino group of plectin Lys36 and Lys37 residues, respectively, which is in good agreement with the results obtained by XL-MS analysis (**Figure 3.14C**) (**Table 3**).

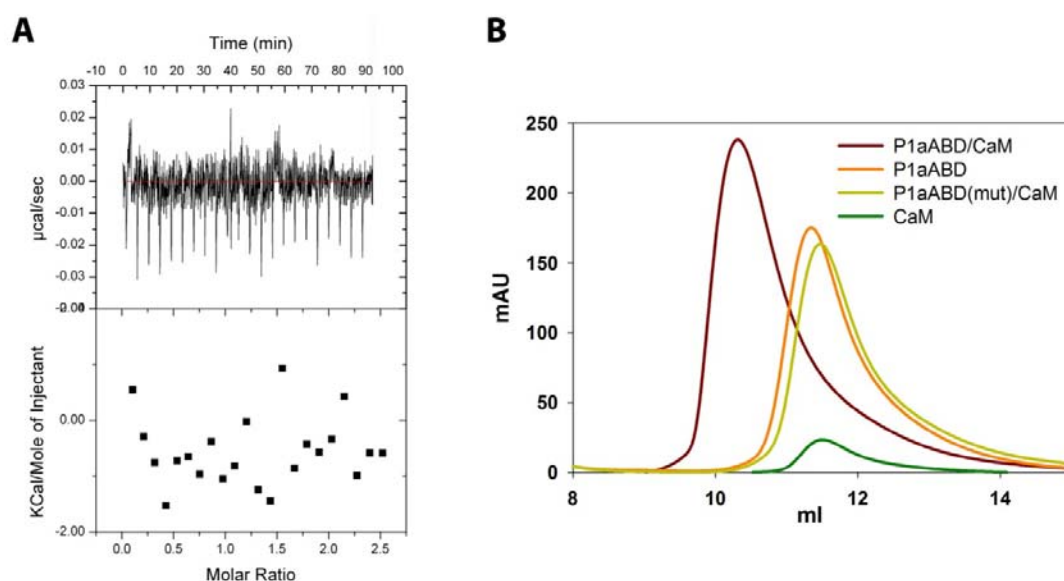


**Figure 3.17.** *In vitro* mutational analyses. **(A)** ITC experiment was carried out to measure the mutational effect on the interaction. CaM is titrated to the P1aABD mutant (Leu25Asp and Val29Asp); no interaction is observed. **(B)** Gel-filtration analyses. When P1aABD is mixed with CaM, it is eluted earlier than CaM and P1aABD, suggesting the complex formation in solution. However the P1aABD mutant/CaM mixture is identically eluted as P1aABD, showing no binding to CaM.

The most notable feature of the crystal structure of P1aABD $_{\Delta 22}$ /CaM $_{NL}$  complex is an  $\alpha$ -helix formed by the N-terminal tail (residues 23-37) (**Figure 3.14A**). It was proved that the N-terminal tail is disordered, shown by the crystal structure of P1aABD $_{\Delta 22}$  and EOM analysis of P1aABD.

On the other hand, the structure of the plectin ABD in complex with CaM $_{NL}$  is almost identical to that of the plectin ABD alone (RMSD: 0.69 Å over 209 equivalent C $\alpha$  atoms) indicating that plectin ABD does not undergo a conformational change upon Ca $^{2+}$ /CaM binding (**Figure 3.18**). Taken together these data show that the N-terminal tail is intrinsically disordered in unbound state and adopts an  $\alpha$ -helical conformation upon binding to CaM through “coupled folding and binding” mechanism (Dyson & Wright, 2005).

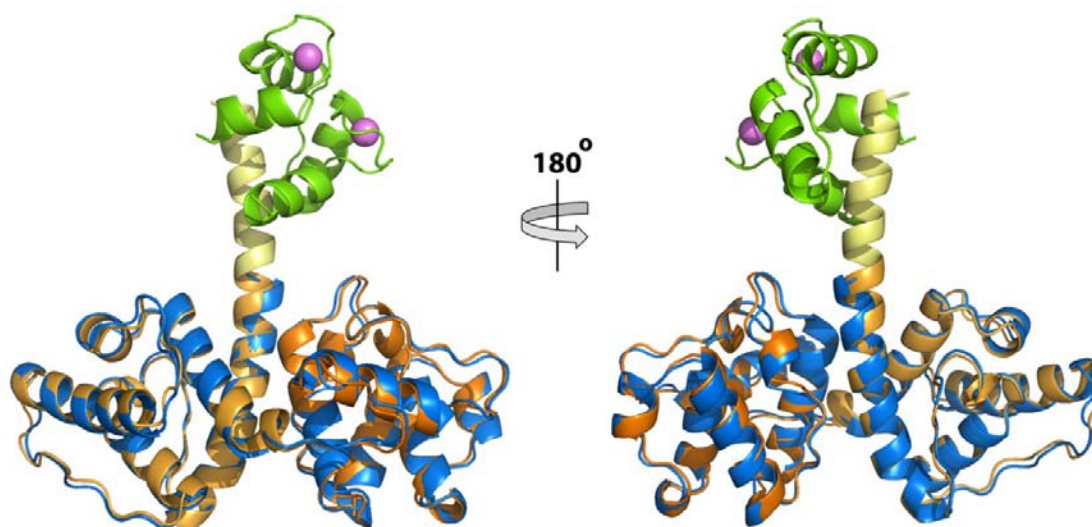


**Figure 3.18.** The crystal structure of P1aABD $_{\Delta 22}$  is shown in blue and superimposed to the P1aABD $_{\Delta 22}$ /CaM $_{NL}$  complex (RMSD: 0.69 Å over 209 equivalent C $\alpha$  atoms), demonstrating that the Ca $^{2+}$ /CaM binding does not affect the conformation of plectin ABD.

### 3.2.8. Molecular determinants for the preferable binding of CaM $_{NL}$

The remarkable feature of the Ca $^{2+}$ /CaM binding to plectin is that N-lobe displays a higher affinity than C-lobe. The molecular basis for the higher affinity of CaM $_{NL}$  was therefore assessed by structural and thermodynamics analyses. The structure of CaM $_{CL}$  (residues 82-146, PDB: 3CLN) was superimposed on the crystal structure of the P1aABD $_{\Delta 22}$ /CaM $_{NL}$  complex (RMSD: 0.50 Å over 58 equivalent C $\alpha$  atoms) and the structure of the P1aABD $_{\Delta 22}$ /CaM $_{CL}$  complex was generated.

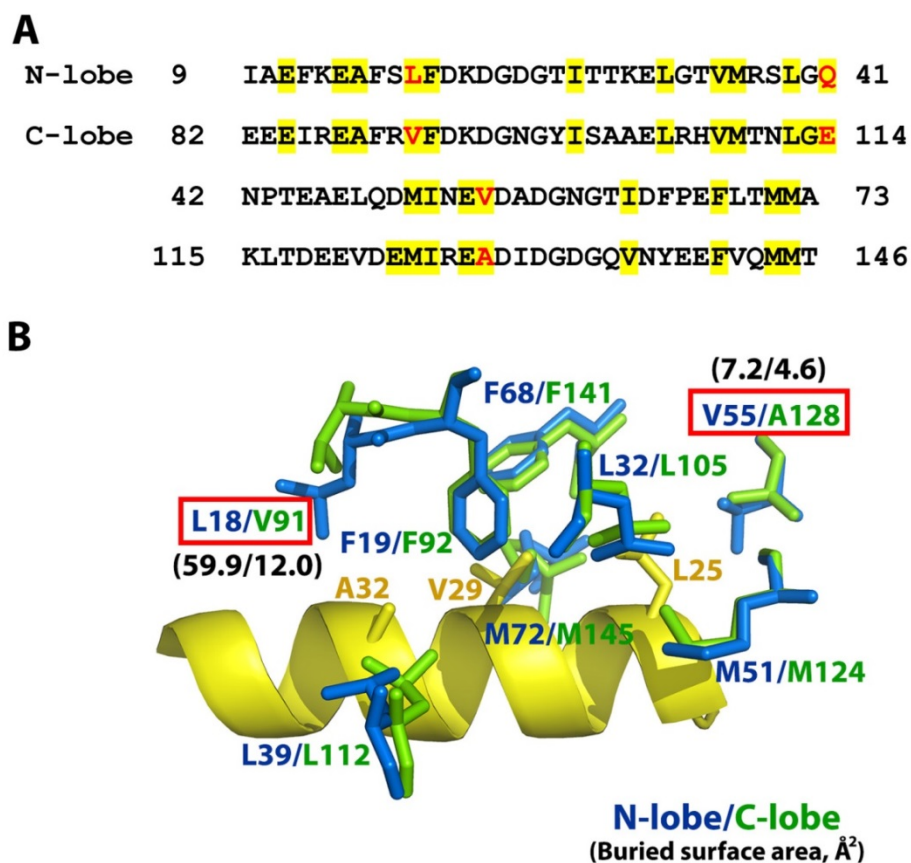


**Figure 3.19.** Comparison of CaM lobes for the P1a binding. **(A)** The sequence alignment of each lobe of CaM. The interfacing residues were analyzed by PDBePISA and shaded in yellow. Different residues between two lobes are shown in red **(B)** Interfacing hydrophobic residues of two lobes are superimposed and shown in sticks; N-lobe in blue and C-lobe in green, showing that Leu18 and Val55 in N-lobe coordinate larger hydrophobic interfaces than C-lobe. Hydrophobic residues of P1a corresponding to a 1-5-8 motif are displayed in yellow sticks.

Amino acid residues involved in the interaction were individually analyzed by PDBePISA (Krissinel & Henrick, 2007) and highlighted in yellow in the sequence alignment (**Figure 3.19A**). The majority of interface residues are highly conserved between two lobes (CaM<sub>NL</sub>/CaM<sub>CL</sub>: Phe19/Phe92, Leu32/Leu105, Leu39/Leu112, Met51/Met124, Phe68/Phe141, and Met72/Met145), nevertheless differences are in three positions

involved in polar or hydrophobic interactions: Gln41(CaM<sub>NL</sub>)/Glu114(CaM<sub>CL</sub>), Leu18(CaM<sub>NL</sub>)/Val91(CaM<sub>CL</sub>), and Val55(CaM<sub>NL</sub>)/Ala128(CaM<sub>CL</sub>) (**Figure 3.19A**). Although Glu114 in C-lobe has a potential to form a stronger interaction with P1aABD Arg31 residue (3.32 Å) than corresponding Gln41 in N-lobe (3.79 Å), the two hydrophobic residues in N-lobe (Leu18 and Val55) coordinate larger buried surface areas (59.9 and 7.2 Å<sup>2</sup>) than corresponding C-lobe residues: Val91 (12.0 Å<sup>2</sup>) and Ala128 (4.6 Å<sup>2</sup>), leading to the higher affinity (**Figure 3.19B**).

**Table 6.** Summary of PISA analysis

	P1aABD <sub>Δ22</sub> /CaM <sub>NL</sub>		P1aABD <sub>Δ22</sub> /CaM <sub>CL</sub>	
	P1aABD <sub>Δ22</sub>	CaM <sub>NL</sub>	P1aABD <sub>Δ22</sub>	CaM <sub>CL</sub>
Number of atoms	56 (2.8 %)	61 (12.3 %)	57 (2.9 %)	70 (13.3 %)
Number of residues	15 (6/9)	19 (15/4)	15 (6/9)	23 (17/6)
(Non-polar/polar)	(6.2 %)	(29.2 %)	(6.2%)	(35.4 %)
Solvent-accessible area (Å <sup>2</sup> )	664.8 (5.2 %)	634.7 (14.9 %)	671.0 (5.3%)	617.6 (13.4 %)
Solvation energy gain (kcal/mol)	-6.2 (2.9 %)	-6.7 (14.7 %)	-5.2 (2.4 %)	-5.4 (11.2)

PISA interface analysis shows that the total interface area of the CaM<sub>NL</sub> (634.7 Å<sup>2</sup>, 14.9% of solvent accessible surface area) is larger than that of the CaM<sub>CL</sub> (617.6 Å<sup>2</sup>, 13.4% of solvent accessible surface area) and that the complex formation of P1aABD<sub>Δ22</sub> with CaM<sub>NL</sub> is thermodynamically more favored (solvation energy gain: -12.9 kcal/mol for CaM<sub>NL</sub> vs -10.6 kcal/mol for CaM<sub>CL</sub>) (**Table 6**), which is in good agreement with experimental data of ITC, where CaM<sub>NL</sub> displays a higher affinity to P1aABD and is displaces CaM<sub>CL</sub> from a complex with P1aABD.

### 3.2.9. SAXS structure of the P1aABD/CaM complex

#### 3.2.9.1. *Ab initio* modeling

SAXS was carried out to decipher the solution structure of the P1aABD/CaM complex and to model the missing part of the crystal structure. Three samples with different concentrations (3.5, 6.0, and 8.4 mg/ml) were measure by SAXS, while the lowest concentration sample (3.5 mg/ml) was chosen for further studies due to the concentration dependence; overall structural parameters such as zero-angle intensity,  $I(0)$  and radius of gyration,  $R_g$  were analyzed by Guinier analyses. Data collection and structural parameters derived from SAXS analyses are summarized in **Table 7**.

**Table 7.** Data collection and scattering-derived parameters of the P1aABD/CaM complex

Data collection parameters		Structural parameters	
Instrument	SAXS beamline X33 (DESY)	$I(0)$ [from $P(r)$ ]	$47.44 \pm 0.01^*$
Sample to detector distance (m)	2.7 m	$R_g$ (nm) [from $P(r)$ ]	$3.17 \pm 0.01$
Wavelength (Å)	1.5	$I(0)$ (from Guinier)	$47.94 \pm 0.11$
$S$ range (Å <sup>-1</sup> )	0.08-0.6	$R_g$ (nm) (from Guinier)	$3.17 \pm 0.01$
Exposure time (sec)	15	Porod volume (nm <sup>3</sup> )	80.36
Temperature (K)	283	$D_{max}$ (nm)	10.4

\* Data are expressed as mean value  $\pm$  standard deviation.



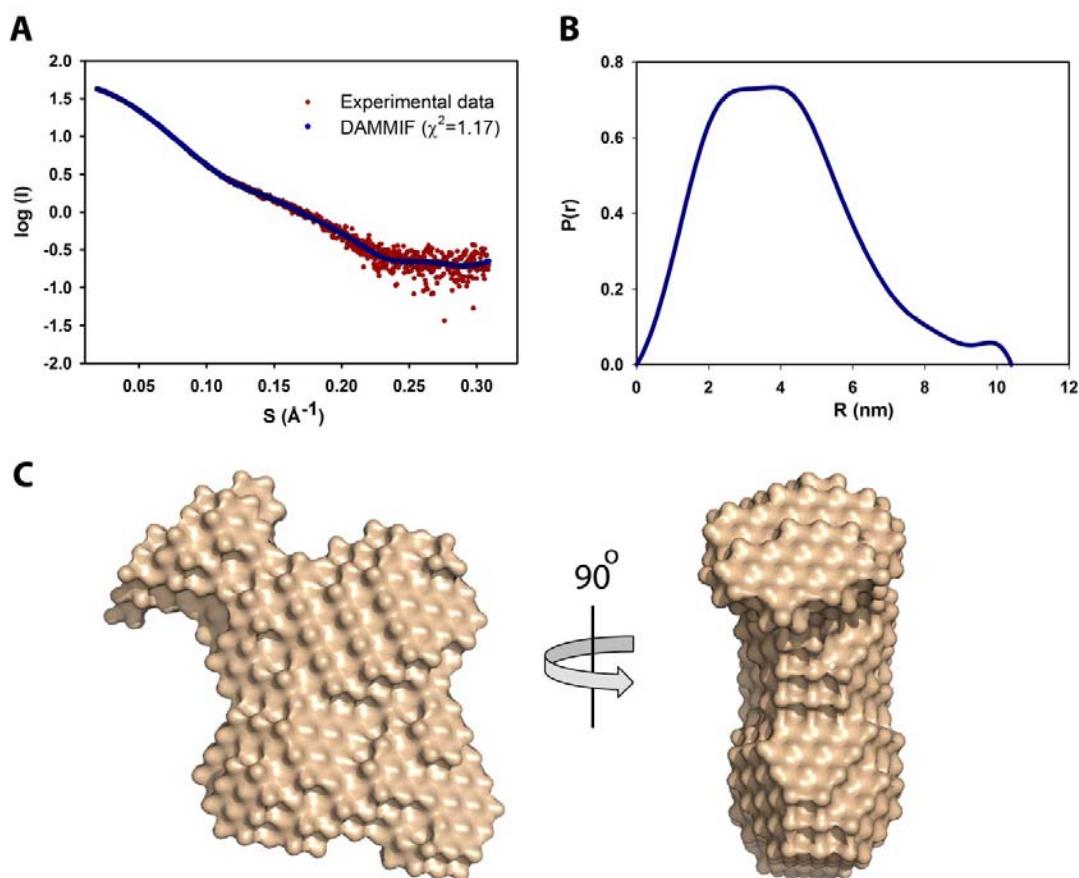


**Figure 3.20.** SAXS analyses on the P1aABD/CaM complex. **(A)** The experimental scattering curve of the complex is shown in red dots. The calculated scattering profile from *ab initio* modeling is fitted to the experimental data and displayed in blue line ( $\chi^2 = 1.17$ ). **(B)** The  $P(r)$  curve shows the  $D_{\max}$  (10.4 nm) of the complex. **(C)** The molecular surface of the averaged *ab initio* model is shown in different orientations (rotated 90° along Y-axis).

The overall structural parameter of the complex was analyzed by Guinier plot and  $P(r)$  curve, generating  $R_g$  of 3.17 nm and 3.14 nm respectively. *Ab initio* model construction was performed using the program DAMMIF ( $\chi^2=1.17$ , **Figure 3.20A**). The maximum dimension of the complex is 10.4 nm, determined by  $P(r)$  curve (**Figure 3.20B**). Twenty models generated were superimposed and averaged by the program DAMAVER. The



averaged model is shown in **Figure 3.20C**. SAXS structure suggests that CaM displays rather extended conformation than collapsed in complex with P1aABD in solution; nevertheless the molecular shape with low resolution limits the explanation about the molecular details of the interaction. Rigid-body modeling with high resolution structures was carried out to overcome the drawback of the *ab initio* modeling.

### 3.2.9.2. An extended conformation of CaM in complex with P1aABD

The program CORAL was employed to model the missing parts of the crystal structure of the P1aABD<sub>Δ22</sub>/CaM<sub>NL</sub> complex, which fits to the experimental data with the  $\chi$  value of 1.47 (**Figure 3.21A**), and superimposed to the averaged *ab initio* model (**Figure 3.21B**).

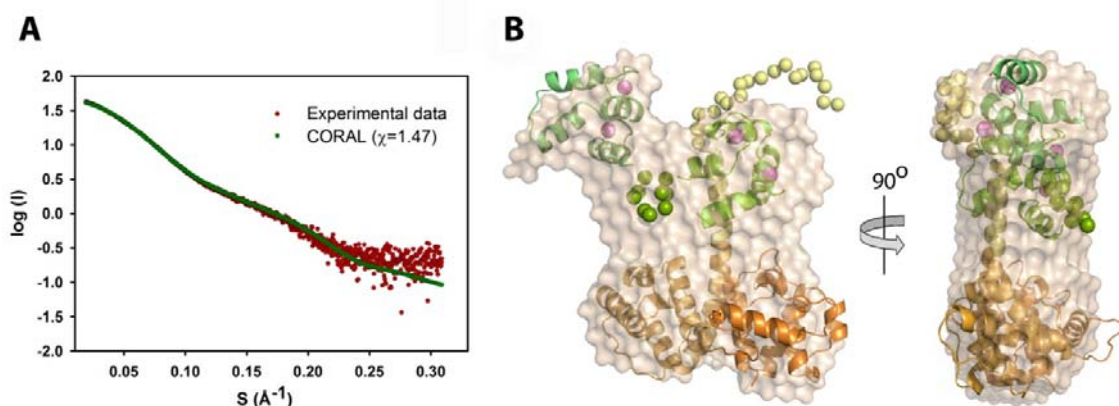


**Figure 3.21.** Rigid-body modeling of the P1aABD/CaM complex. **(A)** The simulated scattering profile of the rigid-body model fits to the experimental data ( $\chi=1.47$ ). **(B)** The *ab initio* molecular shape of the P1aABD/CaM complex is shown in gray, superimposed to the rigid-body model of the complex.

In the SAXS-derived molecular model of the P1aABD/CaM complex, Ca<sup>2+</sup>/CaM exhibits an extended conformation where the two lobes are connected with an inter-lobe linker

modelled with dummy residues. The  $R_g$  of CaM (20.95 Å) in the complex is calculated by CRY SOL (Svergun et al, 1995), which is similar to the  $R_g$  value of the solution structure of extended  $\text{Ca}^{2+}$ /CaM ( $21.3 \pm 0.2$  Å) (Heidorn & Trewella, 1988). The analysis of the model shows that the  $\text{CaM}_{\text{CL}}$  and the first 22 residues of the N-terminal segment (missing in P1aABD $_{\Delta 22}$ ) do not participate in the interaction at all.

		1	5	8	14
skMLCK	566	KRR <b>W</b> KKN <b>F</b> IA <b>V</b> SAANR <b>F</b> KKISS			
smMLCK	796	ARR <b>K</b> W <b>Q</b> KT <b>G</b> H <b>A</b> VRAIGR <b>L</b> SS			
Calcineurin	393	KEV <b>I</b> RNK <b>I</b> RA <b>I</b> GKMAR <b>V</b> FSVLR			
C20W	1102	RGQIL <b>W</b> FRGL <b>N</b> RI <b>I</b> QTQIK			
Munc13-1	459	RAKAN <b>W</b> LRA <b>F</b> N <b>K</b> <b>V</b> RMQLQEARGE <b>G</b> EMSKSL <b>W</b> <b>F</b>			
Plectin 1a	20	SS <b>E</b> DN <b>L</b> YL <b>A</b> VLR <b>A</b> SEGKKDERDRV			

**Figure 3.22.** Sequence alignment of CaM binding motifs. The hydrophobic residues corresponding to the CaM binding motifs are highlighted in red. skMLCK, smMLCK, and calcineurin are classified into a 1-5-8-14 motif, whereas C20W and plectin 1a belong to a 1-5-8 motif. Munc13-1 has a 1-5-8-26 CaM-binding motif.

The CaM binding motif of the N-terminal tail is classified into a 1-5-8 motif (Leu25-Val29-Ala32), which is a sub-group of a 1-5-8-14 class (**Figure 3.22**) (Elshorst et al, 1999; Rhoads & Friedberg, 1997). The extended, non-canonical conformation of  $\text{Ca}^{2+}$ /CaM in the bound form has been reported in several cases (Drum et al, 2002; Elshorst et al, 1999; Rodriguez-Castaneda et al, 2010; Schumacher et al, 2001). However, to my knowledge, this is the first finding that N-lobe of CaM plays the major role in the interaction with the binding partner in an extended conformation.

### 3.3. Studies on the plectin 1a actin-binding domain/integrin $\beta 4$ complex

#### 3.3.1. Construct design

The integrin  $\beta 4$  construct termed  $\beta 4\text{Fn}12$  (1126-1355) comprises the first pair of fibronectin type III domains including a part of the connecting segment (CS) of integrin  $\beta 4$  (Niessen et al, 1997) (**Figure 3.23**). P1aABD was employed for the interaction study with integrin  $\beta 4$ .

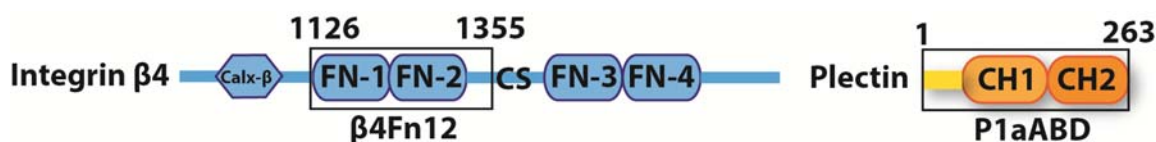


**Figure 3.23.** Schematic diagram of integrin  $\beta 4$  and plectin 1a constructs. Cytoplasmic domain of integrin  $\beta 4$  is shown in blue; fibronectin type III domain is named FN and CS is the connecting segment between FnIII-2 and 3 domains.

#### 3.3.2. Purification of $\beta 4\text{Fn}12$

Expressed  $\beta 4\text{Fn}12$  was purified as the same way used for plectin and calmodulin constructs, and finally purified using a Superdex 75 26/60 gel filtration column (GE Healthcare) (**Figure 3.24A**). The fractions of the peak were collected and analyzed by SDS-PAGE to measure the purity of samples (**Figure 3.24B**).

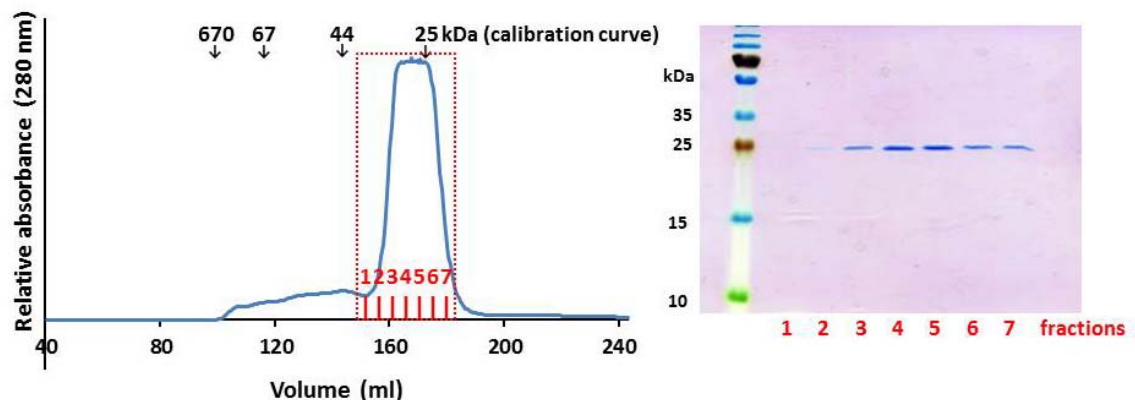


**Figure 3.24.** Purification of  $\beta 4\text{Fn}12$ . **(A)** Elution profile of  $\beta 4\text{Fn}12$  using a Superdex 75 26/60 column.  $\beta 4\text{Fn}12$  was eluted at the peak around 170 ml, corresponding to the molecular weight estimation of 35 kDa. **(B)** SDS-PAGE analysis of the fractions. The gel (15% of acrylamide) was stained with Coomassie brilliant blue.

### 3.3.3. Crystallization and structure determination of the $\text{P1aABD}_{\Delta 22}/\beta 4\text{Fn}12$ complex

The crystal structure of the  $\text{P1cABD}/\beta 4\text{Fn}12$  complex was determined (de Pereda et al, 2009); however only plectin 1a is regulated by  $\text{Ca}^{2+}/\text{CaM}$  (Kostan et al, 2009) and co-localized with hemidesmosomes in basal keratinocytes (Andra et al, 2003). In addition, the results suggested “coupled folding and binding” mechanism for a P1a isoform specific sequence when binding to  $\text{Ca}^{2+}/\text{CaM}$ , which suggests that P1a isoform specific sequence might display the similar behavior upon binding to integrin  $\beta 4$ . In order to address this question, the integrin  $\beta 4$  construct ( $\beta 4\text{Fn}12$ : residues 1126-1355) was used to crystallize with  $\text{P1aABD}_{\Delta 22}$ . Due to the low affinity of the interaction between plectin 1aABD and  $\beta 4\text{Fn}12$  ( $K_d$ : 41.7), the protein complex was not eluted from a size-exclusion chromatography.  $\text{P1aABD}_{\Delta 22}$  was mixed with  $\beta 4\text{Fn}12$  in an equal molar ratio and concentrated to 12 mg/ml, which was used for crystallization. Crystals of the protein

complex were grown at 22 °C using vapor diffusion methods, consisted of equal volumes of the protein sample and the crystallization solution containing 20 mM HEPES pH 6.5, 150 mM Sodium formate, 7.5% PEG 5500 MME, and 3% Sucrose. The obtained crystals were treated with several dehydration methods (**Section 5.5.4**). After dehydration, the crystals were flash frozen with liquid nitrogen for the diffraction experiments. Diffraction data were collected using the beamline ID23-2 at ESRF. The structure of the complex was solved by molecular replacement; plectin ABD (PDB: 1MB8) (Garcia-Alvarez et al, 2003) and integrin  $\beta 4$  fragment (PDB: 3F7Q) (de Pereda et al, 2009) were used for search models.

#### 3.3.4. Crystal structure of the P1aABD $_{\Delta 22}$ / $\beta 4$ Fn12 complex

The crystal structure of the P1aABD $_{\Delta 22}$ / $\beta 4$ Fn12 complex was determined to 4.0 Å resolution and refined to final  $R_{work}$  and  $R_{free}$  factors of 0.217 and 0.285, respectively (**Figure 3.25A and Table 8**). The asymmetric unit contains two P1aABD $_{\Delta 22}$  molecules and an anti-parallel  $\beta 4$ Fn12 homo-dimer as observed previously (de Pereda et al, 2009; de Pereda et al, 1999); one of  $\beta 4$ Fn12 subunits binds to one P1aABD $_{\Delta 22}$  molecule, while another  $\beta 4$ Fn12 does not have any contact with P1aABD $_{\Delta 22}$  molecules. The crystal structure of the P1aABD $_{\Delta 22}$ / $\beta 4$ Fn12 was superimposed to the crystal structure of P1cABD/ $\beta 4$ Fn12 (PDB: 3F7P) (de Pereda et al, 2009) to compare the integrin  $\beta 4$  binding to the two different plectin isoforms. RMSD of 0.87 Å over 367 equivalent C $\alpha$  atoms suggests that the binding interface of  $\beta 4$ Fn12 maps to the same site of plectin isoforms 1a and 1c and that no substantial conformational changes of the subunits occurred. The FnIII domain has a beta sandwich structure consisting of two  $\beta$ -sheets; one is consisted of A, B, and E strands and another possesses C, C', F and G strands (Campbell & Spitzfaden, 1994). One side of FnIII-2, comprising A, B, and E strands and interconnecting loops, faces the tip of C-helix and neighboring two short helices (B and E) of CH1. Three salt bridges between CH1 domain of ABD and FnIII-2 domain of integrin  $\beta 4$  identified in the P1cABD/ $\beta 4$ Fn12 are essential for the interaction as proven by mutational analyses (de Pereda et al, 2009;

Koster et al, 2001). They are also conserved in the P1aABD $_{\Delta 22}$ /β4Fn12 complex: Asp123/Arg1225 (2.60 Å), Arg71/Glu1242 (3.04 Å), and Glu68/Arg1281 (2.57 Å) (**Figure 3.25B**). 15 amino acid residues corresponding to the N-terminal extension of P1aABD $_{\Delta 22}$  are not visible in the electron density of P1aABD $_{\Delta 22}$ /β4Fn12 crystal structure, suggesting that the N-terminal segment is again disordered in the complex and does not play a role for the interaction with integrin β4.

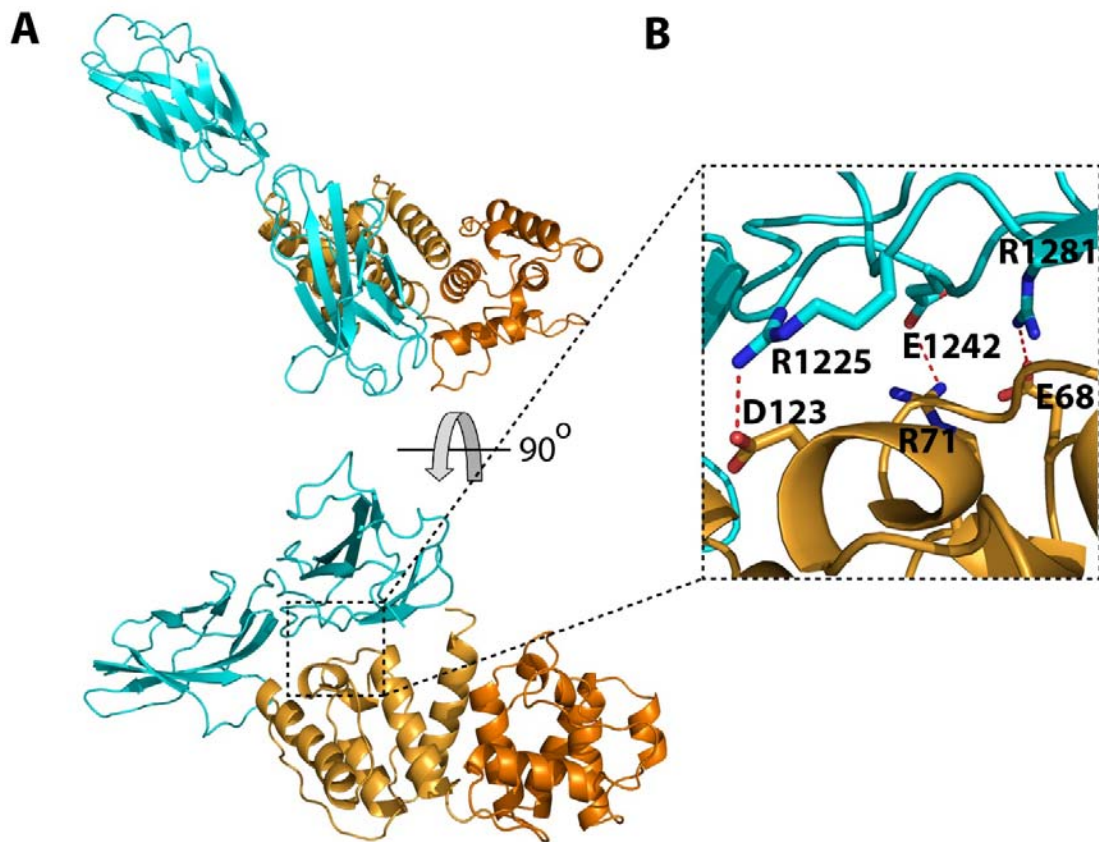


**Figure 3.25.** Crystal structure of the P1aABD $_{\Delta 22}$ /β4Fn12 complex. **(A)** The crystal structure is shown in two different orientations (rotated 90° along x-axis); P1aABD $_{\Delta 22}$  and β4Fn12 are respectively displayed in orange and cyan. **(B)** The binding interface comprises three salt bridges: Asp123/Arg1225 (2.60 Å), Arg71/Glu1242 (3.04 Å), and Glu68/Arg1281 (2.57 Å).

**Table 8.** Data collection and refinement statistics P1aABD<sub>Δ22</sub>/β4Fn12

DATA COLLECTION		REFINEMENT	
Source	ID23-2 (ESRF)	R <sub>work</sub> <sup>d</sup>	0.224
Wavelength (Å)	0.873	R <sub>free</sub> <sup>e</sup>	0.287
Resolution (Å)	48.16-4.0 (4.47-4.0) <sup>a</sup>	R.m.s.d. bonds (Å)	0.004
Space group	P6 <sub>5</sub>	R.m.s.d. angles (°)	0.888
Unit cell (Å, °)	a= 96.32, b= 96.32, c= 207.8 α= 90, β= 90, γ= 120	Wilson B factor	99.74
Molecules / a.u.	4	MOLPROBITY <sup>f</sup> STATISTICS	
Unique reflections	9188 (2594)	All-atom clash score	14.46
Completeness (%)	99.1 (99.5)	Ramachandran plot	
R <sub>merge</sub> <sup>b</sup>	0.272 (0.793)	Outliers	0.12 %
R <sub>meas</sub>	0.300 (0.879)	Allowed	6.64 %
R <sub>pim</sub> <sup>c</sup>	0.123 (0.364)	Favored	93.23 %
Multiplicity	5.7 (5.6)	Rotamer outliers	0.82 %
Mean I/sig(I)	7.4 (3.9)	C-beta deviations	1
CC (1/2)	0.977(0.751)		

<sup>a</sup>Values in parentheses are for the highest resolution shell.

$${}^b R_{merge} = \frac{\sum_{hkl} \sum_j |I_{hkl,j} - \langle I_{hkl} \rangle|}{\sum_{hkl} \sum_j I_{hkl,j}} \quad {}^c R_{pim} = \frac{\sum_{hkl} \sqrt{\frac{1}{n-1}} \sum_{j=1}^n |I_{hkl,j} - \langle I_{hkl} \rangle|}{\sum_{hkl} \sum_j I_{hkl,j}}$$

<sup>d</sup>R<sub>work</sub> = Σ|Fo-Fc| / ΣFo, <sup>e</sup>R<sub>free</sub> is the cross-validation. <sup>d</sup>R<sub>work</sub> computed for the test set of reflections (5 %) which are omitted in the refinement process.

<sup>f</sup> (Chen et al, 2010)

This observation was further supported by SAXS analysis, which revealed the presence of the N-terminal tail of plectin in a number of variable conformations (**Figure 3.6C**). This suggests that the main function of the N-terminal tail is not binding to integrin  $\beta 4$ , but regulating P1a-integrin  $\beta 4$  interaction *via* binding to  $\text{Ca}^{2+}$ /CaM.

### 3.3.5. SAXS structure of the P1aABD/ $\beta 4$ Fn12 complex

SAXS experiment was carried out to understand the structure of the P1aABD/ $\beta 4$ Fn12 complex in solution. The protein samples with different concentrations (2.4~15.5 mg/ml) were measured by SAXS, while the lowest concentration sample (2.4 mg/ml) was chosen for modeling to minimize the concentration dependence, detected by comparing  $I(0)$  and  $R_g$  obtained from Guinier analyses. Data collection and structural parameters derived from SAXS analyses are summarized in **Table 9**.

**Table 9.** Data collection and scattering-derived parameters of the P1aABD/  $\beta 4$ Fn12 complex

Data collection parameters		Structural parameters	
Instrument	SWING beamline at the synchrotron SOLEIL	$I(0)$ [from $P(r)$ ]	$0.0429 \pm 0.0001^*$
Sample to detector distance (m)	1.8 m	$R_g$ (nm) [from $P(r)$ ]	$2.90 \pm 0.01$
Wavelength (Å)	1.03	$I(0)$ (from Guinier)	$0.0430 \pm 0.0057$
S range (Å <sup>-1</sup> )	0.04-0.38	$R_g$ (nm) (from Guinier)	$2.85 \pm 0.6$
Exposure time (sec)	500	Porod volume (nm <sup>3</sup> )	48.87
Temperature (K)	283	Dmax (nm)	9.0

\*Data are expressed as mean value  $\pm$  standard deviation.



The overall structural parameter of the complex was analyzed by Guinier plot and P(r) curve, generating  $R_g$  of 2.85 nm and 2.90 nm respectively. *Ab initio* model construction was performed using the program DAMMIF ( $\chi^2=1.01$ , **Figure 3.26A**). The maximum dimension of the complex is 9.0 nm, determined by P(r) curve (**Figure 3.26B**). Twenty models generated were superimposed and averaged by the program DAMAVER. The averaged model is shown in different orientations (rotated 90° along x-axis, **Figure 3.26C**).

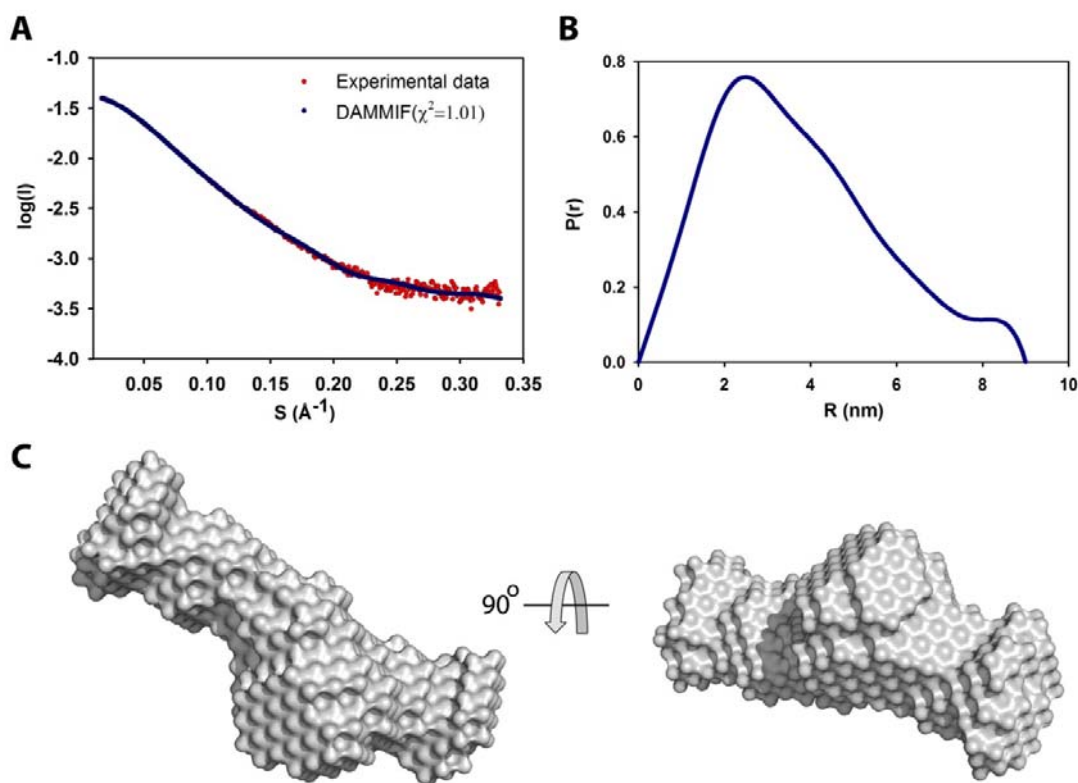


**Figure 3.26.** SAXS studies on the P1aABD/ $\beta$ 4Fn12 complex. **(A)** The experimental scattering curve of the complex is shown in red dots. The calculated scattering profile from *ab initio* modeling is fitted to the experimental data and displayed in blue line ( $\chi^2 = 1.01$ ). **(B)** The  $P(r)$  curve shows the  $D_{\max}$  (9.0 nm) of the complex. **(C)** The molecular surface of the averaged *ab initio* model is shown in different orientations (rotated 90° along x-axis).

The scattering data was simulated from the crystal structure of the P1aABD $_{\Delta 22}$ /β4Fn12 complex by OLIGOMER (**Figure 3.27A**). I employed the program OLIGOMER to calculate the volume fractions of the complex and each subunit in solution, since the concentration of the sample used (41.3 μM) is similar with the  $K_d$  of the complex (41.7 μM), causing a polydisperse solution (62.0% dissociated). The proportions of the volume fractions were estimated like the followings: 53.7 % for the complex, 25.4 % for P1aABD, and 20.8 % for β4Fn12, fitting well to the experimental data ( $\chi^2 = 0.90$ ). The SAXS structure was superimposed to the crystal structure of the P1aABD $_{\Delta 22}$ /β4Fn12 complex, showing a good agreement between SAXS and crystal structures of the P1aABD/β4Fn12 complex (**Figure 3.27B**).

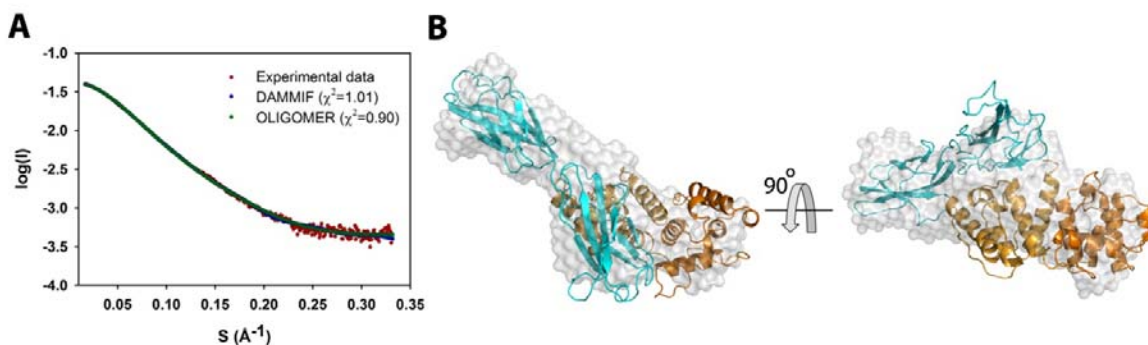


**Figure 3.27.** Comparing crystal and SAXS structures. **(A)** The scattering profile of the crystal structure was simulated by OLIGOMER, exhibiting a good agreement with the experimental data ( $\chi^2 = 0.90$ ). **(B)** The crystal structure of P1aABD $_{\Delta 22}$ /β4Fn12 complex is superimposed to the SAXS structure.

### 3.4. Disassembly of the P1aABD/ $\beta$ 4Fn12 complex by CaM binding

#### 3.4.1. *In silico* analysis of the dissociation mechanism

The dissociation mechanism was simulated by superimposing two structures of the CaM/P1aABD complex and the P1aABD $_{\Delta 22}$ / $\beta$ 4Fn12 complex. The rigid body model of the P1aABD/CaM complex and the crystal structure of the P1aABD $_{\Delta 22}$ / $\beta$ 4Fn12 complex were superimposed to plectin ABD (RMSD: 0.765Å over 206 C $\alpha$  atoms, Figure 5A) to mimic the CaM binding to the P1aABD $_{\Delta 22}$ / $\beta$ 4Fn12 complex. As shown in **Figure 3.28**, the N-terminal tail and CaM generate steric hindrances against FnIII-2 domain, resulting in the disruption of the  $\beta$ 4Fn12 binding to plectin ABD.

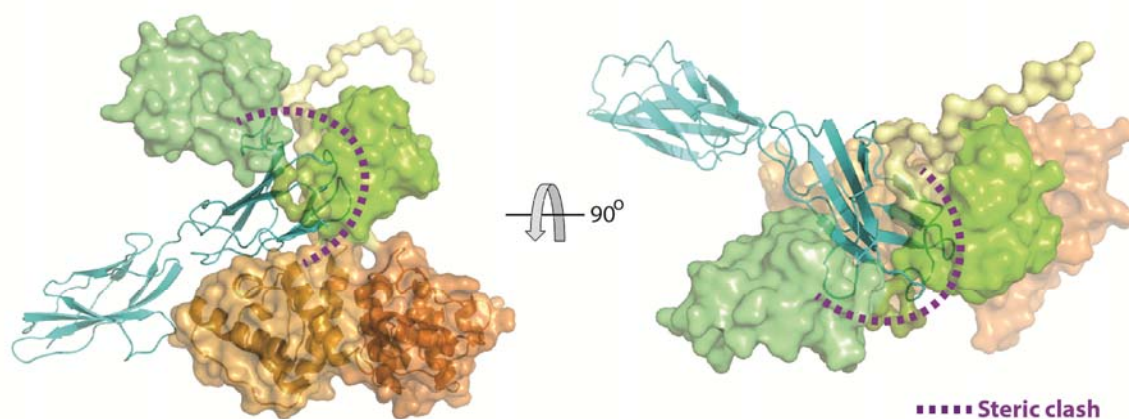


**Figure 3.28.** The structure of the CaM/P1aABD complex are superimposed to plectin ABD of the P1aABD $_{\Delta 22}$ / $\beta$ 4Fn12 complex (RMSD 0.77 Å over 206 equivalent C $\alpha$  atoms), generating steric clashes with the FnIII-2 domain indicated in purple.

### 3.4.2. Competitive binding assay by displacement ITC

I further carried out ITC to analyse thermodynamics of the dissociation and interactions between CaM,  $\beta$ 4Fn12, and P1aABD. The  $\beta$ 4Fn12 binding to P1aABD is an entropy-driven reaction, having weak affinity ( $K_d$  41.7  $\mu$ M, **Figure 3.29A**), while the  $\text{Ca}^{2+}$ /CaM binding is enthalpy-favoured process, and an order of magnitude stronger than the  $\beta$ 4Fn12 binding ( $K_d$  4.2  $\mu$ M, **Figure 3.29B**). No interaction was observed between  $\text{Ca}^{2+}$ /CaM and  $\beta$ 4Fn12 (**Figure 3.30A**).

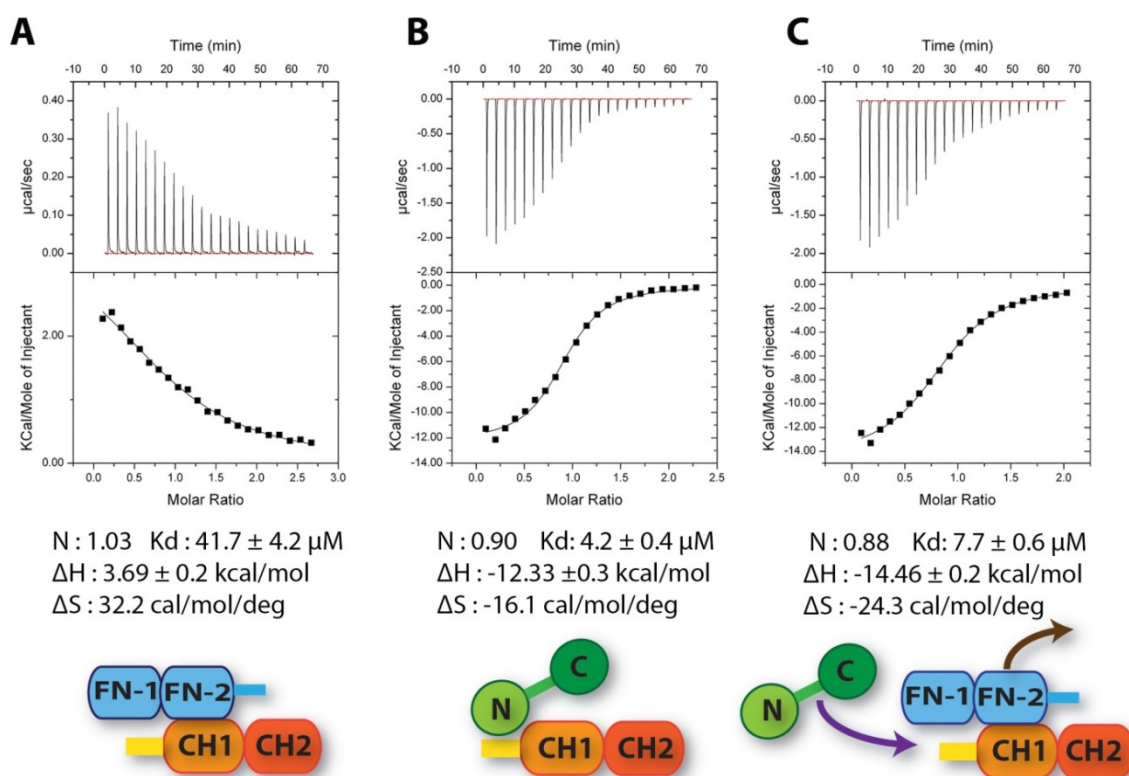


**Figure 3.29.** The displacement of  $\beta$ 4Fn12 by  $\text{Ca}^{2+}$ /CaM assessed by ITC. **(A)** 0.8 mM  $\beta$ 4Fn12 was titrated into 0.08 mM P1aABD, exhibiting the entropy-driven binding. **(B)** 1 mM CaM was titrated into 0.1 mM P1aABD. CaM binds to P1aABD with a higher affinity than  $\beta$ 4Fn12. **(C)** 1 mM CaM was injected into the sample cell containing 0.1 mM P1aABD and 0.1 mM  $\beta$ 4Fn12 for the displacement binding assay. All ITC measurements were carried out at 30  $^{\circ}\text{C}$  of isotherm. Data are expressed as mean values  $\pm$  standard deviations.

In the displacement experiment  $\text{Ca}^{2+}/\text{CaM}$  was titrated to the P1aABD/ $\beta 4\text{Fn}12$  complex, the apparent binding affinity of  $\text{Ca}^{2+}/\text{CaM}$  was reduced because of the competitive binding of  $\beta 4\text{Fn}12$  to P1aABD, and the enthalpy and entropy changes ( $\Delta H$  and  $\Delta S$ ) were enlarged due to the replacement of an entropic binding with an enthalpic one (**Figure 3.29C**).

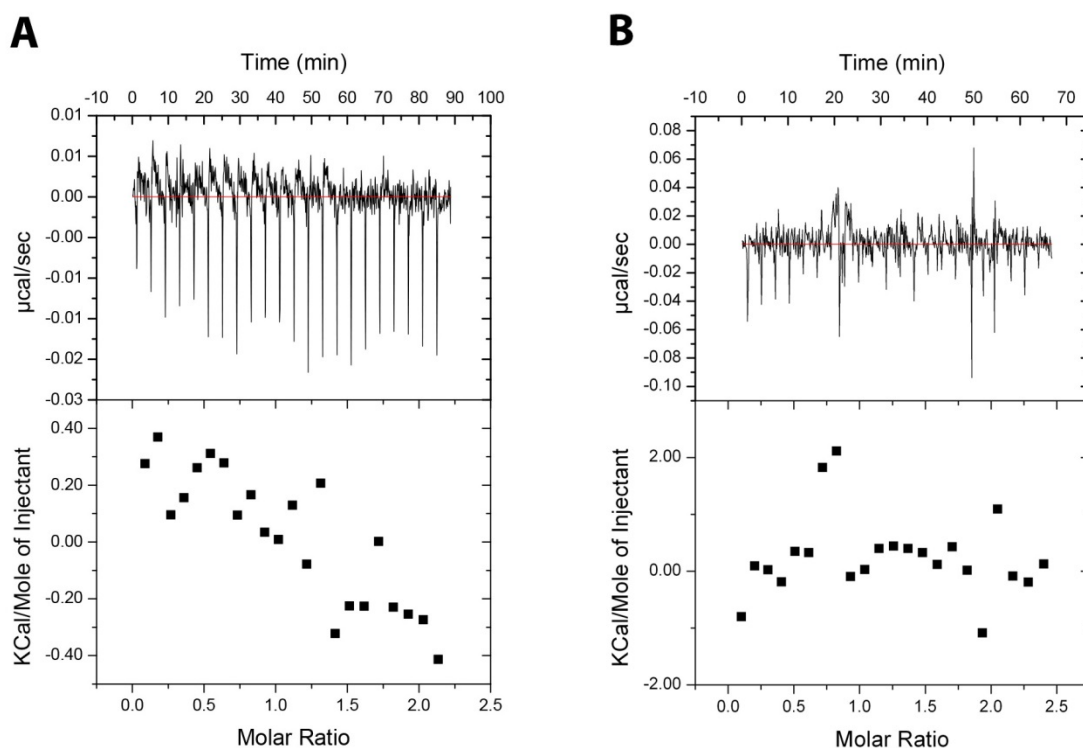


**Figure 3.30.** ITC analyses **(A)** 0.4 μM CaM was titrated to 0.04 μM β4Fn12 at 30°C, displaying the no interaction. **(B)** 0.7 mM CaM<sub>NL</sub> is titrated to 0.07 mM of P1aABD and β4Fn12; ITC experiment was carried out at 30 °C. CaM<sub>NL</sub> binds to P1aABD in the presence of β4Fn12 with the lower affinity ( $K_d$  of 21.5 μM).

The measured binding affinity of  $\text{Ca}^{2+}/\text{CaM}$  is identical to the calculated one using the competitive binding model by Origin software (Sigurskjold, 2000). The displacement-binding assay demonstrates that the  $\text{Ca}^{2+}/\text{CaM}$  binding to P1aABD leads to the disassembly of the P1aABD/ $\beta 4\text{Fn}12$  complex. When CaM<sub>NL</sub> is titrated to the P1aABD/ $\beta 4\text{Fn}12$  complex,

it is also able to displace  $\beta$ 4Fn12 and to bind to P1aABD as expected from the affinity differences: CaM<sub>NL</sub> possesses a higher affinity ( $K_d$  of 10.5  $\mu$ M) than  $\beta$ 4Fn12 ( $K_d$  of 41.7  $\mu$ M) to P1aABD, which suggests that the CaM<sub>NL</sub> binding is sufficient to disrupt the interaction between P1aABD and  $\beta$ 4Fn12 (**Figure 3.30B**).

Thermodynamics of the  $\beta$ 4Fn12 and Ca<sup>2+</sup>/CaM interaction to P1aABD was compared to elucidate the mechanism of integrin  $\beta$ 4 dissociation. The formation of P1aABD/ $\beta$ 4Fn12 complex is not enthalpy-favourable ( $\Delta H$ : 3.69 kcal/mol, **Figure 3.29A**). The interaction is namely entropy-driven, indicating that ordered water molecules solvating each binding partner are released upon complex formation (Cozzini et al, 2004; Dunitz, 1994). For the P1aABD/CaM interaction, the results show that the disordered N-terminal tail of plectin isoform 1a folding into an  $\alpha$ -helix is coupled with binding to Ca<sup>2+</sup>/CaM. This reaction is entropy-unfavourable as shown by ITC results (**Figure 3.29B**). However, the enthalpy contribution compensates the entropy cost to instigate the binding reaction (**Figure 3.29B and C**) (Dyson & Wright, 2005), which is inferred from the fact that the binding affinity of Ca<sup>2+</sup>/CaM to P1aABD ( $K_d$ : 4.2  $\mu$ M) is lower than to other binding partners reported ( $K_d$  of 10<sup>-7</sup> to 10<sup>-11</sup> M) (Crivici & Ikura, 1995). Taken together the results show that the Ca<sup>2+</sup>/CaM has a higher affinity to P1aABD than does  $\beta$ 4Fn12, resulting in capacity to displace of  $\beta$ 4Fn12 from complex with P1aABD.

## 4. DISCUSSION

It has been shown that the hemidesmosome disassembly is regulated by phosphorylation on multiple sites of integrin  $\beta 4$ . Under the EGF or PMA stimuli, extracellular signal-regulated kinase (ERK) 1/2 and ribosomal s6 kinase (p90RSK)1/2 phosphorylate integrin  $\beta 4$  Ser1356 and Ser1364 residues positioned in the connecting segment (CS) between FnIII-2 and 3 domains, interfering with the interaction between integrin  $\beta 4$  and plectin ABD (Frijns et al, 2010), whereas previous studies reported that calcium regulated protein kinase C (PKC) phosphorylates Ser1356, Ser1360, and Ser1364, resulting in mobilization of integrin  $\beta 4$  from hemidesmosomes and its association with F-actin (Rabinovitz et al, 2004; Wilhelmsen et al, 2007). The phosphorylation of integrin  $\beta 4$  at its C-terminal tail (Thr1736) mediated by PKD1 reduces the interaction with plakin domain of plectin (Frijns et al, 2012). The results show that the  $\text{Ca}^{2+}$ /CaM binding to the N-terminal extension of plectin isoform 1a is sufficient to disrupt the interaction between plectin ABD and the first pair of FnIII domains of integrin  $\beta 4$ , contributing along with the phosphorylation on integrin  $\beta 4$  to the hemidesmosome dissociation. Structural analysis of the P1aABD $_{\Delta 22}$ / $\beta 4$ Fn12 and P1aABD $_{\Delta 22}$ /CaM complexes, together with thermodynamic and mutational studies allowed to elucidate molecular mechanism of  $\text{Ca}^{2+}$ /CaM regulation of hemidesmosome disassembly *via* disruption of integrin  $\beta 4$  from P1a interaction.

### 4.1. The role of the isoform specific sequence of plectin 1a

The disassembly of the plectin and integrin  $\beta 4$  complex is isoform-specific and calcium-dependent. Alternative splicing at 5'-end of plectin gene generates 11 first exons, encoding diverse N-terminal extensions that determine cellular locations of isoforms (Fuchs et al, 1999; Reznicek et al, 2003). In mouse keratinocytes, plectin 1a is specifically located in hemidesmosomes, whereas plectin 1c is co-localized with microtubules (Andra et al, 2003).  $\text{Ca}^{2+}$ /CaM only binds to plectin 1a among three isoforms tested (P1a, P1c, and

P1f) (Kostan et al, 2009). Structural analysis showed that architectures and nature of interactions in complexes between integrin  $\beta 4$  FnIII-2 domain with P1aABD or P1cABD are identical (RMSD of 0.87 Å over 367 equivalent C $\alpha$  atoms) except for the N-terminal isoform specific tail: five residues in the N-terminal extension of 1cABD are bound to FnIII-2 domain *via* hydrogen bonds from the polypeptide backbone. These residues are not conserved in P1a isoform, where the entire N-terminal extension is intrinsically disordered and therefore not detectable in electron density. Binding affinities of P1a and P1c to integrin  $\beta 4$  are comparable ( $K_d$  of  $28 \pm 5$   $\mu$ M for P1aABD and  $K_d$  of  $31 \pm 4$   $\mu$ M for P1cABD) (de Pereda et al, 2009), suggesting that the N-terminal extensions of plectin isoforms (1a and 1c) do not play a determinant role in the complex formation of plectin with integrin  $\beta 4$ .

#### 4.2. The non-canonical binding of calmodulin in an extended conformation

The CaM binding motif of P1aABD belongs to a 1-5-8 class, bearing hydrophobic residues at these positions (Leu25-Val29-Ala32), which is a sub-group of a 1-5-8-14 motif (**Figure 3.22**) (Rhoads & Friedberg, 1997). Interestingly, CaM displays an extended conformation when it binds to P1aABD recognition site, which lacks a hydrophobic residue at position 14 in a 1-5-8-14 motif group (Elshorst et al, 1999; Rodriguez-Castaneda et al, 2010). In the CaM/C20W (the N-terminal calmodulin binding domain of plasma membrane Ca<sup>2+</sup> pump) complex (PDB: 1CFF) the C-lobe binds to the peptide (1-5-8 motif), exhibiting an extended conformation (Elshorst et al, 1999). In addition, the CaM binding motif of Munc13-1 (a synaptic vesicle priming protein) features a 1-5-8-26 motif, where residues corresponding to a 1-5-8 motif are responsible for the interaction with calmodulin C-lobe while the hydrophobic residue at position 26 binds to the N-lobe (PDB:2KDU) (Rodriguez-Castaneda et al, 2010). On the other hand, a peptide of skeletal muscle light chain kinase (skMLCK), possessing a 1-5-8-14 CaM binding motif, recruits CaM in a collapsed conformation by anchoring a hydrophobic residue at position 14 into N-lobe (PDB: 2BBM) (Ikura et al, 1992).



Plectin 1a hosts Asp38 at position 14, indicating that C-lobe of CaM is not able to bind to plectin due to the absence of a hydrophobic residue at this site. In addition, Asp38 is the first residue of A-helix, which comprises the core of CH1 domain. Binding of C-lobe to this site would lead to a steric clash with plectin and calmodulin. In order to simulate binding of calmodulin C-lobe to plectin Asp38, crystal structure of the CaM bound to smMLCK (skeletal muscle myosin light chain kinase) (PDB: 1CDL) (Meador et al, 1992) (RMSD: 0.684Å over 57 Cα), which contains the CaM binding motif 1-5-8-14 (**Figure 3.22**) was superimposed on our P1aABD<sub>Δ22</sub>/CaM<sub>NL</sub> complex. The analysis of the superposition shows that the C-helix of CaM C-terminal lobe of the CaM/smMLCK complex generates a steric clash against plectin ABD (**Figure 4.1**).

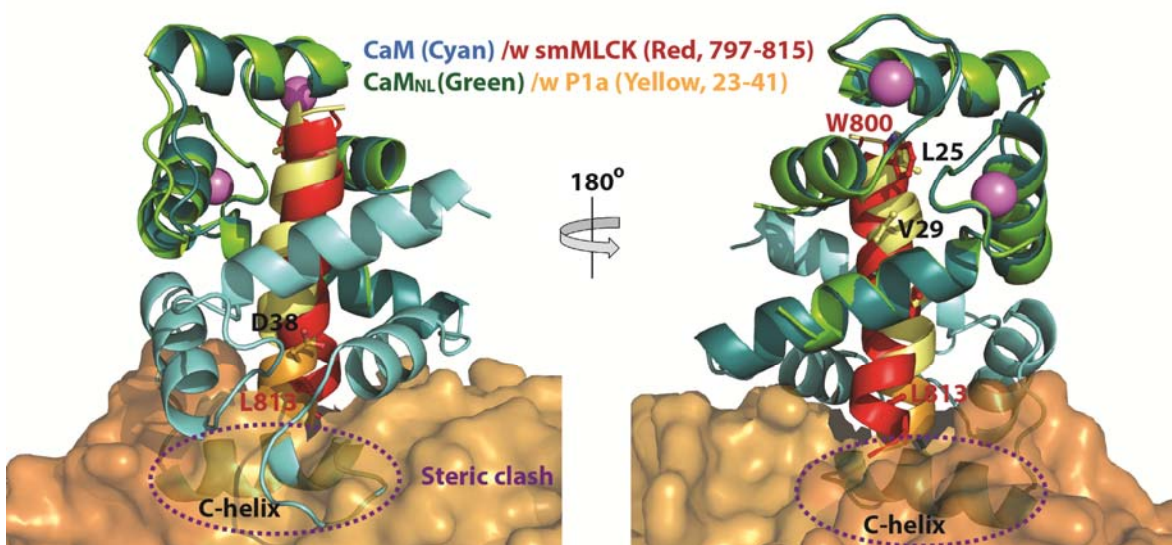


**Figure 4.1.** The crystal structure of the P1aABD<sub>Δ22</sub>/CaM<sub>NL</sub> complex superimposed on the crystal structure of the CaM/smMLCK complex (PDB:1CDL) (RMSD: 0.684Å over 57 Cα); N and C-lobes are respectively displayed in light and dark cyan and smMLCK peptide (797-815 residues) is shown in red. The superposition shows that C-helix of N-lobe makes a steric clash with plectin ABD (shown in an orange molecular surface).

In all cases mentioned above, C-lobe plays a major role for the binding, assisted by secondary role of the N-terminal lobe. To my knowledge, this is the first example of the preferential  $\text{Ca}^{2+}$ /CaM N-terminal lobe binding to the binding partner in extended conformation.

#### 4.3. Calmodulin is the first reported binding partner of isoform specific sequences of plectin

Plectin features isoform diversity by alternative splicing at the 5'-end of plectin gene, generating variable N-terminal sequences, which determine tissue-specific distribution of isoforms (Fuchs et al, 1999). My bioinformatics, biophysical and structural studies show that N-terminal tail of plectin 1a is disordered. However, bioinformatics analysis of plectin N-terminal extensions in other isoforms suggests that this is not a common feature among plectin isoforms (**Figure 3.3**). The first exon encoded regions of plectin 1b and 1g are expected to be mostly ordered, whereas plectin 1a, 1c, and 1d show strong tendencies for being intrinsically disordered. Albeit the subcellular co-localization partners of plectin isoforms are well known: plectin 1a with hemidesmosomes, plectin 1b with mitochondria, plectin 1c with microtubules, plectin 1d with Z-disk, plectin 1 and 1f with costameres (Andra et al, 2003; Konieczny et al, 2008; Reznicek et al, 2007), the binding partners of the isoform specific sequences have so far not been reported. Previous studies have not elucidated the binding region of calmodulin on plectin 1a and the molecular mechanism of plectin - calmodulin interaction (Kostan et al, 2009). My PhD study firstly shows that CaM is the binding partner of the isoform specific sequence of plectin 1a, whereas the role of the N-terminal tail in the specific sub-cellular localization with hemidesmosomes is not clear yet.

#### 4.4. The role of calmodulin binding to plectin in the interaction with F-actin

Actin-binding capacity of plectin is common among all isoforms bearing different N-terminal sequences (Kostan et al, 2009). Interestingly, the muscle-specific isoforms of plectin containing additional exon 2 $\alpha$  and 3 $\alpha$  sequences in CH1 exhibit enhanced affinity to F-actin (Fuchs et al, 1999). In addition to its role in modulating the interaction between plectin 1a and integrin  $\beta$ 4, calmodulin was found to prevent plectin 1a binding to actin filaments (Kostan et al, 2009). To understand the mechanism of this regulation, the SAXS structure of the P1aABD/CaM complex was superimposed on the CH1 domain of  $\alpha$ -actinin ABD bound to F-actin (PDB: 3LUE) (Galkin et al, 2010) (RMSD: 0.54 Å over 98 equivalent C $\alpha$  atoms).

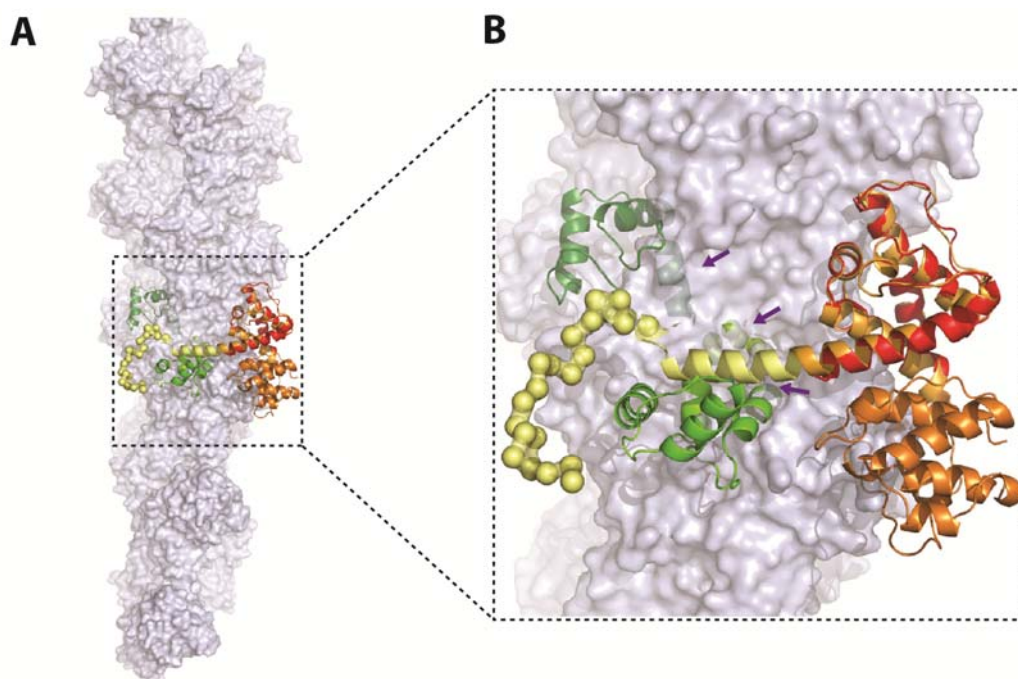


**Figure 4.2.** The SAXS structure of the P1aABD/CaM complex is superimposed to the CH1 domain of  $\alpha$ -actinin (red) that is bound to F-actin (light grey, PDB: 3LUE) (RMSD: 0.54 Å over 98 equivalent C $\alpha$  atoms). The steric clash between CaM and F-actin is indicated by purple arrows.

$\alpha$ -actinin ABD namely displays a closed conformation like plectin ABD (Franzot et al, 2005), with RMSD of 1.26 Å over 203 corresponding C $\alpha$  atoms. Besides the steric clash between CH2 of ABD and F-actin, already observed in  $\alpha$ -actinin F-actin study (Galkin et al, 2010), C-lobe of CaM in complex with P1aABD forms a steric clash with F-actin (**Figure 4.2**). While the actin-binding sites (ABS) of CH1, mapped to the first and the last  $\alpha$ -helix of the CH1 domain and to the first helix of CH2 (Bresnick et al, 1990; Levine et al, 1990), are not directly affected by CaM binding, the structural analysis shows that CaM binding inhibits the plectin ABD/F-actin interaction by limiting the accessibility of F-actin to ABD.

#### 4.5. Summary

During my PhD study, I have shed light on the structural basis of the hemidesmosome disassembly regulated by calcium-calmodulin. I would like to summarize major findings of my PhD study. Firstly, I solved the crystal and solution structures of plectin 1a actin-binding domain, which both show that the N-terminal tail of plectin 1a is disordered, while ABD adopts the classical closed conformation. Secondly, I solved the crystal structure of the P1aABD $_{\Delta 22}$ /CaM $_{NL}$  complex and the solution structure of the P1aABD/CaM complex. These results provide the first structural insights into the calmodulin binding to plectin 1a. The structures show that the N-terminal lobe of calmodulin binds to the N-terminal tail of plectin 1a. These findings were corroborated by isothermal titration calorimetry and chemical cross-linking combined with mass spectrometry analysis. Upon calmodulin binding to the N-terminal tail of plectin 1a, the disordered N-terminal tail adopts an  $\alpha$ -helical structure. Comparative structural analysis showed that calmodulin binds to plectin 1a in a non-canonical way, in extended conformation. Thirdly, I determined the crystal structure of the P1aABD $_{\Delta 22}$ / $\beta$ 4Fn12 complex and solution structure of the P1aABD/ $\beta$ 4Fn12 complex. In both structures N-terminal tail of plectin 1a is disordered and does not play a role for the interaction between plectin and integrin  $\beta$ 4. Finally, in order to elucidate at molecular level the dissociation mechanism of the P1aABD/ $\beta$ 4Fn12 complex driven by

calmodulin, the comprehensive displacement ITC study and structural analyses were carried out. Taken these results together, I suggest a model for the mechanism as depicted in **Figure 4.3**. At low cytosolic calcium concentrations plectin 1a – integrin  $\beta 4$  complex is maintained in hemidesmosomes. In this complex plectin 1a and in integrin  $\beta 4$  interact *via* an isoform independent interface also observed in plectin 1c - integrin  $\beta 4$ . The N-terminal extension of plectin 1a is disordered in the complex and is not involved in the interaction.

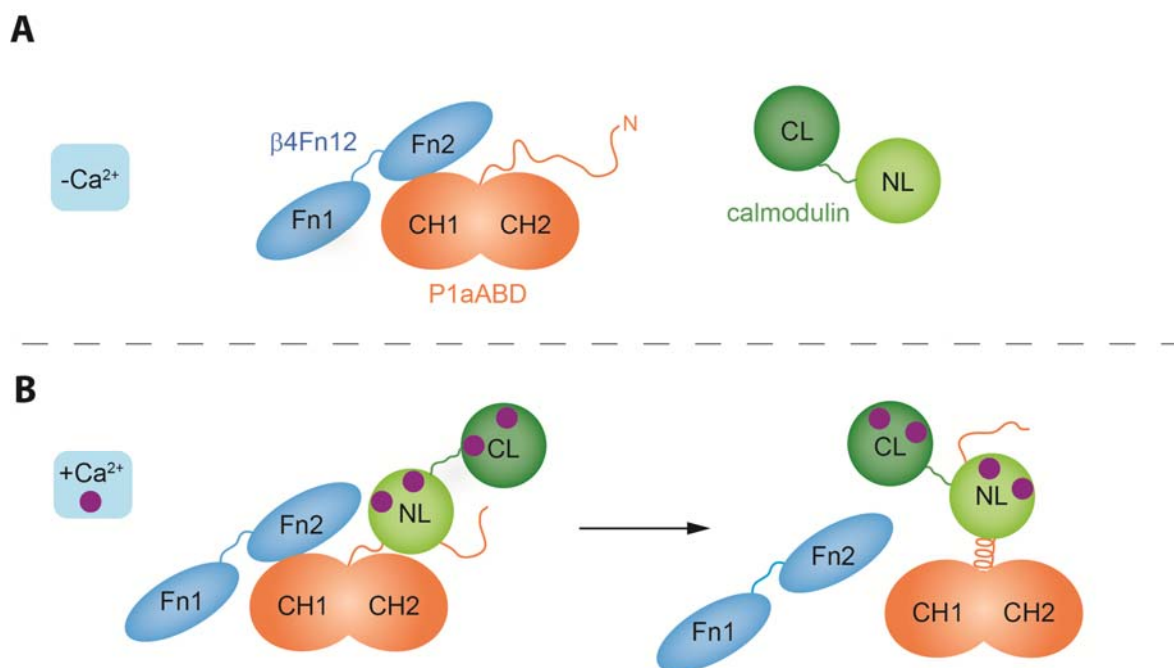


**Figure 4.3.** Model for the CaM driven disruption of the P1aABD/ $\beta 4$ Fn12 complex. **(A)** In low cytosolic calcium concentration, the P1aABD/ $\beta 4$ Fn12 complex is maintained in hemidesmosomes **(B)** When calcium concentration is increased in cytosol, calmodulin is activated by calcium binding, subsequently, it binds to the disordered N-terminal tail of plectin 1a which leads to its the folding into an  $\alpha$ -helix. The steric clash caused by calmodulin binding results in the dissociation of the P1aABD/ $\beta 4$ Fn12 complex.

Increased cytosolic calcium concentration causes the conformational change of calmodulin, rendering it capable of binding to the disordered N-terminal tail of plectin 1a. Calmodulin binds to the N-terminal tail of plectin 1a *via* its N-terminal lobe, which exhibits a higher affinity than the C-terminal lobe, due to a larger buried surface area with P1a than the C-terminal lobe. The N-terminal segment does not contribute to the complex formation with integrin  $\beta 4$ . Nevertheless, being intrinsically disordered is its essential property, which enables plectin 1a to interact with calmodulin. If it formed an  $\alpha$ -helix, it would generate a clash with integrin  $\beta 4$ , impeding the plectin-integrin  $\beta 4$  interaction. Upon calmodulin binding to plectin 1a, the N-terminal tail folds into an  $\alpha$ -helix, causing a steric clash that leads to the displacement of integrin  $\beta 4$ . When calmodulin binds to plectin 1a-integrin  $\beta 4$  complex, the binding affinity of calmodulin is reduced due to the competition with integrin  $\beta 4$ , and enthalpy and entropy changes are enlarged because of the replacement of integrin  $\beta 4$ . Calmodulin binding concomitantly leads also to inhibition of plectin 1a interaction with F-actin due to steric clash of calmodulin C-terminal lobe with actin filaments, suggesting its role in modulating competitive actin-binding of plectin and integrin. The hemidesmosome disassembly is also regulated by phosphorylation on several sites of integrin  $\beta 4$ ; phosphorylation on Ser1356 and Ser1364 by ERK 1/2 and p90RSK 1/2, and phosphorylation on Thr1736 by PKD1. My study deciphered only one mechanism contributing to the hemidesmosome disassembly. I think that a comprehensive study including several factors leading to the hemidesmosome disassembly should be accomplished to understand the interplay between the calmodulin binding to plectin 1a and the phosphorylation on integrin  $\beta 4$ .

## 5. MATERIALS AND METHODS

### 5.1. Molecular cloning

**Table 5.1.** Oligonucleotide primers used for PCR

Name	Sequence
Primers for plectin 1a	
PlecF1	5' ATAGATACATGTCTCAGCACCGGCTCCG
PlecF13	5' ATAGATCCATGGGCCTGGGTAGCAAGAGAAC
PlecF23	5' ATAGATCCATGGACAACCTCTACCTGGCTGTG
PlecF33	5' ATAGATCCATGGCCTCCGAGGGCAAGAAAGAT
PlecF38	5' ATAGATCCATGGATGAACGAGACCGTGTGCAG
PlecR263	5' ATACATGGATCCCTAGGGCATAGCATCGTACAGGGA
Primers for calmodulin	
CaM_F1	5' ATATATCCATGGAGGAGCAGATTGCAGAGTTCAAG
CaM_R1	5' ATATATGGATCCTCAGGCCATCATGGTCAGGAACTCC
Cam_F2	5' ATATATCCATGGACAGTGAGGAGGAGATCCGAGA
Cam_R2	5' ATATATGGATCCTCACTTTGCAGTCATCATCTGTACAAAC
Primers for integrin $\beta$ 4	
ITB4_F	5' CCAGGGGCCCCGCCATGGACC TGGGCGCCCCG
ITB4_R	5' GACCCGACGCGGTTAGCGTA GAACGTCATCGCTGTA
Primers for site-directed mutagenesis of plectin 1a	
LVDD-F	5' AGCTCAGAGGACAACGACTACCTGGCTGACCTCAGAGCCTCCGAG
LVDD-R	5' CTCGGAGGCTCTGAGGTCAGCCAGGTAGTCGTTGTCCTCTGAGCT

### 5.1.1. Plectin 1aABD

cDNA of mouse plectin 1aABD (UniProt accession number: Q9QXS1-3) encoding exon 1a-8 was amplified by polymerase chain reaction (PCR) using the oligonucleotide primers listed above (**Table 5.1**), generating plectin constructs with various lengths of the N-terminal tail encoding exon 1a, which are named P1aABD (1-263), P1aABD<sub>Δ11</sub> (12-263), P1aABD<sub>Δ22</sub> (23-263), P1aABD<sub>Δ32</sub> (33-263), and P1aABD<sub>Δ37</sub> (38-263). The amplified products were digested with *NcoI* (or *PstI* only for P1aABD construct) and *BamHI*, and were ligated into the expression vector pETM-14 containing the N-terminal his-tag and the 3C protease cleavage site, which had been digested with the same enzymes. The ligated products were transformed to *E.coli* DH5α competent cells.

### 5.1.2. Calmodulin

The full-length calmodulin construct was prepared as described previously (Kostan et al, 2009). Calmodulin constructs of N- and C-terminal lobes were prepared using the oligonucleotide primers listed above; CaMF-1 and CaMR-1 were used for the N-terminal domain of calmodulin (CaM<sub>NL</sub>) and CaMF-2 and CaMR-2 were used for the C-terminal domain of calmodulin (CaM<sub>CL</sub>) (**Table 5.1**). The amplified products were digested with *NcoI* and *BamHI*, and were ligated into the expression vector pETM-14, which had been digested with the same enzymes. The ligated product was transformed to *E.coli* DH5α competent cells.

### 5.1.3. Integrin β4

The integrin β4 construct termed β4Fn12 (1126-1355) comprises the first pair of fibronectin type III domains including a part of the connecting segment (CS) of integrin β4, designed by previous researchers (de Pereda et al, 2009; Niessen et al, 1997). The β4Fn12



construct was prepared using the cDNA of human integrin  $\beta 4$  (Rezniczek et al, 1998) and amplified using the oligonucleotide primers listed above (ITB4\_F and ITB4\_R) containing the complementary overhang for ligase independent cloning (**Table 5.1**). The PCR product was incubated for 30 min at 22 °C with T4 DNA polymerase in the presence of dATP, followed by heat treatment at 75 °C to inactivate the polymerase. The expression vector pETM-14LIC containing the N-terminal his-tag and the 3C protease cleavage site, designed for ligase independent cloning (pETM-14LIC), was digested with *BsaI* and the digested vector was treated for 30 min at 22 °C with T4 DNA polymerase in the presence of dTTP, followed by heat treatment at 75 °C to inactivate the polymerase. The insert and the vector were annealed at 22 °C for 30 min, and the annealed product was transformed to *E.coli* DH5 $\alpha$  competent cells.

#### 5.1.4. Site-directed mutagenesis of plectin 1aABD

The oligonucleotide primers were designed to mutate two hydrophobic residues (Leu25Asp and Val29Asp) in the N-terminal tail of plectin 1a. The PCR was carried out using the expression vector containing P1aABD (encoding exon 1a-8) and the mutagenesis oligonucleotide primers listed above. The amplified vector was incubated with *DpnI* at 37 °C for 1 h to digest the template plasmid, followed by the transformation to *E.coli* DH5 $\alpha$  competent cells.

## 5.2. Protein expression and purification

The expression vectors transformed to *E.coli* DH5 $\alpha$  competent cells were isolated and transformed to *E.coli* Rosetta2 (DE3) pLysS cells after checking nucleotide sequences. Cells harboring the different expression plasmids were grown at 37 °C in ZYP media until the OD 600 is reached to 0.6. Protein expression was induced by 0.2 mM isopropyl- $\beta$ -D-thiogalactopyranoside (IPTG), and cultures were grown for another 18 °C for 16 h. ZYP

media was used for the protein expression, which is supplemented with 0.5% glycerol, 2 mM MgSO<sub>4</sub> and the trace metal solution containing 50 μM FeCl<sub>3</sub>, 20 μM CaCl<sub>2</sub>, 10 μM MnCl<sub>3</sub>, 10 μM ZnSO<sub>4</sub>, 2 μM CoCl<sub>2</sub>, 2 μM CuCl<sub>2</sub>, 2 μM NiCl<sub>2</sub>, 2 μM Na<sub>2</sub>MoO<sub>4</sub>, 2 μM Na<sub>2</sub>SeO<sub>3</sub>, and 2 μM H<sub>3</sub>BO<sub>3</sub> (Studier, 2005). Cells were harvested by centrifugation and resuspended in the lysis buffer (20 mM Tris–HCl pH 7.5, 150 mM NaCl, and 0.1 mM EDTA). The resuspended cells were disrupted by sonication and centrifuged at 30,000*g* for 20 min at 4 °C.

Protein samples were introduced to a HisTrap HP column (GE Healthcare) equilibrated with the HisTrap buffer A containing 20 mM Tris pH 7.5, 0.5 M NaCl, and 0.01 mM EDTA and samples were eluted with the HisTrap buffer B (20 mM Tris pH 7.5, 0.5 M NaCl, and 0.5 M imidazole). Major fractions containing the desired proteins were pooled and dialyzed against the HisTrap buffer A, supplemented with 2 mM β-mercaptoethanol. The GST-3C protease cleavage was followed after the dialysis. The dialyzed samples were introduced again to HisTrap HP column (GE Healthcare). Unbound fractions were collected after second nickel-affinity chromatography, which were further purified using a Superdex 75 gel filtration column (GE Healthcare) and an in-line GSTrap HP column (GE Healthcare) in the SEC buffer (20 mM Tris pH 7.5, 150 mM NaCl, 0.1 mM EDTA, and 3% glycerol).

### 5.3. Thermal shift assay (thermofluor)

20 μM protein samples (13.5 μl) were mixed with 1.5 μl of 100 X Sypro Orange (Molecular Probes), which were added to 96-well PCR plate. The plates were sealed with Optical-Quality Sealing Tape (Bio-Rad) and heated in an iCycler iQ Real Time PCR Detection System (Bio-Rad) from 20 to 95 °C in increments of 1 °C. Fluorescence changes in the plates were measured at the wavelengths for excitation and emission were 490 and 575 nm, respectively (Ericsson et al, 2006).

#### 5.4. Determination of protein concentration

Extinction coefficients of protein samples were calculated by ProtParam tool on the ExPASy server (Gasteiger et al, 2003) and listed below (**Table 5.2**). The extinction coefficient of CaM<sub>NL</sub> was not able to calculate due to the absence of aromatic residues. Each protein concentration was measured by NanoDrop spectrophotometer (Thermo Scientific) at UV 280 nm or 205 nm (in the case of CaM<sub>NL</sub>).

**Table 5.2.** Extinction coefficients of proteins

Name	Extinction coefficient (M <sup>-1</sup> cm <sup>-1</sup> )	Abs 0.1% (=1 g/L)
Plectin 1a constructs		
P1aABD	32430	1.062
P1aABD <sub>Δ11</sub>	32430	1.115
P1aABD <sub>Δ22</sub>	32430	1.150
P1aABD <sub>Δ32</sub>	30940	1.145
P1aABD <sub>Δ37</sub>	30940	1.171
Calmodulin constructs		
CaM	2980	0.177
CaM <sub>NL</sub>	ND	ND
CaM <sub>CL</sub>	2980	0.371
Integrin β4 construct		
β4Fn12	41620	1.616

## 5.5. Protein crystallization

### 5.5.1. Crystallization and Structure Determination of the P1aABD<sub>Δ22</sub>

P1aABD<sub>Δ22</sub> (23-263) was prepared in the buffer containing 20 mM Tris pH 7.5, 150 mM NaCl. Crystals were grown by the sitting-drop method at 22 °C. The protein sample (10 mg/ml) was mixed with an equal volume of the crystallization solution containing 0.05 M potassium phosphate monobasic and 20% PEG 8000. Crystals were transferred to crystallization solution containing 20% glycerol and flash frozen in liquid nitrogen. Diffraction data were collected at the beamline ID14-4 in ESRF (Grenoble, France), integrated with XDS (Kabsch, 2010) and scaled with Scala in the CCP4 suite (Evans & Murshudov, 2013). The structure was solved by molecular replacement using Phaser (McCoy et al, 2007); plectin ABD (PDB: 1MB8) was used as a search model. Refinement was carried out using Phenix Refine (Afonine et al, 2012), alternating with model adjustment by Coot (Emsley & Cowtan, 2004). Data collection and final refinement statistics are summarized in **Table 1**.

### 5.5.2. Crystallization and structure determination of the P1aABD<sub>Δ22</sub>/CaM<sub>NL</sub> complex

P1aABD<sub>Δ22</sub> (23-262) was mixed with CaM<sub>NL</sub> in an equal molar ratio and the protein complex was eluted from a gel filtration column in the buffer containing 20 mM Tris pH 7.5, 150 mM NaCl, and 5 mM CaCl<sub>2</sub>. Crystals were grown by the hanging-drop vapor diffusion method at 4 °C. The concentrated protein solution (11 mg/ml) was mixed with an equal volume of the crystallization solution containing 0.1 M Bis-Tris pH 6.5, 0.2 M MgCl<sub>2</sub>, and 13% PEG 8000. Crystals were transferred to cryo-protectant containing 20% glycerol and flash frozen in liquid nitrogen. Diffraction data were collected at the beamline ID14-1 in ESRF (Grenoble, France), integrated with XDS (Kabsch, 2010) and scaled with Scala in CCP4 suite (Evans & Murshudov, 2013). The structure was solved by molecular replacement using

Phaser (McCoy et al, 2007); plectin ABD (PDB: 1MB8) was used as a search model. The initial model was constructed by Arp/wARP (Langer et al, 2008), and refinement was carried out using Phenix Refine (Afonine et al, 2012), alternating with model adjustment by Coot (Emsley & Cowtan, 2004). Data collection and final refinement statistics are summarized in **Table 5**.

### 5.5.3. Crystallization and structure determination of the P1aABD<sub>Δ22</sub>/β4Fn12 complex

P1aABD<sub>Δ22</sub> was mixed with β4Fn12 in an equal molar ratio and concentrated to 12 mg/ml for crystallization. Crystals of the protein complex were grown at 22 °C using vapor diffusion from hanging drop, consisted of equal volumes of the protein sample and the crystallization solution containing 20 mM HEPES pH 6.5, 150 mM Sodium formate, 7.5% PEG 5500 MME and 3% Sucrose. The obtained crystals were treated with several dehydration methods. Crystals were transferred to cryoprotectant containing 40% PEG550 MME and flash frozen in liquid nitrogen. Two data sets were collected at the beamline ID23-2 in ESRF and each data set was individually integrated by XDS, followed by merging and scaling with Aimless. The structure of the complex was solved by molecular replacement with Phaser by using plectin ABD (PDB: 1MB8) and integrin β4 fragment (PDB: 3F7Q) as search models. The refinement was performed alternately by Coot and Phenix Refine using strategies of rigid body and TLS (Krissinel & Henrick, 2007). Data collection and final refinement statistics are summarized in **Table 8**.

### 5.5.4. Crystal dehydration

Dehydration for crystals of the P1aABD<sub>Δ22</sub>/β4Fn12 complex was performed in house by following several methods shown in **Figure 5.1**. First, crystal dehydration was carried out

by transferring cover slips to reservoirs containing the crystallization solution with serial concentrations of PEG 550 MME; the concentration was increased to 40% in steps of 10% (equilibration time: 24h each). Second, crystals were transferred to another drop containing higher precipitant concentration (3% increment of PEG 5500 MME) and incubated for 2 h, which step was repeated until the concentration of PEG 5500 MME in drop is reached to either 15 % or 20 %.

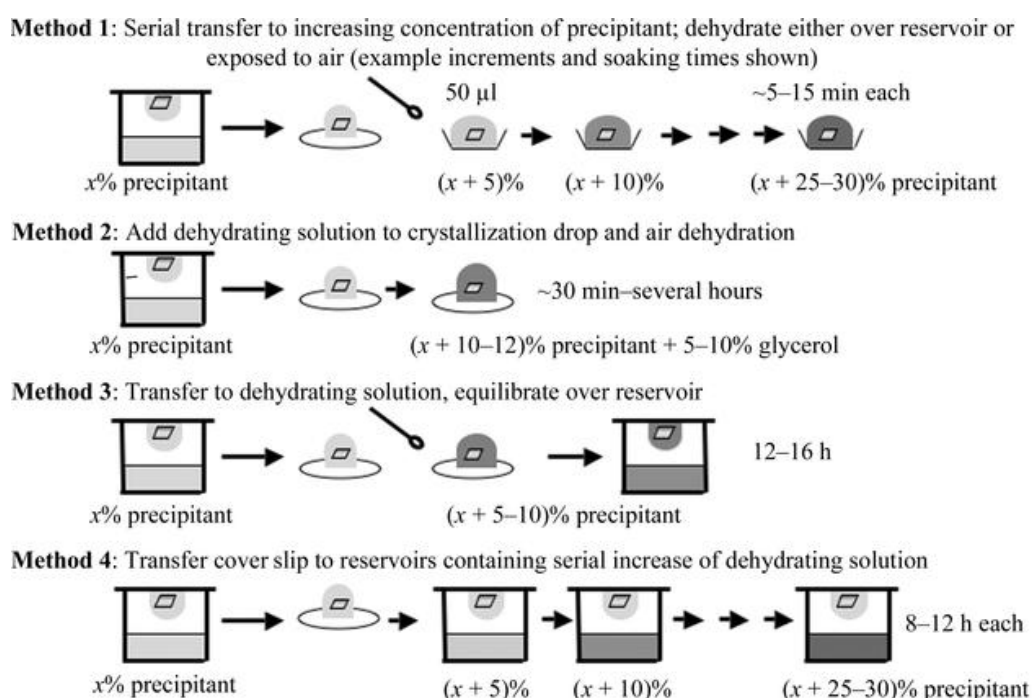


**Figure 5.1.** Crystal dehydration with several methods. The figure was reproduced from (Heras & Martin, 2005).

Crystal dehydration was also tried using humidity-control device (HC1b) at BM14 and ID23-2 beamlines at ESRF (Grenoble, France) (Sanchez-Weatherby et al, 2009). The crystals were transferred to mesh loops without redundant solvent and mounted on the goniometer. Relative humidity was decreased from 99 % to several relative humidity levels

such as 96%, 92%, and 86%. After dehydration, the crystals were flash frozen with liquid nitrogen for the diffraction experiments.

## 5.6. Isothermal Titration Calorimetry (ITC)

All protein samples were dialyzed against the buffer (20 mM HEPES pH 7.5, 150 mM NaCl and 5 mM  $\text{CaCl}_2$ ) overnight at 4°C. 200  $\mu\text{l}$  protein samples were injected in the sample cell and water was filled in the reference cell. 40  $\mu\text{l}$  of protein samples were inserted into the sample syringe for injection. ITC was performed at 25° or 30°C using iTC<sub>200</sub> Microcalorimeter (MicroCal). The experimental parameters were established like the followings: 22 times of total injections, 60 sec of initial delay, and 1000 rpm of stirring speed. Injection parameters are like the followings: 1.8  $\mu\text{l}$  of injection volume, 180 sec of spacing time, and 5 sec of filter period. Thermodynamic parameters of each interaction were obtained by fitting the single-set of binding model or competitive binding model using Origin 7. The heat of dilution into buffer was subtracted from each reaction or the final titration point was used to estimate the reference baseline.

## 5.7. Small angle X-ray scattering (SAXS)

### 5.7.1. SAXS analysis of P1aABD

SAXS experiments were performed at the SAXS beamline X33 at the Doris III storage ring, DESY (Hamburg, Germany) for the analyses of P1aABD (Blanchet et al, 2012). All protein samples were prepared in three different concentrations (3.0, 4.5, and 6.0 mg/ml) in the buffer containing 20 mM Tris pH 7.5, 150 mM NaCl, 5 mM  $\text{CaCl}_2$  and 1 mM DTT. Data reduction and processing were performed using the ATSAS program package. Structural parameters, zero-angle intensity ( $I(0)$ ) and radius of gyration ( $R_g$ ), from the Guinier plot

were calculated using PRIMUS (Konarev et al, 2003). The program GNOM was employed to generate the pair distribution curve for determining the maximum dimension ( $D_{\max}$ ) and to obtain  $R_g$  and  $I(0)$  values (Svergun, 1992). Three scattering data with different concentrations were merged since the concentration dependence was not detected by comparing  $I(0)$  and  $R_g$  values of three samples. EOM (Ensemble optimization method) was employed to assess the flexibility of the N-terminal tail (Bernado et al, 2007). The random pool of 10,000 conformers was generated using plectin ABD as a constraint. 50 models in the pool were selected to calculate the averaged scattering intensity, which was fitted to experimental data.  $R_g$  distributions against the frequency of occurrence were analyzed and compared between the pool and the selected ensemble. A random pool of 10,000 conformers was generated by EOM and the averaged scattering data from the selected ensemble was computed.

#### 5.7.2. SAXS analysis of the P1aABD/CaM complex

SAXS measurements of the P1aABD/CaM complex were performed at the SAXS beamline X33 at the Doris III storage ring, DESY (Hamburg, Germany) (Blanchet et al, 2012). The protein complex was purified by size-exclusion chromatography using a Superdex 75 16/60 column (GE Healthcare) after mixing P1aABD and CaM in an equal molar ratio in the presence of  $\text{Ca}^{2+}$ . Protein samples were prepared in three different concentrations (3.5, 6.0, and 8.4 mg/ml) in the SAXS buffer (20 mM Tris pH 7.5, 150 mM NaCl, 5 mM  $\text{CaCl}_2$ , and 1 mM DTT). The scattering data were processed as mentioned above. The P1aABD/CaM complex was analyzed by SAXS to model the missing parts from the crystal structure of the P1aABD $_{\Delta 22}$ /CaM $_{\text{NL}}$  complex. The concentration dependence was analyzed by analyzing structural parameters ( $I(0)$ ,  $R_g$ ) among samples. *Ab initio* shape determination was computed by the program DAMMIF (Franke & Svergun, 2009) based on the  $P(r)$  function generated by GNOM. Generated *ab initio* models were averaged using the program



DAMAVAR (Volkov & Svergun, 2003). Rigid-body modelling of the complex was performed by the program CORAL (Petoukhov et al, 2012) employing two subunits; one is the crystal structure of the P1aABD<sub>Δ22</sub>/CaM<sub>NL</sub> complex and another is the crystal structure of CaM<sub>CL</sub> (83-148, PDB: 3CLN) (Babu et al, 1988), which was combined with an *ab initio* approach to model missing residues (1-22 residues of P1aABD and 74-82 residues of CaM).

### 5.7.3. SAXS analysis of the P1aABD/ β4Fn12 complex

SAXS data of the P1aABD/β4Fn12 complex were collected at SWING beamline in the synchrotron SOLEIL (Saint-Aubin, France) (David & Perez, 2009). The collected data were integrated and processed using the program Foxtrot. The protein complex was prepared by mixing P1aABD and β4Fn12 in an equal molar ratio with three concentration series (2.4, 4.5, and 6.9 mg/ml) containing the SAXS buffer mentioned above lacking CaCl<sub>2</sub>. *Ab initio* structure determination of the P1aABD/β4Fn12 complex was performed in the same way as for the P1aABD/CaM complex. The program OLIGOMER was employed to calculate the volume fraction of the P1aABD/β4Fn12 complex in solution due to the expected polydispersity at the concentration used. Residues missing in the crystal structure of the P1aABD<sub>Δ22</sub>/β4Fn12 complex (1-37 residues of P1aABD and 1321-1355 residues of β4Fn12) were supplemented by the program BUNCH before generating form factors for OLIGOMER analyses.

### 5.8. Pull-down assay

All plectin constructs were prepared at 5 μM concentration in the buffer (20 mM Tris pH 7.5, 150 mM NaCl, and 0.05% Tween 20). 1 ml of plectin samples were mixed with 50 μl of CaM-Sepharose 4B beads (GE Healthcare) supplemented with either 5 mM CaCl<sub>2</sub> or 1 mM EDTA. The samples were incubated for 2 hours at room temperature, followed by

centrifugation at 3,000 x *g* for 2 min. Beads were washed with 1.5 ml of the buffer for three times and incubated with SDS-PAGE sample buffer at 95°C for 10 min to elute bound samples.

## 5.9. Cross-linking and mass spectrometry analyses

Cross-linking assays were performed using both one-step and two-step methods. For the one-step method, 2.5 mM cross-linkers (EDS/sNHS or DSS) were added to P1aABD/CaM complex (5 µM) prepared in the reaction buffer (0.1 M MES pH 6.5 and 0.5 M NaCl). For the two step cross-linking, 5 µM CaM was prepared in the reaction buffer and activated with 2.5 mM EDC (zero-length crosslinker) and 5 mM sulfo-NHS for 15 min, followed by adding 20 mM β-mercaptoethanol to quench the excessive EDC. P1aABD prepared in PBS was added to the activated CaM in an equal molar ratio and incubated at room temperature for 30 min.

Bands from SDS-PAGE of cross-linked samples were cut out, subjected to in-gel digestion using trypsin and analyzed by nano-HPLC-ESI-MS/MS using an UltiMate 3000 RSLCnano/LTQ-Orbitrap XL system (Thermo Fisher Scientific, Bremen, Germany) as described (Cristodero et al, 2013). In a first step data files from LC-MS/MS were analysed by standard database searches using the programs OMSSA (version 2.1.9) (Geer et al, 2004) as described (Kuhn et al, 2011) and MaxQuant (version 1.3.0.5) (Cox & Mann, 2008; Cox et al, 2011). All searches were done against the amino acid sequences for the recombinant proteins and for a set of common contaminants as provided with the distribution of the MaxQuant program with tryptic specificity allowing up to two missed cleavages. Oxidation of methionine and carbamidomethylation of cysteine were considered as variable and fixed modification, respectively. The mass tolerance for precursor and fragment ions was 5 ppm and 0.5 Da, respectively. In a second step, data were subjected to a rigorous search for the identification of cross-linked peptides using in-

house developed programs. For this purpose, theoretical proteolytic peptides of the recombinant proteins were computed with accurate masses and stored as an indexed table in a MySQL database. For each theoretical peptide the difference between its accurate mass and the precursor mass of each MS/MS spectrum was computed and queried against the indexed list of peptides indexed by mass using the same mass tolerance as in the first search. The cross-linker specificity was taken into account by retrieving only peptide pairs containing at least one suitable residue on each peptide.

For those peptide pairs matching a precursor mass, the list of theoretical fragment ions was generated and compared to the experimental list of fragment ions assigning a P-value according to the probability of finding at least the number of matched out of the number of theoretical masses by chance using the formula used for the Andromeda score (Cox et al, 2011) with minor changes as specified below. Neutral losses were considered for the precursor mass but not for fragment masses. Charges of fragment ions are allowed from +1 up to the charge of the precursor minus 1, but only if the charge state is in a plausible range compared to the expected charge state from the number of charged groups of the peptides. The expected charge state of fragments, computed as the number of basic sites estimated according to a simple scheme described by (Schlosser et al, 2007) (Arg, Lys, N-term: 1; His: 0.5) has to be met with a tolerance of +/- 1. In addition, analogously to the overall P-value of a cross-linked peptide spectrum match,  $P_{\alpha/\beta}$ -values were determined representing probabilities of finding at least the number of matched out of the number of theoretical fragment masses by chance for the  $\alpha$ - and  $\beta$ -peptide, respectively, of the cross-linked pair, carrying the mass of the complementary peptide at one linkage residue. From the resulting list of candidate peptide pairs only those with  $P_{\alpha/\beta}$ -values below 0.05 were considered as cross-linked peptide spectrum matches.

Quantitative analysis of peptide spectrum matches was performed based on the intensities of peptide features in the allPeptides.txt result file from the MaxQuant program. For this purpose the text file was stored in a MySQL table. For each peptide

spectrum match the sum of intensities was retrieved for features within the given precursor  $m/z$  tolerance and a retention time window  $\pm 1$  min around the retention time of the MS/MS spectrum.

## 6. REFERENCES

- Afonine PV, Grosse-Kunstleve RW, Echols N, Headd JJ, Moriarty NW, Mustyakimov M, Terwilliger TC, Urzhumtsev A, Zwart PH, Adams PD (2012) Towards automated crystallographic structure refinement with phenix.refine. *Acta crystallographica Section D, Biological crystallography* **68**: 352-367
- Andra K, Kornacker I, Jorgl A, Zorer M, Spazierer D, Fuchs P, Fischer I, Wiche G (2003) Plectin-isoform-specific rescue of hemidesmosomal defects in plectin (-/-) keratinocytes. *J Invest Dermatol* **120**: 189-197
- Andra K, Lassmann H, Bittner R, Shorny S, Fassler R, Propst F, Wiche G (1997) Targeted inactivation of plectin reveals essential function in maintaining the integrity of skin, muscle, and heart cytoarchitecture. *Genes Dev* **11**: 3143-3156
- Andra K, Nikolic B, Stocher M, Drenckhahn D, Wiche G (1998) Not just scaffolding: plectin regulates actin dynamics in cultured cells. *Genes Dev* **12**: 3442-3451
- Aumailley M, Bruckner-Tuderman L, Carter WG, Deutzmann R, Edgar D, Ekblom P, Engel J, Engvall E, Hohenester E, Jones JC, Kleinman HK, Marinkovich MP, Martin GR, Mayer U, Meneguzzi G, Miner JH, Miyazaki K, Patarroyo M, Paulsson M, Quaranta V, Sanes JR, Sasaki T, Sekiguchi K, Sorokin LM, Talts JF, Tryggvason K, Uitto J, Virtanen I, von der Mark K, Wewer UM, Yamada Y, Yurchenco PD (2005) A simplified laminin nomenclature. *Matrix Biol* **24**: 326-332
- Babu YS, Bugg CE, Cook WJ (1988) Structure of calmodulin refined at 2.2 Å resolution. *J Mol Biol* **204**: 191-204
- Babu YS, Sack JS, Greenhough TJ, Bugg CE, Means AR, Cook WJ (1985) Three-dimensional structure of calmodulin. *Nature* **315**: 37-40
- Baker SE, Hopkinson SB, Fitchmun M, Andreason GL, Frasier F, Plopper G, Quaranta V, Jones JC (1996) Laminin-5 and hemidesmosomes: role of the alpha 3 chain subunit in hemidesmosome stability and assembly. *J Cell Sci* **109 ( Pt 10)**: 2509-2520
- Baudoin C, Fantin L, Meneguzzi G (2005) Proteolytic processing of the laminin alpha3 G domain mediates assembly of hemidesmosomes but has no role on keratinocyte migration. *J Invest Dermatol* **125**: 883-888

Bernado P, Mylonas E, Petoukhov MV, Blackledge M, Svergun DI (2007) Structural characterization of flexible proteins using small-angle X-ray scattering. *Journal of the American Chemical Society* **129**: 5656-5664

Berridge MJ (1993) Inositol trisphosphate and calcium signalling. *Nature* **361**: 315-325

Blanchet CE, Zozulya AV, Kikhney AG, Franke D, Konarev PV, Shang WF, Klaering R, Robrahn B, Hermes C, Cipriani F, Svergun DI, Roessle M (2012) Instrumental setup for high-throughput small- and wide-angle solution scattering at the X33 beamline of EMBL Hamburg. *Journal of applied crystallography* **45**: 489-495

Borradori L, Koch PJ, Niessen CM, Erkeland S, van Leusden MR, Sonnenberg A (1997) The localization of bullous pemphigoid antigen 180 (BP180) in hemidesmosomes is mediated by its cytoplasmic domain and seems to be regulated by the beta4 integrin subunit. *J Cell Biol* **136**: 1333-1347

Borradori L, Sonnenberg A (1996) Hemidesmosomes: roles in adhesion, signaling and human diseases. *Current opinion in cell biology* **8**: 647-656

Borradori L, Sonnenberg A (1999) Structure and function of hemidesmosomes: more than simple adhesion complexes. *J Invest Dermatol* **112**: 411-418

Bresnick AR, Warren V, Condeelis J (1990) Identification of a short sequence essential for actin binding by Dictyostelium ABP-120. *J Biol Chem* **265**: 9236-9240

Campbell ID, Humphries MJ (2011) Integrin structure, activation, and interactions. *Cold Spring Harbor perspectives in biology* **3**

Campbell ID, Spitzfaden C (1994) Building proteins with fibronectin type III modules. *Structure* **2**: 333-337

Chavanas S, Pulkkinen L, Gache Y, Smith FJ, McLean WH, Uitto J, Ortonne JP, Meneguzzi G (1996) A homozygous nonsense mutation in the PLEC1 gene in patients with epidermolysis bullosa simplex with muscular dystrophy. *J Clin Invest* **98**: 2196-2200

Chen VB, Arendall WB, 3rd, Headd JJ, Keedy DA, Immormino RM, Kapral GJ, Murray LW, Richardson JS, Richardson DC (2010) MolProbity: all-atom structure validation for macromolecular crystallography. *Acta crystallographica Section D, Biological crystallography* **66**: 12-21

Clark EA, Brugge JS (1995) Integrins and signal transduction pathways: the road taken. *Science* **268**: 233-239

Cox J, Mann M (2008) MaxQuant enables high peptide identification rates, individualized p.p.b.-range mass accuracies and proteome-wide protein quantification. *Nature biotechnology* **26**: 1367-1372

Cox J, Neuhauser N, Michalski A, Scheltema RA, Olsen JV, Mann M (2011) Andromeda: a peptide search engine integrated into the MaxQuant environment. *Journal of proteome research* **10**: 1794-1805

Cozzini P, Fornabaio M, Marabotti A, Abraham DJ, Kellogg GE, Mozzarelli A (2004) Free energy of ligand binding to protein: evaluation of the contribution of water molecules by computational methods. *Current medicinal chemistry* **11**: 3093-3118

Cristodero M, Mani J, Oeljeklaus S, Aeberhard L, Hashimi H, Ramrath DJ, Lukes J, Warscheid B, Schneider A (2013) Mitochondrial translation factors of *Trypanosoma brucei*: Elongation factor-Tu has a unique subdomain that is essential for its function. *Molecular microbiology*

Crivici A, Ikura M (1995) Molecular and structural basis of target recognition by calmodulin. *Annu Rev Biophys Biomol Struct* **24**: 85-116

David G, Perez J (2009) Combined sampler robot and high-performance liquid chromatography: a fully automated system for biological small-angle X-ray scattering experiments at the Synchrotron SOLEIL SWING beamline. *Journal of applied crystallography* **42**: 892-900

de Pereda JM, Lillo MP, Sonnenberg A (2009) Structural basis of the interaction between integrin alpha6beta4 and plectin at the hemidesmosomes. *EMBO J* **28**: 1180-1190

de Pereda JM, Wiche G, Liddington RC (1999) Crystal structure of a tandem pair of fibronectin type III domains from the cytoplasmic tail of integrin alpha6beta4. *EMBO J* **18**: 4087-4095

Dixon TC, Meselson M, Guillemin J, Hanna PC (1999) Anthrax. *The New England journal of medicine* **341**: 815-826

Djinovic Carugo K, Banuelos S, Saraste M (1997) Crystal structure of a calponin homology domain. *Nat Struct Biol* **4**: 175-179

Drum CL, Yan SZ, Bard J, Shen YQ, Lu D, Soelaiman S, Grabarek Z, Bohm A, Tang WJ (2002) Structural basis for the activation of anthrax adenyl cyclase exotoxin by calmodulin. *Nature* **415**: 396-402

Dunitz JD (1994) The entropic cost of bound water in crystals and biomolecules. *Science* **264**: 670

Dyson HJ, Wright PE (2005) Intrinsically unstructured proteins and their functions. *Nature reviews Molecular cell biology* **6**: 197-208

Eady RA, Dunnill MG (1994) Epidermolysis bullosa: hereditary skin fragility diseases as paradigms in cell biology. *Arch Dermatol Res* **287**: 2-9

Elshorst B, Hennig M, Forsterling H, Diener A, Maurer M, Schulte P, Schwalbe H, Griesinger C, Krebs J, Schmid H, Vorherr T, Carafoli E (1999) NMR solution structure of a complex of calmodulin with a binding peptide of the Ca<sup>2+</sup> pump. *Biochemistry* **38**: 12320-12332

Emsley P, Cowtan K (2004) Coot: model-building tools for molecular graphics. *Acta crystallographica Section D, Biological crystallography* **60**: 2126-2132

Ericsson UB, Hallberg BM, Detitta GT, Dekker N, Nordlund P (2006) Thermofluor-based high-throughput stability optimization of proteins for structural studies. *Analytical biochemistry* **357**: 289-298

Evans PR, Murshudov GN (2013) How good are my data and what is the resolution? *Acta crystallographica Section D, Biological crystallography* **69**: 1204-1214

Farquhar MG, Palade GE (1963) Junctional complexes in various epithelia. *J Cell Biol* **17**: 375-412

Fine JD, Bauer EA, Briggaman RA, Carter DM, Eady RA, Esterly NB, Holbrook KA, Hurwitz S, Johnson L, Lin A, et al. (1991) Revised clinical and laboratory criteria for subtypes of inherited epidermolysis bullosa. A consensus report by the Subcommittee on Diagnosis and Classification of the National Epidermolysis Bullosa Registry. *Journal of the American Academy of Dermatology* **24**: 119-135

Foisner R, Leichtfried FE, Herrmann H, Small JV, Lawson D, Wiche G (1988) Cytoskeleton-associated plectin: in situ localization, in vitro reconstitution, and binding to immobilized intermediate filament proteins. *J Cell Biol* **106**: 723-733



Foisner R, Wiche G (1987) Structure and hydrodynamic properties of plectin molecules. *J Mol Biol* **198**: 515-531

Franke D, Svergun DI (2009) DAMMIF, a program for rapid ab-initio shape determination in small-angle scattering. *Journal of applied crystallography* **42**: 342-346

Franzot G, Sjoblom B, Gautel M, Djinojic Carugo K (2005) The crystal structure of the actin binding domain from alpha-actinin in its closed conformation: structural insight into phospholipid regulation of alpha-actinin. *J Mol Biol* **348**: 151-165

Frijns E, Kuikman I, Litjens S, Raspe M, Jalink K, Ports M, Wilhelmsen K, Sonnenberg A (2012) Phosphorylation of threonine 1736 in the C-terminal tail of integrin beta4 contributes to hemidesmosome disassembly. *Mol Biol Cell* **23**: 1475-1485

Frijns E, Sachs N, Kreft M, Wilhelmsen K, Sonnenberg A (2010) EGF-induced MAPK signaling inhibits hemidesmosome formation through phosphorylation of the integrin {beta}4. *J Biol Chem* **285**: 37650-37662

Fuchs P, Zorer M, Rezniczek GA, Spazierer D, Oehler S, Castanon MJ, Hauptmann R, Wiche G (1999) Unusual 5' transcript complexity of plectin isoforms: novel tissue-specific exons modulate actin binding activity. *Hum Mol Genet* **8**: 2461-2472

Galione A, White A (1994) Ca<sup>2+</sup> release induced by cyclic ADP-ribose. *Trends Cell Biol* **4**: 431-436

Galkin VE, Orlova A, Salmazo A, Djinojic-Carugo K, Egelman EH (2010) Opening of tandem calponin homology domains regulates their affinity for F-actin. *Nature structural & molecular biology* **17**: 614-616

Garcia-Alvarez B, Bobkov A, Sonnenberg A, de Pereda JM (2003) Structural and functional analysis of the actin binding domain of plectin suggests alternative mechanisms for binding to F-actin and integrin beta4. *Structure* **11**: 615-625

Gasteiger E, Gattiker A, Hoogland C, Ivanyi I, Appel RD, Bairoch A (2003) ExPASy: the proteomics server for in-depth protein knowledge and analysis. *Nucleic acids research* **31**: 3784-3788

Geer LY, Markey SP, Kowalak JA, Wagner L, Xu M, Maynard DM, Yang X, Shi W, Bryant SH (2004) Open mass spectrometry search algorithm. *Journal of proteome research* **3**: 958-964

Geerts D, Fontao L, Nievers MG, Schaapveld RQ, Purkis PE, Wheeler GN, Lane EB, Leigh IM, Sonnenberg A (1999) Binding of integrin alpha6beta4 to plectin prevents plectin association with F-actin but does not interfere with intermediate filament binding. *J Cell Biol* **147**: 417-434

Georges-Labouesse E, Messaddeq N, Yehia G, Cadalbert L, Dierich A, Le Meur M (1996) Absence of integrin alpha 6 leads to epidermolysis bullosa and neonatal death in mice. *Nat Genet* **13**: 370-373

Giudice GJ, Emery DJ, Diaz LA (1992) Cloning and primary structural analysis of the bullous pemphigoid autoantigen BP180. *J Invest Dermatol* **99**: 243-250

Goldfinger LE, Hopkinson SB, deHart GW, Collawn S, Couchman JR, Jones JC (1999) The alpha3 laminin subunit, alpha6beta4 and alpha3beta1 integrin coordinately regulate wound healing in cultured epithelial cells and in the skin. *J Cell Sci* **112 ( Pt 16)**: 2615-2629

Green KJ, Jones JC (1996) Desmosomes and hemidesmosomes: structure and function of molecular components. *FASEB journal : official publication of the Federation of American Societies for Experimental Biology* **10**: 871-881

Heidorn DB, Trewella J (1988) Comparison of the crystal and solution structures of calmodulin and troponin C. *Biochemistry* **27**: 909-915

Hemler ME, Crouse C, Sonnenberg A (1989) Association of the VLA alpha 6 subunit with a novel protein. A possible alternative to the common VLA beta 1 subunit on certain cell lines. *J Biol Chem* **264**: 6529-6535

Heras B, Martin JL (2005) Post-crystallization treatments for improving diffraction quality of protein crystals. *Acta crystallographica Section D, Biological crystallography* **61**: 1173-1180

Hoeflich KP, Ikura M (2002) Calmodulin in action: diversity in target recognition and activation mechanisms. *Cell* **108**: 739-742

Hynes RO (2002) Integrins: bidirectional, allosteric signaling machines. *Cell* **110**: 673-687

Ikura M, Clore GM, Gronenborn AM, Zhu G, Klee CB, Bax A (1992) Solution structure of a calmodulin-target peptide complex by multidimensional NMR. *Science* **256**: 632-638

Ishida T, Kinoshita K (2007) PrDOS: prediction of disordered protein regions from amino acid sequence. *Nucleic acids research* **35**: W460-464

Jefferson JJ, Ciatto C, Shapiro L, Liem RK (2007) Structural analysis of the plakin domain of bullous pemphigoid antigen1 (BPAG1) suggests that plakins are members of the spectrin superfamily. *J Mol Biol* **366**: 244-257

Jones JC, Asmuth J, Baker SE, Langhofer M, Roth SI, Hopkinson SB (1994) Hemidesmosomes: extracellular matrix/intermediate filament connectors. *Exp Cell Res* **213**: 1-11

Jones JC, Hopkinson SB, Goldfinger LE (1998) Structure and assembly of hemidesmosomes. *Bioessays* **20**: 488-494

Kabsch W (2010) Xds. *Acta crystallographica Section D, Biological crystallography* **66**: 125-132

Kataoka M, Head JF, Seaton BA, Engelman DM (1989) Melittin binding causes a large calcium-dependent conformational change in calmodulin. *Proc Natl Acad Sci U S A* **86**: 6944-6948

Klevit RE, Blumenthal DK, Wemmer DE, Krebs EG (1985) Interaction of calmodulin and a calmodulin-binding peptide from myosin light chain kinase: major spectral changes in both occur as the result of complex formation. *Biochemistry* **24**: 8152-8157

Konarev PV, Volkov VV, Sokolova AV, Koch MHJ, Svergun DI (2003) PRIMUS: a Windows PC-based system for small-angle scattering data analysis. *Journal of applied crystallography* **36**: 1277-1282

Konieczny P, Fuchs P, Reipert S, Kunz WS, Zeold A, Fischer I, Paulin D, Schroder R, Wiche G (2008) Myofiber integrity depends on desmin network targeting to Z-disks and costameres via distinct plectin isoforms. *J Cell Biol* **181**: 667-681

Koss-Harnes D, Hoyheim B, Anton-Lamprecht I, Gjesti A, Jorgensen RS, Jahnsen FL, Olaisen B, Wiche G, Gedde-Dahl T, Jr. (2002) A site-specific plectin mutation causes dominant epidermolysis bullosa simplex Ogna: two identical de novo mutations. *J Invest Dermatol* **118**: 87-93

Koss-Harnes D, Jahnsen FL, Wiche G, Soyland E, Brandtzaeg P, Gedde-Dahl T, Jr. (1997) Plectin abnormality in epidermolysis bullosa simplex Ogna: non-responsiveness of basal keratinocytes to some anti-rat plectin antibodies. *Exp Dermatol* **6**: 41-48

Kostan J, Gregor M, Walko G, Wiche G (2009) Plectin isoform-dependent regulation of keratin-integrin alpha6beta4 anchorage via Ca<sup>2+</sup>/calmodulin. *J Biol Chem* **284**: 18525-18536

Koster J, Geerts D, Favre B, Borradori L, Sonnenberg A (2003) Analysis of the interactions between BP180, BP230, plectin and the integrin alpha6beta4 important for hemidesmosome assembly. *J Cell Sci* **116**: 387-399

Koster J, Kuikman I, Kreft M, Sonnenberg A (2001) Two different mutations in the cytoplasmic domain of the integrin beta 4 subunit in nonlethal forms of epidermolysis bullosa prevent interaction of beta 4 with plectin. *J Invest Dermatol* **117**: 1405-1411

Koster J, van Wilpe S, Kuikman I, Litjens SH, Sonnenberg A (2004) Role of binding of plectin to the integrin beta4 subunit in the assembly of hemidesmosomes. *Mol Biol Cell* **15**: 1211-1223

Krissinel E, Henrick K (2007) Inference of macromolecular assemblies from crystalline state. *J Mol Biol* **372**: 774-797

Kuboniwa H, Tjandra N, Grzesiek S, Ren H, Klee CB, Bax A (1995) Solution structure of calcium-free calmodulin. *Nat Struct Biol* **2**: 768-776

Kuhn P, Weiche B, Sturm L, Sommer E, Drepper F, Warscheid B, Sourjik V, Koch HG (2011) The bacterial SRP receptor, SecA and the ribosome use overlapping binding sites on the SecY translocon. *Traffic* **12**: 563-578

Langer G, Cohen SX, Lamzin VS, Perrakis A (2008) Automated macromolecular model building for X-ray crystallography using ARP/wARP version 7. *Nature protocols* **3**: 1171-1179

Lau TL, Kim C, Ginsberg MH, Ulmer TS (2009) The structure of the integrin alphaIIb beta3 transmembrane complex explains integrin transmembrane signalling. *EMBO J* **28**: 1351-1361

Leahy DJ, Hendrickson WA, Aukhil I, Erickson HP (1992) Structure of a fibronectin type III domain from tenascin phased by MAD analysis of the selenomethionyl protein. *Science* **258**: 987-991

Lee EC, Lotz MM, Steele GD, Jr., Mercurio AM (1992) The integrin alpha 6 beta 4 is a laminin receptor. *J Cell Biol* **117**: 671-678

Levine BA, Moir AJ, Patchell VB, Perry SV (1990) The interaction of actin with dystrophin. *FEBS Lett* **263**: 159-162

Litjens SH, de Pereda JM, Sonnenberg A (2006) Current insights into the formation and breakdown of hemidesmosomes. *Trends Cell Biol* **16**: 376-383

McCoy AJ, Grosse-Kunstleve RW, Adams PD, Winn MD, Storoni LC, Read RJ (2007) Phaser crystallographic software. *Journal of applied crystallography* **40**: 658-674

Meador WE, Means AR, Quirocho FA (1992) Target enzyme recognition by calmodulin: 2.4 Å structure of a calmodulin-peptide complex. *Science* **257**: 1251-1255

Moore CA, Keep NH, Kendrick-Jones J (2000) Structure of the utrophin actin-binding domain bound to F-actin reveals binding by an induced fit mechanism. *J Mol Biol* **297**: 465-480

Moser M, Legate KR, Zent R, Fassler R (2009) The tail of integrins, talin, and kindlins. *Science* **324**: 895-899

Niessen CM, Hulsman EH, Oomen LC, Kuikman I, Sonnenberg A (1997) A minimal region on the integrin beta4 subunit that is critical to its localization in hemidesmosomes regulates the distribution of HD1/plectin in COS-7 cells. *J Cell Sci* **110 ( Pt 15)**: 1705-1716

Nikolic B, Mac Nulty E, Mir B, Wiche G (1996) Basic amino acid residue cluster within nuclear targeting sequence motif is essential for cytoplasmic plectin-vimentin network junctions. *J Cell Biol* **134**: 1455-1467

Ortega E, Buey RM, Sonnenberg A, de Pereda JM (2011) The structure of the plakin domain of plectin reveals a non-canonical SH3 domain interacting with its fourth spectrin repeat. *J Biol Chem* **286**: 12429-12438

Pacifici R, Basilico C, Roman J, Zutter MM, Santoro SA, McCracken R (1992) Collagen-induced release of interleukin 1 from human blood mononuclear cells. Potentiation by fibronectin binding to the alpha 5 beta 1 integrin. *J Clin Invest* **89**: 61-67

Petoukhov MV, Franke D, Shkumatov AV, Tria G, Kikhney AG, Gajda M, Gorba C, Mertens HDT, Konarev PV, Svergun DI (2012) New developments in the ATSAS program package for small-angle scattering data analysis. *Journal of applied crystallography* **45**: 342-350

Petrich BG, Fogelstrand P, Partridge AW, Yousefi N, Ablooglu AJ, Shattil SJ, Ginsberg MH (2007) The antithrombotic potential of selective blockade of talin-dependent integrin alpha IIb beta 3 (platelet GPIIb-IIIa) activation. *J Clin Invest* **117**: 2250-2259

Potter JD, Strang-Brown P, Walker PL, Iida S (1983) Ca<sup>2+</sup> binding to calmodulin. *Methods in enzymology* **102**: 135-143

Rabinovitz I, Tsomo L, Mercurio AM (2004) Protein kinase C- $\alpha$  phosphorylation of specific serines in the connecting segment of the  $\beta$ 4 integrin regulates the dynamics of type II hemidesmosomes. *Mol Cell Biol* **24**: 4351-4360

Reipert S, Steinbock F, Fischer I, Bittner RE, Zeold A, Wiche G (1999) Association of mitochondria with plectin and desmin intermediate filaments in striated muscle. *Exp Cell Res* **252**: 479-491

Rezniczek GA, Abrahamsberg C, Fuchs P, Spazierer D, Wiche G (2003) Plectin 5'-transcript diversity: short alternative sequences determine stability of gene products, initiation of translation and subcellular localization of isoforms. *Hum Mol Genet* **12**: 3181-3194

Rezniczek GA, de Pereda JM, Reipert S, Wiche G (1998) Linking integrin  $\alpha$ 6 $\beta$ 4-based cell adhesion to the intermediate filament cytoskeleton: direct interaction between the  $\beta$ 4 subunit and plectin at multiple molecular sites. *J Cell Biol* **141**: 209-225

Rezniczek GA, Konieczny P, Nikolic B, Reipert S, Schneller D, Abrahamsberg C, Davies KE, Winder SJ, Wiche G (2007) Plectin 1f scaffolding at the sarcolemma of dystrophic (mdx) muscle fibers through multiple interactions with beta-dystroglycan. *J Cell Biol* **176**: 965-977

Rezniczek GA, Walko G, Wiche G (2010) Plectin gene defects lead to various forms of epidermolysis bullosa simplex. *Dermatologic clinics* **28**: 33-41

Rhoads AR, Friedberg F (1997) Sequence motifs for calmodulin recognition. *FASEB journal : official publication of the Federation of American Societies for Experimental Biology* **11**: 331-340

Rodriguez-Castaneda F, Maestre-Martinez M, Coudeville N, Dimova K, Junge H, Lipstein N, Lee D, Becker S, Brose N, Jahn O, Carlomagno T, Griesinger C (2010) Modular architecture of Munc13/calmodulin complexes: dual regulation by Ca<sup>2+</sup> and possible function in short-term synaptic plasticity. *EMBO J* **29**: 680-691

Ruoslahti E, Pierschbacher MD (1987) New perspectives in cell adhesion: RGD and integrins. *Science* **238**: 491-497

Sanchez-Weatherby J, Bowler MW, Huet J, Gobbo A, Felisaz F, Lavault B, Moya R, Kadlec J, Ravelli RB, Cipriani F (2009) Improving diffraction by humidity control: a novel device compatible with X-ray beamlines. *Acta crystallographica Section D, Biological crystallography* **65**: 1237-1246

Schlosser A, Vanselow JT, Kramer A (2007) Comprehensive phosphorylation site analysis of individual phosphoproteins applying scoring schemes for MS/MS data. *Analytical chemistry* **79**: 7439-7449

Schumacher MA, Rivard AF, Bachinger HP, Adelman JP (2001) Structure of the gating domain of a Ca<sup>2+</sup>-activated K<sup>+</sup> channel complexed with Ca<sup>2+</sup>/calmodulin. *Nature* **410**: 1120-1124

Schwartz MA, Schaller MD, Ginsberg MH (1995) Integrins: emerging paradigms of signal transduction. *Annual review of cell and developmental biology* **11**: 549-599

Sevcik J, Urbanikova L, Kost'an J, Janda L, Wiche G (2004) Actin-binding domain of mouse plectin. Crystal structure and binding to vimentin. *Eur J Biochem* **271**: 1873-1884

Shattil SJ, Kim C, Ginsberg MH (2010) The final steps of integrin activation: the end game. *Nature reviews Molecular cell biology* **11**: 288-300

Sigurskjold BW (2000) Exact analysis of competition ligand binding by displacement isothermal titration calorimetry. *Analytical biochemistry* **277**: 260-266

Sonnenberg A, Calafat J, Janssen H, Daams H, van der Raaij-Helmer LM, Falcioni R, Kennel SJ, Aplin JD, Baker J, Loizidou M, et al. (1991) Integrin alpha 6/beta 4 complex is located in hemidesmosomes, suggesting a major role in epidermal cell-basement membrane adhesion. *J Cell Biol* **113**: 907-917

Stanley JR, Tanaka T, Mueller S, Klaus-Kovtun V, Roop D (1988) Isolation of complementary DNA for bullous pemphigoid antigen by use of patients' autoantibodies. *J Clin Invest* **82**: 1864-1870

Stepp MA, Spurr-Michaud S, Tisdale A, Elwell J, Gipson IK (1990) Alpha 6 beta 4 integrin heterodimer is a component of hemidesmosomes. *Proc Natl Acad Sci U S A* **87**: 8970-8974

Studier FW (2005) Protein production by auto-induction in high density shaking cultures. *Protein expression and purification* **41**: 207-234

Suzuki S, Naitoh Y (1990) Amino acid sequence of a novel integrin beta 4 subunit and primary expression of the mRNA in epithelial cells. *EMBO J* **9**: 757-763

Svergun D (1992) Determination of the regularization parameter in indirect-transform methods using perceptual criteria. *Journal of applied crystallography* **25**: 495-503

Svergun D, Barberato C, Koch MHJ (1995) CRY SOL - A program to evaluate x-ray solution scattering of biological macromolecules from atomic coordinates. *Journal of applied crystallography* **28**: 768-773

Tadokoro S, Shattil SJ, Eto K, Tai V, Liddington RC, de Pereda JM, Ginsberg MH, Calderwood DA (2003) Talin binding to integrin beta tails: a final common step in integrin activation. *Science* **302**: 103-106

Tamura RN, Rozzo C, Starr L, Chambers J, Reichardt LF, Cooper HM, Quaranta V (1990) Epithelial integrin alpha 6 beta 4: complete primary structure of alpha 6 and variant forms of beta 4. *J Cell Biol* **111**: 1593-1604

Vetter SW, Leclerc E (2003) Novel aspects of calmodulin target recognition and activation. *Eur J Biochem* **270**: 404-414

Vidal F, Aberdam D, Miquel C, Christiano AM, Pulkkinen L, Uitto J, Ortonne JP, Meneguzzi G (1995) Integrin beta 4 mutations associated with junctional epidermolysis bullosa with pyloric atresia. *Nat Genet* **10**: 229-234

Volkov VV, Svergun DI (2003) Uniqueness of ab initio shape determination in small-angle scattering. *Journal of applied crystallography* **36**: 860-864

Walko G, Vukasinovic N, Gross K, Fischer I, Sibitz S, Fuchs P, Reipert S, Jungwirth U, Berger W, Salzer U, Carugo O, Castanon MJ, Wiche G (2011) Targeted proteolysis of plectin isoform 1a accounts for hemidesmosome dysfunction in mice mimicking the dominant skin blistering disease EBS-Ogna. *PLoS genetics* **7**: e1002396

Wallace AC, Laskowski RA, Thornton JM (1995) LIGPLOT: a program to generate schematic diagrams of protein-ligand interactions. *Protein engineering* **8**: 127-134

Way M, Pope B, Weeds AG (1992) Are the conserved sequences in segment 1 of gelsolin important for binding actin? *J Cell Biol* **116**: 1135-1143



Wegener KL, Partridge AW, Han J, Pickford AR, Liddington RC, Ginsberg MH, Campbell ID (2007) Structural basis of integrin activation by talin. *Cell* **128**: 171-182

Wiche G, Baker MA (1982) Cytoplasmic network arrays demonstrated by immunolocalization using antibodies to a high molecular weight protein present in cytoskeletal preparations from cultured cells. *Exp Cell Res* **138**: 15-29

Wiche G, Herrmann H, Leichtfried F, Pytela R (1982) Plectin: a high-molecular-weight cytoskeletal polypeptide component that copurifies with intermediate filaments of the vimentin type. *Cold Spring Harbor symposia on quantitative biology* **46 Pt 1**: 475-482

Wilhelmsen K, Litjens SH, Kuikman I, Margadant C, van Rheenen J, Sonnenberg A (2007) Serine phosphorylation of the integrin beta4 subunit is necessary for epidermal growth factor receptor induced hemidesmosome disruption. *Mol Biol Cell* **18**: 3512-3522

Xiong JP, Stehle T, Diefenbach B, Zhang R, Dunker R, Scott DL, Joachimiak A, Goodman SL, Arnaout MA (2001) Crystal structure of the extracellular segment of integrin alpha Vbeta3. *Science* **294**: 339-345

Xiong JP, Stehle T, Goodman SL, Arnaout MA (2003) New insights into the structural basis of integrin activation. *Blood* **102**: 1155-1159

Xiong JP, Stehle T, Zhang R, Joachimiak A, Frech M, Goodman SL, Arnaout MA (2002) Crystal structure of the extracellular segment of integrin alpha Vbeta3 in complex with an Arg-Gly-Asp ligand. *Science* **296**: 151-155

Yazawa M, Ikura M, Hikichi K, Ying L, Yagi K (1987) Communication between two globular domains of calmodulin in the presence of mastoparan or caldesmon fragment. Ca<sup>2+</sup> binding and 1H NMR. *J Biol Chem* **262**: 10951-10954

## CURRICULUM VITAE

# JAE-GEUN (JAKE) SONG

Max F. Perutz Laboratories, University of Vienna

Campus Vienna Biocenter 5, 1030, Vienna, Austria

[jaegeun.song@univie.ac.at](mailto:jaegeun.song@univie.ac.at)

## PERSONAL

---

Jae-Geun Song (called Jake Song)

Born in Seoul, 05 May 1982 / Married, one child

## EDUCATION

---

**B.S/M.S** Sungkyunkwan University (Dept. of Genetic Engineering, with honor), South Korea

2001-2009 Thesis title: Unique substrate spectrum and enhanced processivity of *Nanoarchaeum equitans* Family B DNA Polymerase / Supervisor: Prof. Suk-Tae Kwon

**Ph.D** MFPL, University of Vienna (Dept. of Structural and Computational Biology), Austria

2010- Expected to complete the thesis in Mar 2014/Supervisor: Prof. Kristina Djinovic-Carugo

## COURSES

---

DGK-AK1 Workshop: Diffraction Data Collection Using Synchrotron Radiation, BESSY II, Berlin, Germany (7-9 July 2011)

45<sup>th</sup> International School of Crystallography, Erice, Italy (31 May-10 June, 2012)

## SEMINAR PRESENTATION

---

14<sup>th</sup> Heart of Europe Bio-Crystallography meeting, Zagan, Poland, “Structural and functional analysis of the interaction between calmodulin and plectin isoform 1a” (30 Sep 2011)

## RESEARCH EXPERIENCE

---

Molecular biology and biochemistry

Molecular cloning, protein expression and purification with a variety of chromatographic techniques, mutagenesis (site-directed, random, and chimera) cross-linking assay

Biophysics

ITC, CD spectroscopy, Dynamic Light Scattering, SEC-MALLS, Thermofluor

X-ray Crystallography

Protein crystallization, seeding, limited proteolysis, crystal dehydration, data processing and structure determination, data collection by synchrotron radiation at ESRF, Swiss Light Source and Diamond Light Source, software skill (CCP4, PHENIX, XDS, Coot, Pymol)

Small angle X-ray scattering

Data collection and processing, data analyses by Guinier plots and P(r) curves, *ab initio* and rigid-body model generation, model validation, averaging, and alignment

## STRUCTURES

---

Crystal structures of the CaM(N-lobe)/plectinABD complex (1.8 Å) and the plectinABD/integrin  $\beta 4$  complex (4.0 Å) by MR (planned to submit to PDB in Mar 2014)

SAXS structures of the CaM/PlectinABD complex and the plectinABD/Integrin b4 complex (*ab initio* and rigid body models)

## PUBLICATIONS

---

**Song JG**, Kostan J, de Almeida Ribeiro E, Grishkovskaya I, Djinovic-Carugo K, (2014), Structural and functional analyses for the disassembly of hemidesmosomes regulated by calcium-calmodulin, manuscript in preparation

Duff RM, Tay V, Hackman P, Ravenscroft G, McLean C, Kennedy P, Steinbach A, Schöffler W, van der Ven PF, Fürst DO, **Song J**, Djinović-Carugo K, Penttilä S, Raheem O, Reardon K, Malandrini A, Gambelli S, Villanova M, Nowak KJ, Williams DR, Landers JE, Brown RH Jr, Udd B, Laing NG, (2011), Mutations in the N-terminal actin-binding domain of filamin C cause a distal myopathy. *Am J Hum Genet.*, Jun 10;88(6):729-40 PMID: 21620354

**Song JG**, Kil EJ, Cho SS, Kim IH, Kwon ST, (2010), An amino acid residue in the middle of the fingers subdomain is involved in Neq DNA polymerase processivity: enhanced processivity of engineered Neq DNA polymerase and its PCR application, *Protein Eng Des Sel*, Nov;23(11):835-42. PMID: 20851826

Choi JJ, **Song JG**, Nam KH, Lee JI, Bae H, Kim GA, Sun Y, Kwon ST, (2008), Unique substrate spectrum and PCR application of Nanoarchaeum equitans family B DNA polymerase, *Appl Environ Microbiol*, Nov;74(21):6563-9. PMID: 18791030